Bandgap-Engineered HgCdTe Infrared Detector Structures for Reduced Cooling Requirements

by

Anne M. Itsuno

A dissertation submitted in partial fulfillment
of the requirements for the degree of
Doctor of Philosophy
(Electrical Engineering)
in The University of Michigan
2012

Doctoral Committee:

Associate Professor Jamie D. Phillips, Chair
Professor Pallab K. Bhattacharya
Professor Fred L. Terry, Jr.
Assistant Professor Kevin P. Pipe

To my parents.

ACKNOWLEDGEMENTS

First and foremost, I would like to thank my research advisor, Professor Jamie Phillips, for all of his guidance, support, and mentorship throughout my career as a graduate student at the University of Michigan. I am very fortunate to have had the opportunity to work alongside him. I sincerely appreciate all of the time he has taken to meet with me to discuss and review my research work. He is always very thoughtful and respectful of his students, treating us as peers and valuing our opinions. Professor Phillips has been a wonderful inspiration to me. I have learned so much from him, and I believe he truly exemplifies the highest standard of teacher and technical leader.

I would also like to acknowledge the past and present members of the Phillips Research Group for their help, useful discussions, and camaraderie. In particular, I would like to thank Dr. Emine Cagin for her constant encouragement and humor. Emine has been a wonderful role model. I truly admire her expertise, her accomplishments, and her unfailing optimism and can only hope to follow in her footsteps. I would also like to thank Dr. Pierre Emelie, whose research on HgCdTe devices has been the basis of the work I have pursued in my dissertation. Pierre has always been available to provide technical advice related to my research, and I sincerely appreciate him taking the time to do so in his busy schedule.

Next, I would like to thank Professor Jose Oscar Mur-Miranda, my undergraduate research advisor at the Franklin W. Olin College of Engineering. During my time at Olin and since, he has been very supportive of me, encouraging me in my technical studies and creativity. I have really enjoyed working with and learning from Oscar,

who has influenced the direction of my career focus for the better.

I would also like to take this opportunity to acknowledge my former teachers from Pearl City High School, Mr. Darell Takahashi (Physics) and Mrs. Amanda Amodo (Math), who instilled in me the value of science and math by using creative and interactive teaching methods, sparking my initial interest in engineering.

I extend my thanks to my wonderful friends who have touched and shaped my life in many ways, who have supported me, and who have helped to create some of my best memories.

I would sincerely like to thank my fiancé, Dan Lindquist, who has been extremely supportive, patient, understanding, and good-natured for as long as I have known him.

And finally, my deepest gratitude goes to my loving family: my father, Maurice, my mother, Shizue, and my younger brother, Andrew, who have steadfastly cheered me on through my endeavors. My parents taught me the value of education and hard work, and they have always encouraged me to challenge myself, to achieve no less than my best. For that, I am very grateful, and I dedicate this thesis to them.

Financial student support for my work was provided by the National Science Foundation Graduate Research Fellowship Program. I would like to acknowledge EPIR Technologies, Inc., for the use of their laboratory equipment and facilities, and Dr. Silviu Velicu for extending me the opportunity to experience research and development in an industry setting. I would also like to thank current and former EPIR engineers Matthew Chriss, Dr. Ramana Bommena, Scott Barnes, Dan Adams, John Ellsworth, Dr. Jun Zhao, Dr. Christoph Grein, Chris Buurma, Andrew Yang, and Michael Morley for their technical assistance, feedback, and support.

TABLE OF CONTENTS

CHAPTER

LIST OF FIGURES

Figure

LIST OF TABLES

Table

LIST OF ABBREVIATIONS

BLIP Background limited performance

BTB Band-to-band

DLHJ Double layer heterojunction

DLPH Double layer planar heterostructure

EPD Etch pit density

FOV Field–of–view

FPA Focal plane array

FTIR Fourier transform infrared

G-R Generation-recombination

HOT High operating temperature

IR Infrared

I-V Current-voltage

LPE Liquid phase epitaxy

LWIR Long-wave infrared

MBE Molecular beam epitaxy

MOCVD Metal organic chemical vapor deposition

MWIR Mid-wave infrared

NDR Negative differential resistance

PC photoconductive

PV photovoltaic

QDIP Quantum dot infrared photodetectors

QE Quantum efficiency

QWIP Quantum well infrared photodetectors

RHEED Reflection high-energy electron diffraction

SE Spectroscopic ellipsometry

SIMS Secondary ion mass spectroscopy

SRH Shockley–Read–Hall

SWIR Short-wave infrared

TAT Trap-assisted tunneling

TE Thermoelectric

VLWIR Very long-wave infrared

ABSTRACT

Bandgap-Engineered HgCdTe Infrared Detector Structures for Reduced Cooling Requirements

by

Anne M. Itsuno

Chair: Jamie D. Phillips

State-of-the-art mercury cadmium telluride (HgCdTe) high performance infrared (IR) *p*-*n* heterojunction technology remains limited by intrinsic, thermal Auger generation-recombination (G-R) mechanisms which necessitate strict cooling requirements, and challenges related to processing technology, particularly those associated with achieving stable, controllable *in situ* *p*-type doping in molecular beam epitaxy (MBE) grown HgCdTe. These limitations motivate the need to firstly, increase device operating temperatures, and secondly, address material processing issues. This work investigates three alternative HgCdTe IR device architectures as proposed solutions: 1) the high operating temperature (HOT) detector, 2) the nBn detector, and 3) the NBνN detector. The HOT detector is designed to suppress Auger processes, in turn, reducing the detector noise and cryogenic cooling requirements. A simulation study comparing the device behavior and performance metrics of the Auger-suppressed HOT structure to those obtained for the conventional double layer planar heterostructure (DLPH) device predicts the HOT detector can provide a significant advantage over conventional detectors with an increased operating temperature of ∼40-50 K for devices with cutoff wavelengths in the range of 5-12 μm. In a related study, a series of experiments is conducted to examine arsenic (As) deep diffusion in HgCdTe with the goal of achieving controllable low *p*-type doping in the HOT absorber layer to reduce Auger G-R processes by increasing minority carrier lifetimes. Furthermore, a unipolar, barrier-integrated nBn detector structure is proposed to address the challenges associated with *p*-type doping in MBE grown HgCdTe. Numerically simulated performance characteristics of the HgCdTe nBn device predict values similar to comparable DLPH structures for a range of temperatures, motivating the experimental demonstration of mid- and long-wave IR HgCdTe nBn detectors. Fabricated nBn detectors successfully exhibit barrier-influenced current-voltage and photoresponse characteristics, but are limited by perimeter leakage currents which must be resolved in future work. Finally, this work culminates with the simulation study of the novel, hybrid NBνN structure which addresses both technology limitations by combining the advantages and designs of the Auger-suppressed HOT and unipolar nBn detectors in a single configuration.

CHAPTER I

Introduction

1.1 Overview of IR Technology

Infrared (IR) detectors are devices that respond to incident photons with wavelengths in the infrared spectrum (∼1 μm - 1000 μm). Traditionally, infrared detector technology was developed primarily to fulfill military sensing needs for night vision and surveillance, tank sight systems, and anti-air missile seekers. More recently, the detector market has expanded rapidly to include a wide array of science, medical, and industrial applications such as manufacturing heat distribution monitoring, medical diagnostic imaging, meteorology and astronomy, short range communication, chemical detection, and spectroscopy. Some familiar examples of system-integrated IR detectors are shown in Figure 1.1.

The IR range within the electromagnetic spectrum is illustrated in Figure 1.2. For many IR applications, sensing requires data transmission by air. The presence of large suspended particles such as water droplets, particulates, and aerosols in the environment results in signal attenuation due to wavelength scattering caused by the absorption and re-radiation of photon energy. Figure 1.3 shows a plot of atmospheric transmission through air at sea level over a range of infrared wavelengths where distinct transmission windows are observed. Thus, detector development focuses on devices which operate within these windows, referred to as the short-wavelength infrared

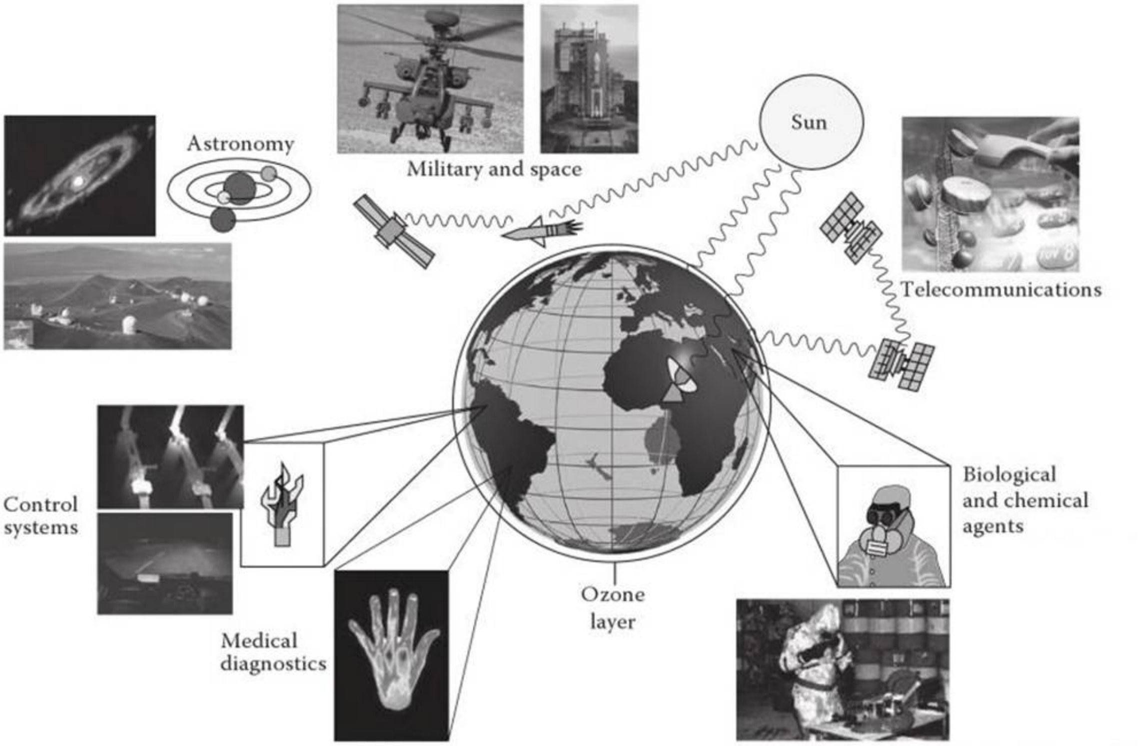

Figure 1.1: System-integrated infrared detector applications [1].

(SWIR, 1 μm-3 μm), mid-wavelength infrared (MWIR, 3 μm-5 μm), long-wavelength infrared (LWIR, 8 μm-14 μm), and very long-wavelength infrared (VLWIR, >14 μm, not shown in Figure 1.3) spectral ranges.

A wide variety of IR detectors have been developed comprising different materials and device architectures. Most commercially available detectors can be classified as one of the following [1]:

- photon detectors (photodetectors)
    - intrinsic detectors
    - extrinsic detectors
    - photoemissive detectors
    - quantum well and quantum dot detectors
- thermal detectors

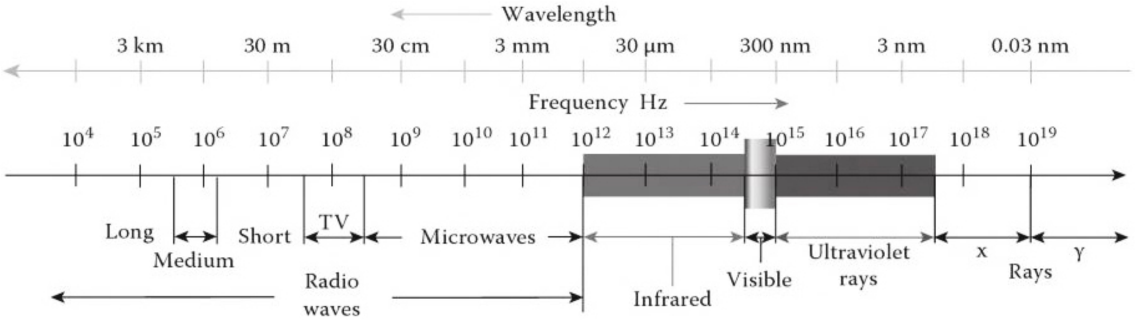

Figure 1.2: Infrared range within electromagnetic spectrum [1].

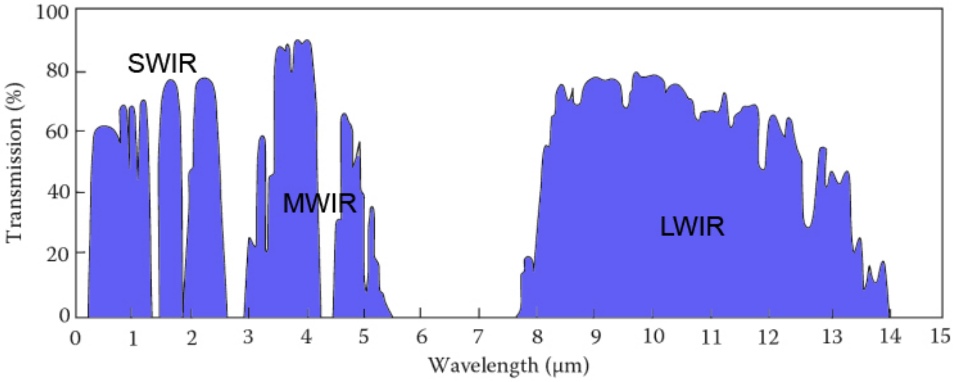

Figure 1.3: Atmospheric transmission as a function of wavelength for 6000 ft. horizontal path containing water precipitates, carbon dioxide, and oxygen molecules. Modified schematic adapted from Ref. [1].

  - bolometers
  - pyroelectric detectors
  - thermopiles
  - thermocouples
- radiation field detectors

Radiation field detector applications in the far-IR are beyond the scope of this study, and these devices will not be further discussed in this work.

The distinction between infrared photon and thermal detectors is given by the difference in their operating mechanisms. Photon detectors are based on semiconductor materials that absorb incident IR photon radiation. The absorbed energy results

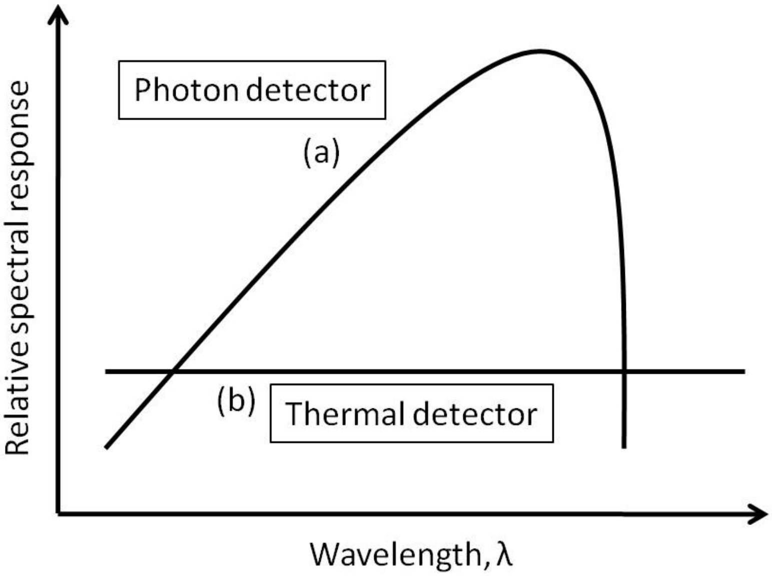

Figure 1.4: Generic (a) photon and (b) thermal detector spectral response based on Ref. [2].

in optical excitation, generating electron-hole pairs and changing the overall charge carrier distribution within the semiconductor. The rapid photon-carrier interaction is observed in an electrical output signal typically measured by the collected device current. Because the incident photon energy influences absorption, the photon detector response is wavelength dependent as illustrated in Figure 1.4a.

Photon detectors can be subdivided into several categories including intrinsic detectors, extrinsic detectors, photoemissive detectors, quantum wells, and quantum dots. Intrinsic detectors consist of direct bandgap semiconductors of III-V (InGaAs, InAs, InSb, InAsSb), IV-VI (PbS, PbSe, PbSnTe), and II-VI (HgCdTe) material systems where photon-induced optical transitions primarily occur between the valence and conduction bands. Extrinsic detectors consist of indirect bandgap semiconductors such as Si doped with Ga or As (Si:Ga, Si:As) or Ge doped with Cu or Hg (Ge:Cu, Ge:Hg) to facilitate photon absorption from the impurity band within the forbidden gap to the conduction band. Photoemissive detectors are typically metal silicide Schottky barrier devices made of PtSi, Pt_2Si, or IrSi. Quantum well and quantum dot IR photodetectors (QWIP, QDIP) consist of superlattice structures and heterojunction configurations of type-I (GaAs/AlGaAs, InGaAs/AlGaAs) or type-II (InAs/InGaSb, InAs/InAsSb) materials. Depending on the design, materials, and application, these devices can be operated in photoconductive (PC), photovoltaic (PV), photoelectromagnetic, or photoemissive modes.

Photon detectors are generally characterized as having fast response and high signal-to-noise ratio. However, narrow bandgap semiconductors used for longer wavelength (>3 μm) applications are susceptible to thermal transitions which contribute to noise, and conventional photodetectors often require cryogenic cooling to reduce thermal generation of charge carriers. Thus, high performance IR photodetectors face a well-known trade-off with sensitivity and size, power, and cost requirements for complex cooling systems such as Joule-Thompson cryostats and Stirling-cycle coolers.

IR thermal detectors are employed in various forms, most of which are commonly identified as bolometers, pyroelectric detectors, and thermopiles and thermocouples. When subjected to incident photons, the detector material is heated by the IR radiation resulting in a change in temperature. A temperature-dependent property such as resistance, pyroelectric voltage, or thermoelectric voltage is then used to generate an electrical signal. The detector response time is limited by the heating and cooling time of the detector element. Furthermore, the thermal detector spectral response is broad and generally wavelength independent as shown in Figure 1.4b, relying on the incident power rather than the energy of the incoming photons. Unlike photon detectors, thermal detectors are usually operated at room temperature and typically found in low cost, low sensitivity applications [2, 3].

Photodetectors remain the preferred technology for high performance IR sensing applications. A major objective of photon detector development is to increase the operating temperature of IR imaging systems without sacrificing performance. Current

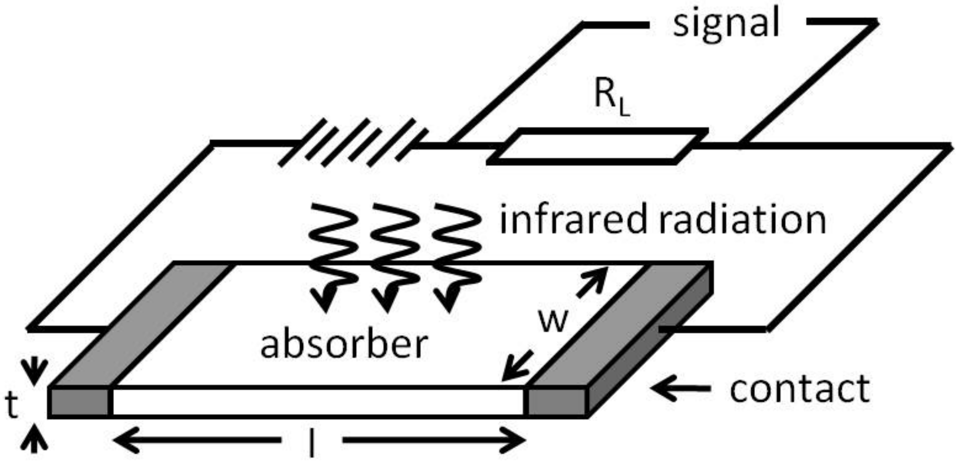

Figure 1.5: Basic photoconductor model based on Ref. [1].

efforts are aimed at developing IR devices, particularly those sensing in the MWIR-VLWIR spectral ranges, with operating temperatures that can be achieved and maintained using single- or multi-stage thermoelectric (TE) cooling systems which are simpler, smaller, lighter, and less expensive in terms of cost and power requirements compared to cryogenic systems. TE coolers can reach temperatures from 250 K (one-stage, TE1) down to 190 K (four-stage, TE4) [1].

Among the variety of photon detectors developed, PC and PV devices are the most widely used. The PC device can be described as a photo-sensitive resistor, as shown in Figure 1.5. The operation of a photoconductor device is based on the change in conductivity of the material due to the generation of optically excited carriers when the detector material is exposed to incident photons with energy $E_{ph} = h\nu$ greater than its bandgap E_g. With photovoltaic devices, such as the *p*-*n* junction photodiode illustrated in Figure 1.6, the optically excited excess carriers are injected into regions near the built-in potential barriers. The photogenerated electron and hole charges are then swept out by the built-in electric field (E_{field}) near the barriers, and the carriers are collected at the contacts. Other PV structures which rely on this operating mechanism include, but are not limited to, heterojunction detectors,

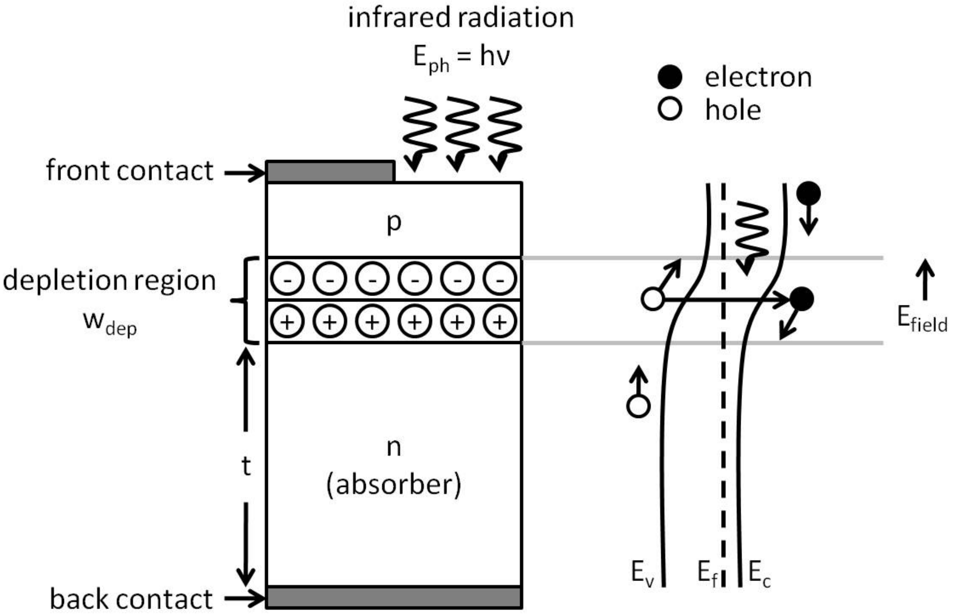

Figure 1.6: Basic photovoltaic detector (p-n homojunction photodiode) model and energy band diagram based on Ref. [1].

photocapacitors, and Schottky barrier photodiodes.

Recent trends in research have seen more advancements in PV p-n junction photodiode technology over photoconductors. This shift is attributed to the increased interest in using 2-D silicon hybrid focal plane arrays (FPAs) for detection in the MWIR and LWIR spectral ranges for defense and space applications. Furthermore, FPA based systems tend to be lighter and smaller, consuming less power and reducing associated costs, while providing higher performance than first-generation linear array photoconductor based systems. Photodiodes generally have relatively high impedance, matching that of Si read-out integrated circuits (ROICs), and low power dissipation compared to conventional photoconductors. Moreover, the strong built-in field present in the depletion region near the p-n interface facilitates rapid collection of the photogenerated carriers, resulting in faster detector response. Most importantly, photodiode architecture is conducive to the 2-D megapixel array assembly favorable for high spatial resolution while PC detectors are limited by their inability to be easily integrated on the focal plane. By these virtues, PV photodiodes have taken the lead as the state-of-the-art second-generation IR detector technology [1].

1.2 Performance Figures

The conventional parameters used to characterize general IR detector performance are introduced in this section. These figures of merit will be used frequently to evaluate and analyze the devices discussed in this work and should be noted.

1.2.1 R_0A Product

The R_0A product (Ω-cm^2) is a commonly used performance parameter for photodiodes. In many applications, photodiodes are operated at zero bias such that

$$R_0 = \left(\frac{\delta I_{dark}}{\delta V}\right)^{-1}_{|V_{bias}=0}, \tag{1.1}$$

and thus,

$$R_0A = \left(\frac{\delta J_{dark}}{\delta V}\right)^{-1}_{|V_{bias}=0} \tag{1.2}$$

where J_{dark} is the dark current density (A/cm^2) given by $J_{dark} = I_{dark}/A$, where I_{dark} is the dark current (A) and A is the device junction area (cm^2). High performance IR detectors typically exhibit low J_{dark} and high R_0A, where J_{dark} and R_0A values correlate to detector noise. It is noted that photodiodes may be operated at any point along the current-voltage (I-V) curve for radiation detection. For high frequency applications such as IR imaging, photodiodes are typically operated at a slight reverse bias to reduce carrier transit time by increasing the width of the depletion region and strength of the E$_{field}$. Other situations where biases are applied include detector configurations requiring non-equilibrium carrier concentrations or voltage-controlled bandedge alignment for operation. In such devices, the dynamic resistance-area product R_dA (Ω-cm^2) at the given bias is used instead to calculate parameters such as detector noise. It is noted that for non-conventional photodiodes, the R_0A metric may not necessarily be considered an accurate performance evaluation figure.

1.2.2 Spectral Response

The spectral response of the detector can be characterized by responsivity R and external quantum efficiency (QE or η). Responsivity (A/W or V/W) characterizes how well a photodetector detector responds to IR photon illumination and is calculated from the photocurrent density J_{ph} (A/cm^2) and the incident radiation power density ϕ (W/cm^2) [4],

$$R = \frac{J_{ph}}{\phi}. \tag{1.3}$$

The external quantum efficiency represents how effectively a detector converts incident photons of a particular wavelength λ (μm) into photocurrent. The normalized η value for a given wavelength is defined by [4]

$$\eta = \frac{J_{ph}hc}{\phi q \lambda} = R\frac{1.24}{\lambda} \tag{1.4}$$

where q is the electronic charge (C), h is Planck's constant (J-s), and c is the speed of light (cm/s).

1.2.3 Noise Current

Standard p-n photodiodes may operate at 0 V or under a slight reverse bias to enhance photocurrent collection. The noise current i_n (A/Hz$^{0.5}$) in an ideal p-n photodiode can be expressed as [4]

$$i_n(0) = \sqrt{\left(\frac{4k_BT_d}{R_0A} + 2q(J_{scene})\right)A} \tag{1.5}$$

at zero bias, or

$$i_n(V_{bias}) = \sqrt{\left(\frac{4k_BT_d}{R_dA} + 2q(J_{dark} + J_{scene})\right)A} \tag{1.6}$$

under reverse bias V_{bias} (V) where k_B is Boltzmann's constant (eV/K), T_d is the detector temperature (K), and J_{scene} is the background scene induced photocurrent density (A/cm^2).

The expression for i_n includes contributions from thermal, electrical, and optical shot noise. The first term in equation 1.6 is the Johnson-Nyquist noise, which is electrical noise generated by thermal agitation of charge carriers regardless of applied voltage. The second term in the equation reflects the bias-dependent electrical shot noise due to random fluctuations of discrete electron charges, which can be of significance when dealing with extremely low dark current values. The final term characterizes shot noise caused by photons generated by the background scene with temperature T_s. The background scene is typically modeled as a 300 K blackbody for earth applications and ignored or modeled as <300 K for space applications. The scene-induced photocurrent is defined as [4]

$$J_{scene} = \frac{q}{1+4f_{\#}^2}\int_0^{\lambda_{co}} \frac{2\pi c}{\lambda^4}\left(\frac{1}{exp(\frac{hc}{T_sk_B\lambda})-1} - \frac{1}{exp(\frac{hc}{T_dk_B\lambda})-1}\right)\eta(\lambda)d\lambda \tag{1.7}$$

where λ_{co} is the cutoff wavelength and $f_{\#}$ is the f-number corresponding to the field-of-view (FOV). λ_{co} (also noted as λ_{cutoff}) is typically defined as the wavelength at which the detector spectral response drops to 50% of its peak value. It should be noted that the electrical shot noise is typically dominated by Johnson-Nyquist thermal noise for detectors operating at or near zero bias, while the reverse case is true for devices operated under larger biases. i_n is expressed as the quadrature sum of all of noise current components.

1.2.4 Detectivity

The detectivity D^* (cm $\text{Hz}^{0.5}$/W) is the primary figure used to evaluate detector performance and corresponds to the normalized signal-to-noise ratio of the device. The detectivity is defined as [4]

$$D^* = \frac{R_\lambda \sqrt{A}}{i_n} \tag{1.8}$$

where R_λ is the responsivity (A/W). In this study, the peak D^* is used for performance evaluation, in which case, R_λ is $R_{\lambda_{peak}}$, the peak responsivity. Detectivity can be improved by increasing the detector responsivity and reducing the noise current, although this proves to be a non-trivial task for high performance devices operating near the theoretical limit. Detectors achieve the highest possible D^* values under background limited performance (BLIP) conditions, that is, where the detector performance is limited by the background photon noise.

1.3 Current Status of HgCdTe IR Detector Technology

The spectral detectivities for commercially available detectors are shown in Figure 1.7. Most commercial IR detectors achieve D^* values around 10^{10} $\text{cmHz}^{0.5}$/W or higher in all spectral ranges spanning SWIR to VLWIR. A close look shows ideal PV detectors outperform both PC and thermal detectors. More notably, cryogenically cooled II-VI compound mercury cadmium telluride (HgCdTe, MCT) PV detectors achieve D^* values near the theoretical limit in both MWIR and LWIR spectral ranges, surpassing numerous detectors based on other materials (GaAs, InAs, InGaAs, InSb, Ge:Hg,Cu, PbS, PbSe, PtSi, Si:As). These performance characteristics strongly motivate the pursuit of next-generation HgCdTe photovoltaic IR devices, laying the foundation for this study.

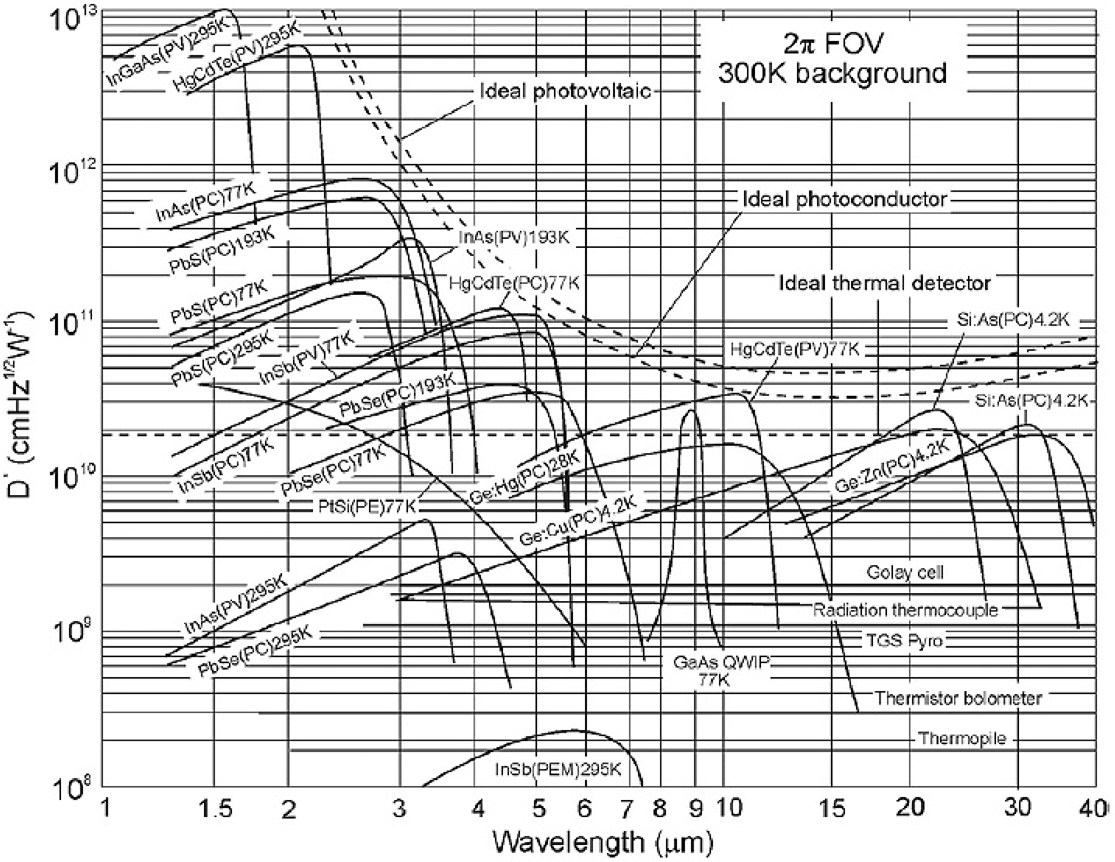

Figure 1.7: D^* values as a function of incident wavelength for commercially available infrared detectors operating at indicated temperature. Theoretical curves for the BLIP D^* values represented by dashed lines for ideal photovoltaic, photoconductor, and thermal detectors [2].

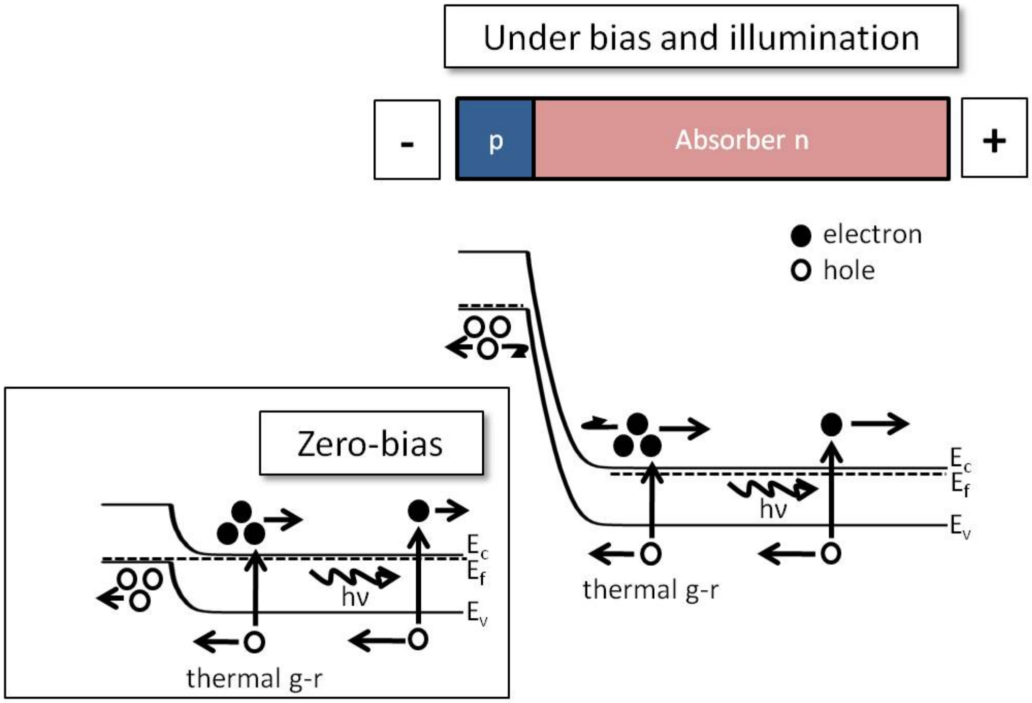

Figure 1.8: Schematic of structure and energy band diagram of a HgCdTe *p*-*n* homojunction photodetector device at zero-bias (inset) and under reverse bias and illumination.

1.3.1 HgCdTe *p*-*n* Junction Photodiode

The photovoltaic *p*-*n* junction photodiode is representative of high performance HgCdTe IR detector technology. Figure 1.8 illustrates the basic operation of a simple, *p*-*n* homojunction detector under illuminated zero-bias and reverse bias conditions. Incident photons with energy greater than the material bandgap ($E_{ph} > E_g$) generate electron-hole pairs in the material on either side of the *p*-*n* junction. Carriers generated within a diffusion length of the space-charge region diffuse to the electrical junction and are separated by the strong electric field (Figure 1.6). The electron and hole minority carrier diffusion lengths L_n and L_p (cm) are given by [5]

$$L_n = \sqrt{D_n \tau_n} \tag{1.9}$$

$$L_p = \sqrt{D_p \tau_p} \tag{1.10}$$

where τ_n and τ_p are the electron and hole minority carrier recombination lifetimes (s), and D_n and D_p are the electron and hole minority carrier diffusion coefficients (cm^{2}s^{-1}) defined by the Einstein relation [5]

$$D_n = \frac{\mu_n k_B T}{q} \tag{1.11}$$

$$D_p = \frac{\mu_p k_B T}{q} \tag{1.12}$$

where μ_n and μ_p are the minority carrier mobilities (cm^2/V-s) for electrons and holes, respectively. The optically excited minority carriers that are injected into the opposite side of the junction by the E$_{field}$ become majority carriers. By this process, a photocurrent density J_{ph} is generated by the incident radiation, increasing the dark saturation current value as illustrated in Figure 1.9. The total current density J_{total} (A/cm^2) in the *p*-*n* junction photodiode is given by [6]

$$J_{total}(V_{bias}) = J_{dark}(V_{bias}) - J_{ph}(\Phi) \tag{1.13}$$

where J_{dark} depends on V_{bias}, and J_{ph} depends on the incident photon flux density Φ (ph/cm^{2}s). In a simple photovoltaic detector with no gain, the photocurrent is equivalent to [6]

$$I_{ph} = J_{ph} A = \eta q \Phi A. \tag{1.14}$$

Most commonly used photovoltaic HgCdTe photodiodes are fabricated in a homojunction configuration with a highly doped n^+ cap layer in contact with a lightly doped, narrow bandgap *p*-type (π) absorber (base) layer, or in a heterojunction con-

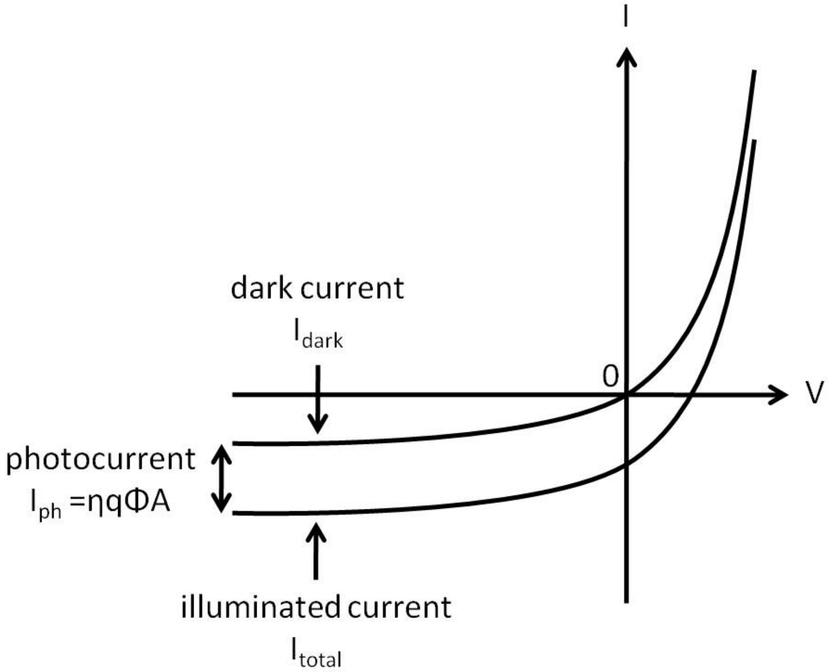

Figure 1.9: Schematic representation of current-voltage characteristics of photodiode under dark and illuminated conditions. Based on Ref. [1]

figuration with wide bandgap (denoted by capitalized letter) P^+ cap layer in contact with a lightly doped, narrow bandgap n-type (ν) absorber layer, as shown in Figure 1.10. In these structures, the absorber layer determines the dark current and photocurrent of the device. The base layer doping in both structures must be below 10^{16} cm^{-3} to avoid tunneling current contribution, and the doping values used are typically $\sim5\times10^{15}$ cm^{-3} and $\sim5\times10^{14}$ cm^{-3} for p-type and n-type layers, respectively [1]. Neither the heavily doped n^+ region nor the wide bandgap P^+ region contribute to the dark current due to suppression of thermal and optical generation mechanisms as a result of the bandgap-widening Burstein-Moss effect in the case of the former and the large transition energy required in the case of the latter. Furthermore, internal electric fields at the junction interface serve to block minority carriers and reduce the influence of surface recombination [1].

Double layer heterojunction (DLHJ) architectures, illustrated in Figure 1.11, have been developed and widely adapted [8–10] for high performance LWIR detectors due

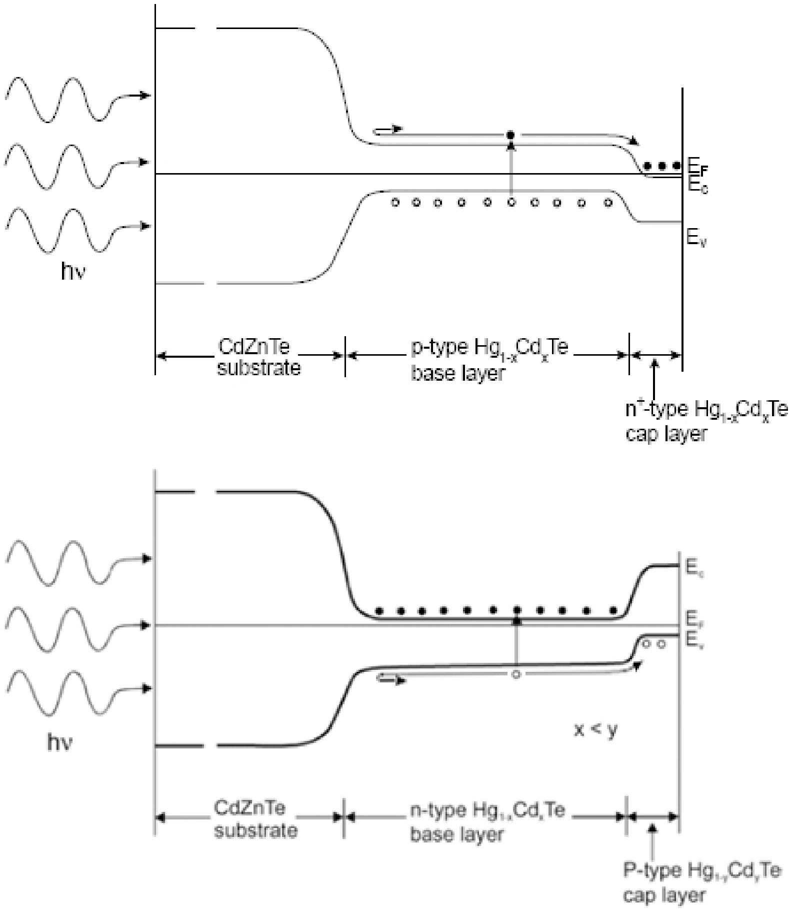

Figure 1.10: Schematic of energy band diagrams of commonly used unbiased (a) *n*-on-*p* homojunction and (b) *P*-on-*n* heterojunction photodiodes under backside illumination [6, 7].

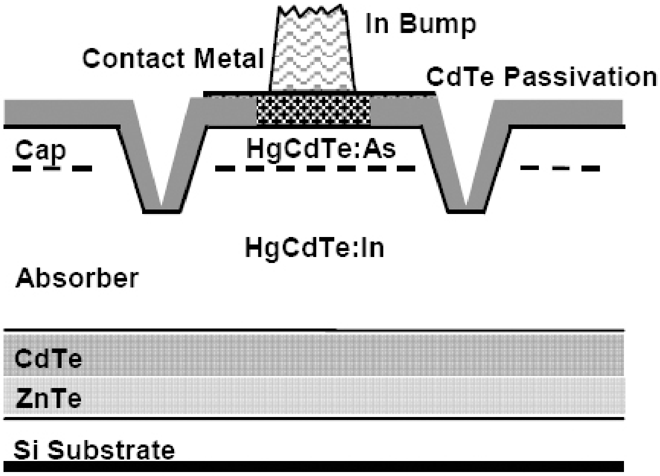

Figure 1.11: HgCdTe DLHJ structure on Si substrate for FPA integration [10].

to low thermal leakage currents [11]. More recently, the double layer planar heterostructure (DLPH) design was introduced to eliminate issues with sidewall leakage observed in etched mesa devices and to reduce contributions of surface defects [12, 13]. These state-of-the-art heterojunction devices exhibit extremely low J_{dark} corresponding to high R_0A values approaching the theoretical limit [14–16]. Throughout this work, the HgCdTe DLPH device operating under a slight bias, as shown in Figure 1.12, is used as the representative *p*-*n* junction technology to which the alternative device structures examined are compared.

1.3.1.1 Current Contribution Mechanisms

The diffusion current I_{diff} (A) is the main current mechanism in an ideal, diffusion-limited *p*-*n* junction photodiode and is described by the basic diode equation,

$$I_{diff} = AJ_{diff} = AJ_s \left[exp\left(\frac{qV_{bias}}{k_BT} \right) - 1 \right], \tag{1.15}$$

where

$$J_s = q\left(\frac{n_{p0}D_n}{L_n} + \frac{p_{n0}D_p}{L_p} \right), \tag{1.16}$$

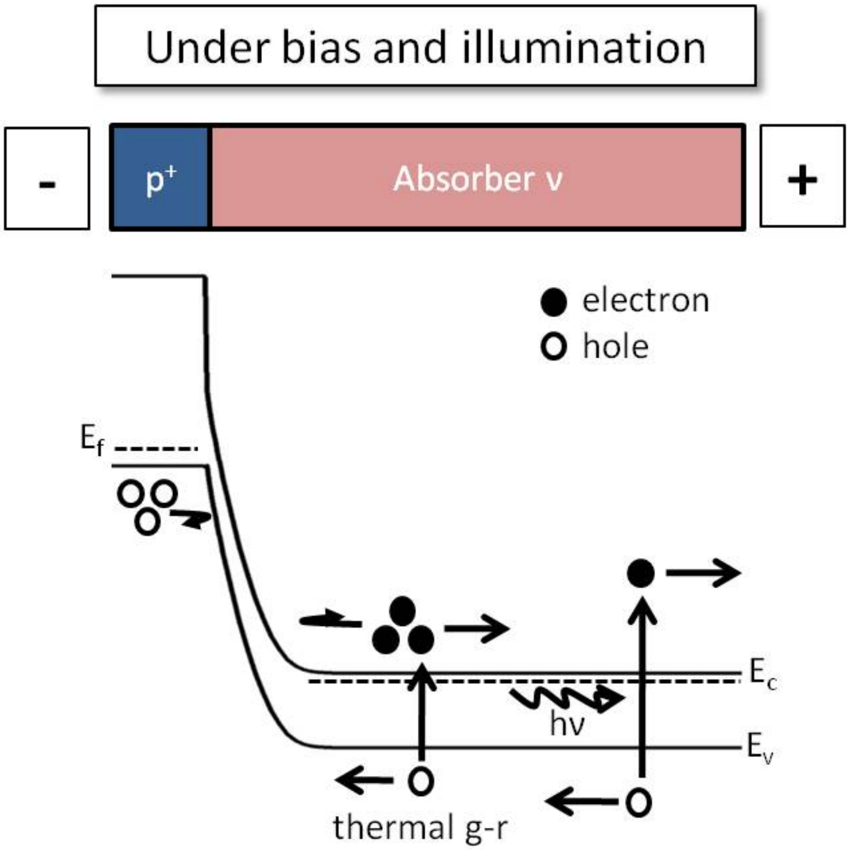

Figure 1.12: Schematic of structure and energy band diagram of a HgCdTe *p*-*n* junction DLPH photodetector device under reverse bias and illumination.

and n_{p0} and p_{n0} are the equilibrium electron and hole concentrations (cm^{-3}) on the p- and n- sides of the junction, respectively. Realistically, additional mechanisms contribute to the dark current density in the photodiode and should be included for a better approximation of the actual device current. These mechanisms, several of which are illustrated in Figure 1.13, include

- generation-recombination (G-R) in the depletion region,
- band-to-band (BTB) tunneling,
- trap-assisted tunneling (TAT), and
- surface recombination.

The total dark current can be expressed as the sum of all contributions

$$I_{dark} = I_{diff} + I_{G-R} + I_{BTB} + I_{TAT} + I_{surf}. \tag{1.17}$$

G-R current is caused by the generation of electron-hole pairs in the semiconductor material [17, 18] and can be facilitated by the presence of extrinsic, process-induced Shockley–Read–Hall (SRH) trap centers or by intrinsic thermal Auger and radiative processes. Under reverse bias, the generation rate due to SRH centers in the depletion region of the device can be considerably greater than in the bulk and should not be neglected. Moreover, materials with narrow bandgaps such as those used in high performance HgCdTe IR detectors are especially susceptible to thermal G-R processes that dominate the dark current at high temperatures. These G-R mechanisms are described in further detail in Chapter II and should be included for a realistic representation of the photodiode current. The expression for G-R current contribution I_{G-R} (A) is given by [2]

$$I_{G-R} = qG_{dep}V_{dep} \tag{1.18}$$

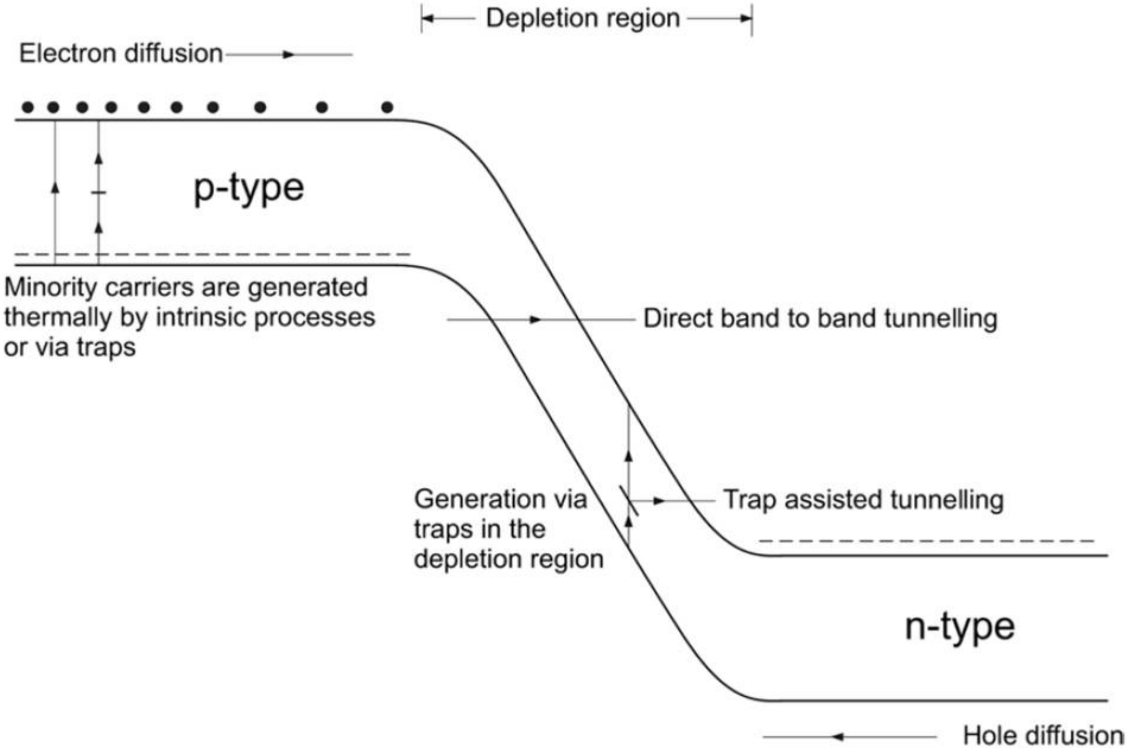

Figure 1.13: Dark current contribution mechanisms in reverse-biased *p*-*n* junction [6].

where G_{dep} is the generation rate (cm$^{-3}s^{-1}$) and V_{dep} is the volume of the depletion region (cm^3).

Band-to-band tunneling occurs when electrons at a given energy level tunnel across the bandgap from the valence band on one side of a junction to the conduction band on the other to fill an unoccupied state at the same energy level. Band-to-band tunneling exhibits a strong dependence on E_g and E$_{field}$, where the field strength depends on V_{bias} and the doping concentration of the junction. The band-to-band tunneling current I_{BTB} (A) is given by [6]

$$I_{BTB} = AJ_{BTB} = \frac{\sqrt{2m_e^*}q^3 E_{field} V_{bias}}{4\pi h^2 \sqrt{E_g}} exp\left(-\frac{4\sqrt{2m_e^*}E_g^{3/2}}{3q\hbar E_{field}}\right) A \tag{1.19}$$

assuming a carrier of constant effective mass m_e^* incident on a potential barrier [19].

Trap-assisted tunneling is caused by carriers tunneling within the depletion region via intermediate trap states created by impurities or defects. The tunneling occurs in a two-step process involving one thermal transition from the valence band to the trap state and a second transition from the trap state to the conduction band. Because the required transition energies are smaller, trap-assisted tunneling occurs at lower fields than band-to-band tunneling. The mechanism is heavily dependent on defect density N_t (cm^{-3}) and the trap level E_{trap} (eV) within the material bandgap.

Rogalski et al. summarize the trap-assisted tunneling process by separating the mechanism into three distinct components and their transition rates to be accounted for when determining the trap-assisted tunneling current [2]:

1. thermal transition of a carrier from the valence band to a trap state E_{trap} in the bandgap with rate $\gamma_p p_t$, where γ_p is the hole recombination coefficient for defect density N_t, and $p_t = N_v exp\left(-E_{trap}/k_B T\right)$ (cm^{-2}), where N_v is the effective density of states in the valence band (thermal transition of a carrier from the conduction band to E_{trap} can be ignored due to the low density of states attributed to the small conduction band electron mass),

2. tunneling of a carrier from the valence band to E_{trap} with rate $\omega_v N_v$ (cm^{-3}s^{-1}), where ω_v represents the carrier tunneling probability from E_{trap} to the valence band, and

3. tunneling of a carrier from E_{trap} to the conduction band with rate $\omega_c N_c$ (cm^{-3}s^{-1}), where N_c (cm^{-3}) is the effective density of states in the conduction band, and ω_c represents the carrier tunneling probability from E_{trap} to the conduction band.

Incorporating each of these rates, the total trap-assisted current can be expressed as [6]

$$I_{TAT} = AJ_{TAT} = qN_t w_{dep}\left(\frac{1}{\gamma_p p_t + \omega v N_v} + \frac{1}{\omega_c N_c}\right)^{-1} A \tag{1.20}$$

where w_{dep} is the depletion width (cm). The expression can be further simplified as

$$I_{TAT} = AJ_{TAT} = qN_t\omega_c N_c w_{dep} A \tag{1.21}$$

assuming $\gamma_p p_t > \omega_v N_v$ and $\omega_v N_c \approx \omega_v N_c$. Then, assuming a uniform E$_{field}$ and parabolic barrier, the tunneling rate $\omega_c N_c$ [20] from E_{trap} to the conduction band is given by [2]

$$\omega_c n_c = \frac{\pi^2 q m_e^* E_{field} M^2}{h^3(E_g - E_{trap})} exp\left[-\frac{(m_e^*/2)^{1/2} E_g^{3/2} F(a)}{2qE\hbar}\right] \tag{1.22}$$

where

$$a = 2\left(\frac{E_{trap}}{E_g}\right)$$

$$F(a) = \left(\frac{\pi}{2}\right) - a(1 - a^{1/2})^{1/2} - \left(\frac{1}{sin(a)}\right)$$

and M is the matrix element associated with the trap potential.

Surface current contributions are also important because device processing can create defects or trap states that affect detector performance. Dangling bonds at the material surface can result in a large density of interface states that generate current via the SRH mechanism. Moreover, the presence of a net surface charge may invert or accumulate the bandedges near the surface creating current channels or affect the position of the junction depletion regions which intersect the surface, facilitating tunneling or field-induced G-R currents [2]. Wide bandgap insulators are ideal for surface passivation and are typically used to neutralize the material surface and reduce the density of surface states.

1.3.1.2 Limitations of HgCdTe *p*-*n* Junction Technology and Proposed Solutions

While high performance HgCdTe *p*-*n* junction detectors exhibit near theoretical R_0A products and D^* values in the MWIR to VLWIR spectral ranges, the technology faces several key challenges which must be addressed for the development of next-generation HgCdTe devices.

As described earlier in this chapter, cryogenic cooling requirements for high performance IR imaging systems remain a major limitation. Thermal G-R processes, namely intrinsic Auger generation described in the next chapter, dominate the dark current density in narrow bandgap materials, fundamentally limiting the detector performance at higher temperatures. Thus, high performance detectors are typically operated at cryogenic temperatures (77 K or lower) and require the use of complex cooling systems such as cryogenic liquid nitrogen (LN_2) dewars, Joule-Thompson cryostats, and Stirling cycle coolers [1]. These cooling systems are extremely bulky, require high input power, and are prohibitively costly to implement. Reducing the size, weight, power, and cost of imaging systems is therefore a critical aspect of advancing IR detector technology. Increasing the detector operating temperature to a range where the cooling requirements can be met by TE coolers (193 K-253 K) is advantageous as these systems are smaller, simpler, and less expensive to integrate [1].

At the processing level, achieving stable, well-controlled, extrinsic *p*-type doping required for *p*-*n* junction PV structures by *ex situ* ion implantation [21–25] or *in situ* doping [26–29] via molecular beam epitaxy (MBE) poses a significant challenge for HgCdTe detector technology. *Ex situ* doping techniques (implantation, in-diffusion) cannot easily provide the level of control over doping profiles necessary for abrupt junction, multi-layer structures and can introduce material damage, reducing the carrier mobilities and minority carrier lifetimes. Furthermore, extrinsic *p*-type doping requires high temperature anneals to mitigate material damage incurred during *ex situ* processes and/or facilitate in-diffusion, and activate dopants. These additional high temperature steps can lead to potentially unwanted diffusion effects and also limit the advantages of low temperature growth by MBE.

The issues which currently limit HgCdTe *p*-*n* junction technology can potentially be addressed by exploring alternative device architectures. This collective study focuses on the design, development, and performance improvements of novel, bandgap-engineered HgCdTe detectors for high temperature operation using theoretical and experimental investigation techniques. The three architectures examined in this work are the (1) Auger-suppressed non-equilibrium high operating temperature (HOT) device, the (2) unipolar nBn detector, and the (3) hybrid NBνN detector.

The HOT detector is proposed to reduce intrinsic Auger G-R processes in MWIR and LWIR HgCdTe detectors, leading to higher temperature BLIP compared to conventional *p*-*n* junction photodiodes. The nBn detector is a simplified, all *n*-type structure which employs an optimized, wide bandgap barrier layer to suppress SRH generation and surface leakage mechanisms that dominate dark current density. Finally, the proposed NBνN detector is a combination of the HOT and nBn structure, exploiting the advantages of both devices in an all *n*-type configuration for high temperature operation. Figure 1.14 summarizes the solutions provided by each of the designs discussed in this work.

1.4 Next-Generation HgCdTe IR Detectors

The basic operation of the proposed HOT, nBn, and NBνN detectors are briefly explained in the following subsections. More detailed explanations can be found in the subsequent chapters.

		Limitations of HgCdTe *p*-*n* junction technology	
		Cryogenic cooling requirement	Challenges with *p*-type doping
Proposed Solution	HOT	• Suppress thermal Auger G-R processes • Increase T_{BLIP}	
	nBn	• Suppress SRH processes, surface leakage mechanism	• All *n*-type doping
	NBvN	• Suppress thermal Auger G-R processes • Suppress SRH processes, surface leakage mechanism • Increase T_{BLIP}	• All *n*-type doping

Figure 1.14: Limitations of HgCdTe *p*-*n* junction (DLPH) technology and solutions proposed using alternative detector designs.

1.4.1 High Operating Temperature (HOT) Detector

Because thermal generation of carriers in IR detectors contributes to noise current that can overwhelm the signal response, low operating temperatures are required to achieve high performance. To reduce stringent cooling requirements and increase the operating temperature, a device operating in non-equilibrium mode was first proposed by Ashley and Elliott [30] in the mid-1980s. The concept of the high operating temperature (HOT) structure is based on the suppression of Auger G-R processes by reducing the thermal carrier concentration in the absorber layer below its equilibrium value. The device consists of a near intrinsic (lightly doped n-type (ν) or p-type (π)), narrow bandgap absorber layer contacted on opposite sides by either 1) two wide bandgap/heavily doped P^+ and N^+ layers as shown in Figure 1.15, or 2) a wide bandgap and a separate heavily doped layer. The P^+-ν or N^+-π interface serves as the extraction junction which, when operated in a slight reverse bias, removes minority carriers from the absorber layer. The unipolar interface (ν-N^+ or π-N^+), also called the exclusion junction, prevents minority carriers from the highly doped/wide bandgap region from being injected into the absorber to replace the diminished carrier concentration. Under applied bias, the minority carriers are rapidly removed from the absorber faster than they can be replenished, and the majority carrier concentration in the absorber is partially depleted below equilibrium to a value near its net doping concentration to maintain charge neutrality. The reduction in minority and majority carriers in the absorber suppresses the Auger thermal processes which would otherwise dominate the dark current at higher temperatures.

1.4.2 Unipolar nBn Detector

The unipolar nBn device is a concept recently proposed by Maimon et al. [31] and demonstrated in III-V compound, type-II heterojunction materials [31–33]. The basic structure shown in Figure 1.16 consists of three n-type layers: a thin, narrow

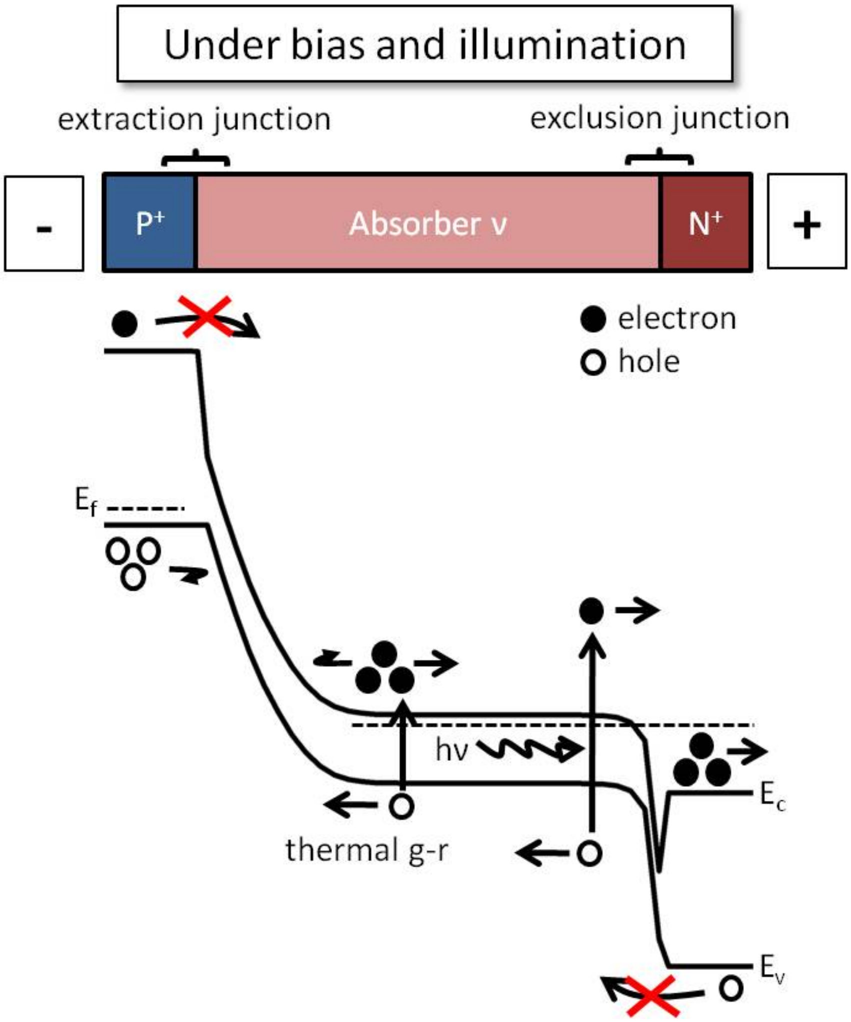

Figure 1.15: Schematic of structure and energy band diagram of a HgCdTe HOT photodetector under reverse bias and illumination.

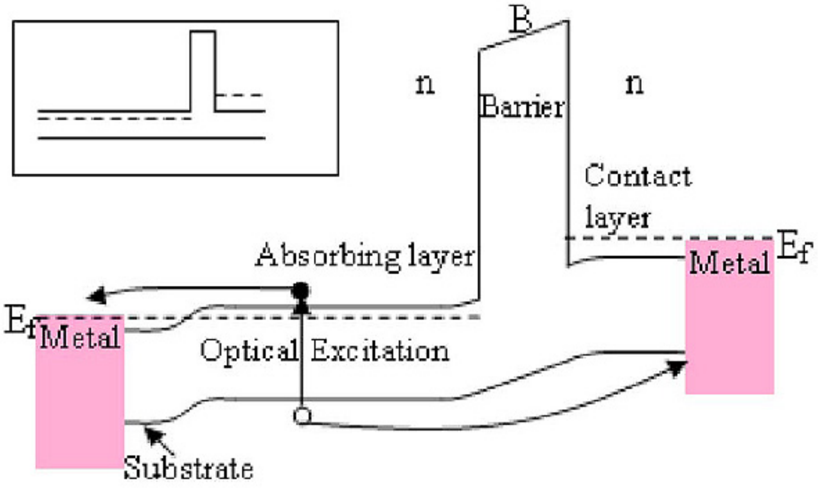

Figure 1.16: Band diagram of a unipolar InAs-based nBn structure at flatband (inset) and biased operating conditions [31].

bandgap contact (n), an undoped, wide bandgap electron barrier (B) with conduction band offset ΔE_c (where $\Delta E_v \approx 0$ eV), and a thick, narrow bandgap absorber (n). The device is designed such that the depletion region falls mostly within the undoped barrier layer. The nBn detector operates as a minority carrier device, selectively blocking electrons in the contact layer while conducting holes from the absorber. Optically generated carriers in the absorber are collected at opposing contacts, where the collection efficiency can be improved when the device is operated under a slight bias. The barrier layer provides several notable functions, suppressing SRH mechanisms that are typically activated in the depletion region and pronounced in narrow bandgap materials, and eliminating the need for surface passivation by reducing surface leakage currents.

1.4.3 Hybrid NBνN Detector

The multi-layer NBνN detector shown in Figure 1.17 combines the unipolarity of the nBn device and the operation of the HOT structure and is proposed for high temperature operation by exploiting the advantages of both devices. The barrier layer

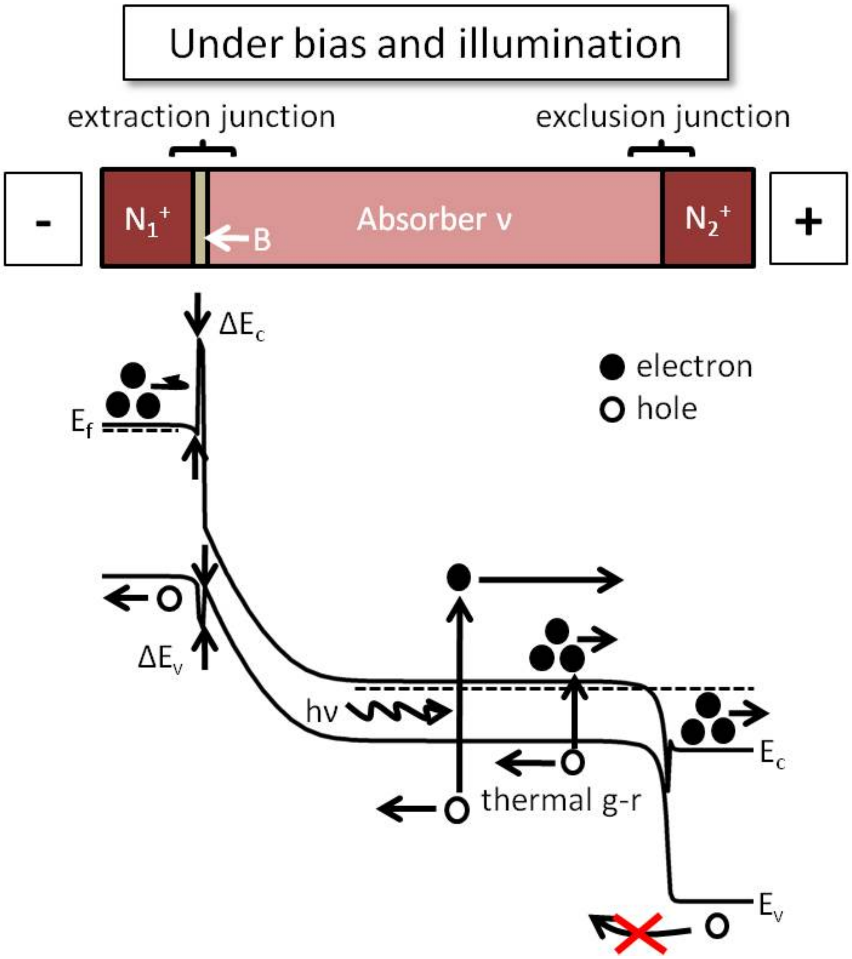

Figure 1.17: Schematic of structure and energy band diagram of a hybrid HgCdTe NBνN device under reverse bias and illumination.

(B) with conduction band offset ΔE_c blocks the flow of majority carrier (electron) current from the N_1^+ cap region to the absorber ν while simultaneously facilitating the flow and collection of thermally and optically generated holes from the absorber to the N_1^+ cap region. Like the HOT structure, the NBνN device consists of an extraction and exclusion junction formed at the interfaces of the N_1^+ cap, B, and absorber (ν) layers and the interface of the ν and N_2^+ layers, respectively. The presence of these junctions facilitate Auger suppression, which is necessary to reduce the dark current density in the detector for high temperature operation.

1.5 Research Direction

This extended study investigates several alternative device solutions using theoretical and experimental means. Figure 1.18 illustrates the organization of this work. The fundamental properties of HgCdTe are provided in Chapter II to familiarize the reader with the important material parameters, characteristics, and mechanisms necessary for understanding their influence on device behavior. The simulation methodology used for theoretical device modeling is described in Chapter III. Chapter IV discusses the performance benefits of a non-equilibrium, Auger-suppressed HOT detector designed to decrease thermally generated dark current contributions and increase the device sensitivity. The simulation study compares the HOT structure to the current, state-of-the-art *p*-*n* junction technology. Chapter V expands upon the HOT device with an experimental investigation of arsenic diffusion behavior in HgCdTe to achieve an optimal $P^+/\pi/N^+$ structure using controllable implantation and deep diffusion techniques. In Chapter VI, an alternative, unipolar HgCdTe nBn structure is proposed based on the III-V barrier-integrated device concept developed by Maimon et al. [31]. The calculated performance characteristics of the nBn device are compared to those of the high performance DLPH detector. The HgCdTe nBn technology shows potential benefits associated with the simplified fabrication process,

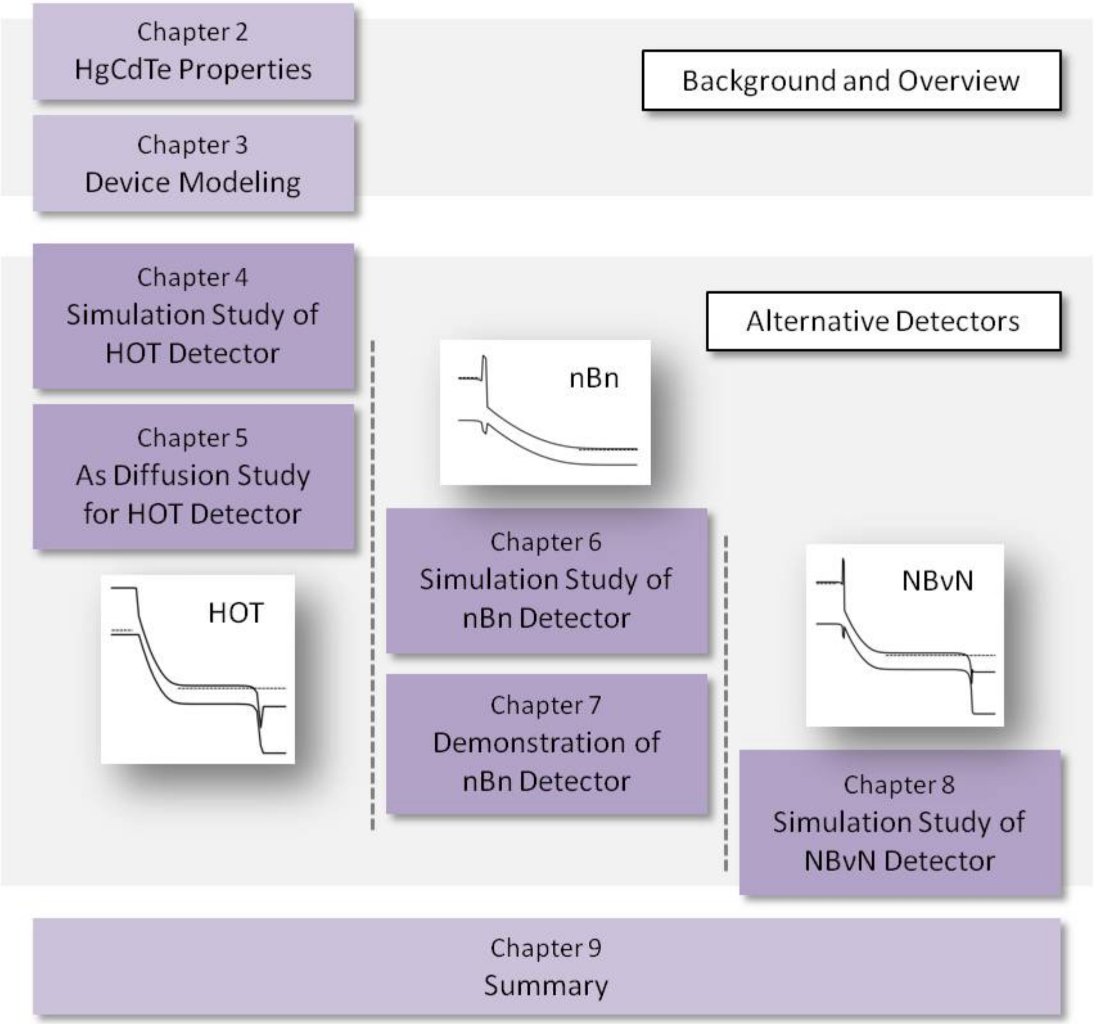

Figure 1.18: Organization of thesis.

eliminating the need for *p*-type doping, without compromising device performance. Single element MWIR and LWIR HgCdTe nBn devices are experimentally demonstrated in Chapter VII. Finally, Chapter VIII examines a novel NBνN architecture proposed for high temperature operation by combining the structures of the HOT and nBn devices, and the calculated performance values are compared to those of DLPH and nBn detector designs. The research findings from this work are summarized in Chapter IX.

The objective of this thesis is to provide the theoretical and experimental foundation for alternative HOT, nBn, and NBνN detectors as potential solutions to the limitations of current high performance IR *p*-*n* junction technology. The primary contributions of this work are the comprehensive numerical simulation studies investigating performance improvements and device behavior of the proposed bandgap-engineered HgCdTe detector architectures for reduced cooling requirements, the HOT detector dopant diffusion study, and the first-reported demonstration of the single element HgCdTe nBn detector.

CHAPTER II

HgCdTe Material Properties

2.1 Overview of HgCdTe

HgCdTe is the most widely used semiconductor for high-performance IR photodetectors due to its favorable optical and material properties for SWIR to VLWIR applications. Over the years, IR technology has seen the emergence of competing detectors made with other semiconductor materials such as InSb, InAs, AlGaAs, PbSe, and SiGe, and alternative structures such as heterojunctions, Schottky barriers, compound strained layer superlattices, and multiple quantum wells. Although these devices are potentially manufacturable and/or more cost-effective, they fail to outperform HgCdTe IR detectors. Overall, they are limited by their fundamental properties, which cannot match those of HgCdTe. To that end, HgCdTe remains the front-runner for high-performance IR FPAs, motivating further efforts to push the boundaries of the technology. This chapter introduces the fundamental properties of the HgCdTe material, the relevant carrier mechanisms, and the MBE growth technique used to achieve high quality epilayers for device applications.

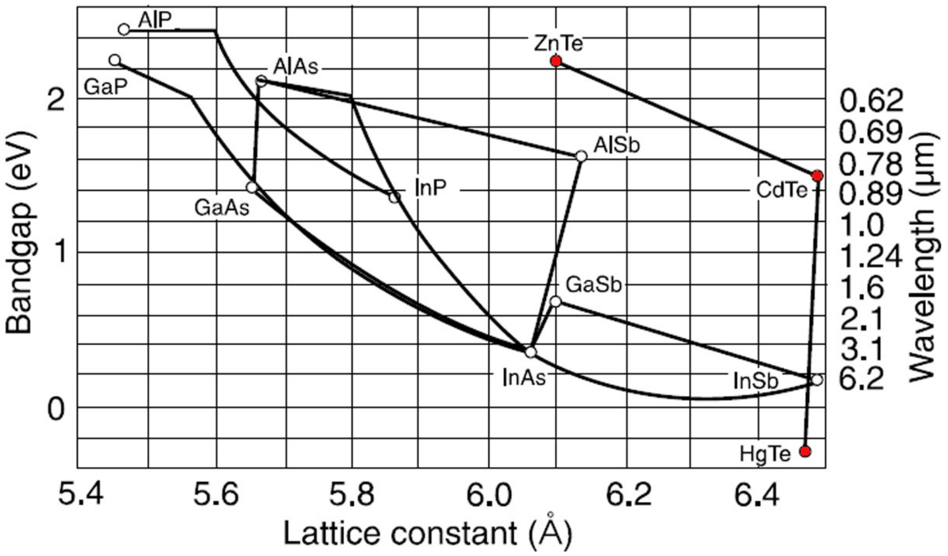

Figure 2.1: Bandgap and corresponding cutoff wavelength as a function of lattice constant for varying compositions of selected III-V materials, HgCdTe, and CdZnTe. Pure HgTe, CdTe, and ZnTe values indicated in red [34].

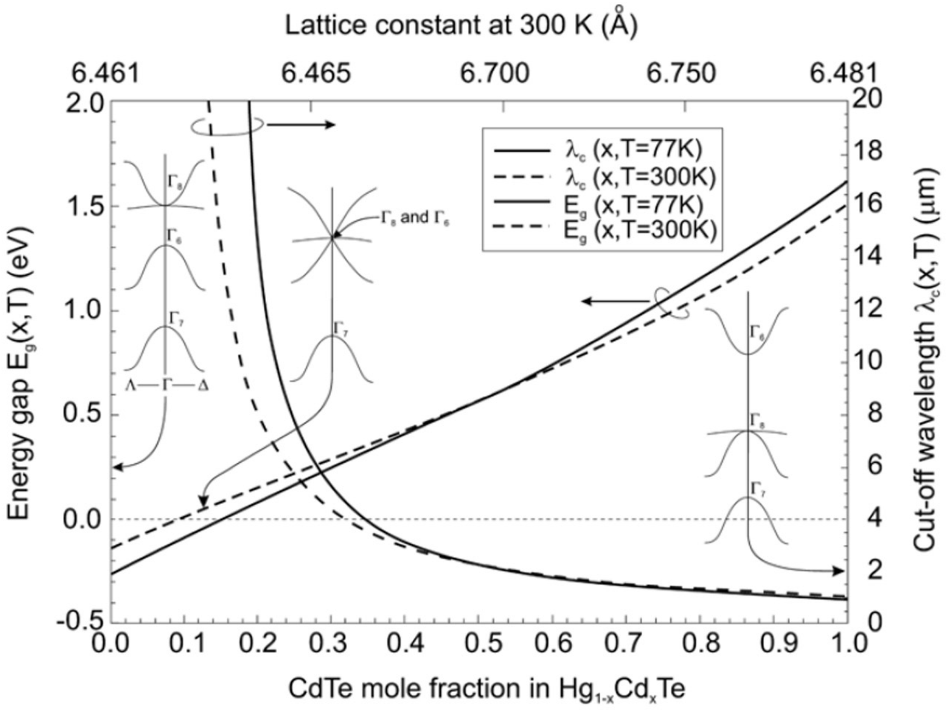

Figure 2.2: Bandgap energy and corresponding cutoff wavelengths of $Hg_{1-x}Cd_xTe$ for varying x and lattice constant values. Calculated bandgap structure near Γ-point for three values (Γ_6, Γ_7, Γ_8) of the forbidden energy gap [6].

2.2 Fundamental Properties of HgCdTe

2.2.1 Band Structure

$Hg_{1-x}Cd_xTe$ is a direct bandgap, zinc-blende, pseudobinary alloy semiconductor of CdTe and HgTe. Due to its semimetallic nature, HgCdTe has a highly tunable bandgap adjustable by the Cd composition x, making it an extremely versatile material for applications over a wide IR range spanning SWIR to VLWIR, as shown in Figures 2.1 and 2.2. The metallic qualities of HgTe characterize HgCdTe with a negative bandgap for $x = 0$; thus, small values of Cd fraction x allow HgCdTe to achieve bandgaps corresponding to cutoff wavelengths in the LWIR and VLWIR spectral regions. Furthermore, HgCdTe exhibits a nominal change in lattice constant over the entire range of x. This attribute is especially beneficial for achieving near-perfect lattice matching of HgCdTe to CdZnTe substrates. The bandgap for $Hg_{1-x}Cd_xTe$ is given by several expressions, the most widely used being that derived by Hansen et al. [35],

$$E_g = -0.302 + 1.93x - 0.81x^2 + 0.832x^3 + 5.35 \times 10^{-4}(1 - 2x)T \tag{2.1}$$

where the bandgap E_g is calculated in units of eV, and the temperature T specified in K.

2.2.2 Electron Affinity

The expression for HgCdTe electron affinity χ (eV) is can be approximated by the following expression [36]

$$\chi(x, T) = 4.23 - 0.813\left[E_g(x, T) - 0.083\right]. \tag{2.2}$$

2.2.3 Intrinsic Carrier Concentration and Effective Mass

The intrinsic carrier concentration n_i (cm^{-3}) of HgCdTe is given by the well-established expression by Hansen and Schmit [37]

$$n_i = (5.585 - 3.82x + 0.001753T - 0.001364xT) \times 10^{14} E_g^{3/4} T^{3/2} exp\left(-\frac{E_g}{2k_BT}\right) \quad (2.3)$$

where E_g (eV) is calculated from Equation 2.1.

The effective electron and light-hole masses, m_e and m_{lh}, respectively, of HgCdTe are close in value and can be calculated using the expression established by Weiler [38] based on the Kane band model,

$$\frac{m_0}{m_e^*} = 1 + 2F + \frac{E_p}{3}\left(\frac{2}{E_g + \frac{1}{E_g+\Delta}}\right) \quad (2.4)$$

where E_p = 19 eV, Δ = 1 eV, and F = -0.8. An approximation of this relationship is also given by $m_e^*/m_0 \approx 0.071\ E_g$ for E_g in eV. Due to the asymmetric bandstructure of HgCdTe as shown in Figure 2.2, the heavy-hole to electron effective mass ratio is high. Commonly, the heavy-hole effective mass value is approximated as $m_{hh}^* = 0.55m_0$ for IR detector modeling. In general, m_{hh}^* values can range from 0.3-0.7m_0.

2.2.4 Carrier Mobility

The high electron carrier mobility of HgCdTe is attributed to the small electron effective mass, on the order of 10^4-10^5 cm^2/Vs. Conversely, heavy-hole mobilities are several orders of magnitude lower. Studies have found that the electron contribution tends to dominate over holes in transport measurements even in *p*-type HgCdTe materials due to high mobility. The large difference in electron and hole mobilities is exploited in HgCdTe detector applications which rely on the speed and influence of G-R mechanisms on carriers such as avalanche photodiodes. The expression for minority carrier electron mobility (cm^2/Vs) based on HgCdTe Hall data [39] is given by [40]

$$\mu_e = \frac{9 \times 10^8 s}{Z^{2r}} \tag{2.5}$$

where

$$\begin{aligned} s &= (0.2/x)^{7.5} \\ r &= (0.2/x)^{0.6} \end{aligned}$$

for compositions in the range of $0.2 \leq x \leq 0.6$ and temperatures $T > 50$ K, where $Z = T$. For $T \leq 50$ K,

$$Z = \frac{1.18 \times 10^5}{2600 - |T - 35|^{2.07}}. \tag{2.6}$$

Hole mobility at 77 K is given by the empirical expression [41]

$$\mu_{hh} = \mu_0 \left[1 + \left(\frac{p}{1.8 \times 10^{17}} \right)^2 \right]^{-1/4} \tag{2.7}$$

where p is the acceptor concentration (cm^{-3}) and $\mu_0 = 440$ cm^2/Vs. The hole mobilities measured around 300 K are found to be weakly dependent on temperature variation and, on the whole, approximately an order of magnitude lower than found for 77 K. For the purposes of detector modeling, the electron-to-hole mobility ratio $b = \mu_e/\mu_{hh} = 100$ is commonly assumed to calculate the hole mobility. These expressions and approximations give a general idea of the carrier mobilities with dependence on Cd composition and temperature. However, it is important to note that the electric field, doping concentration, and presence of impurities and material defects in the HgCdTe material can influence the actual mobility values.

$\mathrm{Hg}_{1-x}\mathrm{Cd}_x\mathrm{Te}$ Material Properties at 77 K			
Properties	$x = 0.2$	$x = 0.3$	$x = 0.4$
Bandgap E_g (eV)	0.083	0.243	0.421
Electron affinity χ (eV)	4.23	4.099	0.3971
Intrinsic carrier concentration n_i (cm^{-3})	9.93×10^{13}	1.18×10^{9}	9.96×10^{3}
Electron effective mass m_e/m_0	0.0063	0.0177	0.0282
Hole effective mass m_{hh}/m_0	0.55	0.55	0.55
Electron mobility μ_e (cm^2/Vs)	1.52×10^{5}	4.74×10^{4}	1.61×10^{4}
Hole mobility μ_{hh} (cm^2/Vs)	1.52×10^{3}	474	161
Static dielectric constant ϵ_0	17.6	16.3	15.2
High frequency dielectric constant ϵ_∞	12.4	11.3	10.3

Table 2.1: Calculated $\mathrm{Hg}_{1-x}\mathrm{Cd}_x\mathrm{Te}$ material parameters at 77 K.

$\mathrm{Hg}_{1-x}\mathrm{Cd}_x\mathrm{Te}$ Material Properties at 300 K			
Properties	$x = 0.2$	$x = 0.3$	$x = 0.4$
Bandgap E_g (eV)	0.155	0.291	0.426
Electron affinity χ (eV)	4.172	4.061	0.3951
Intrinsic carrier concentration n_i (cm^{-3})	3.39×10^{16}	3.60×10^{15}	3.21×10^{14}
Electron effective mass m_e/m_0	0.0114	0.0209	0.0298
Hole effective mass m_{hh}/m_0	0.55	0.55	0.55
Electron mobility μ_e (cm^2/Vs)	1.0×10^{4}	5.61×10^{3}	2.68×10^{3}
Hole mobility μ_{hh} (cm^2/Vs)	100	56.1	26.8
Static dielectric constant ϵ_0	17.6	16.3	15.2
High frequency dielectric constant ϵ_∞	12.4	11.3	10.3

Table 2.2: Calculated $\mathrm{Hg}_{1-x}\mathrm{Cd}_x\mathrm{Te}$ material parameters at 300 K.

2.2.5 Calculated Material Properties

A summary of the HgCdTe material properties at 77 K and 300 K calculated using the analytical and empirical expression described in the previous sections are listed in Tables 2.1 and 2.2.

2.2.6 Optical Properties

The optical properties of HgCdTe are very attractive for optoelectronic applications. However, the absorption coefficients of HgCdTe has been the subject of some debate due to disagreement in the reported results. This discrepancy is attributed to differences in material quality, such as impurities and native defects, composition and doping nonuniformity, and other growth and processing inconsistencies across the conducted studies. Nevertheless, several models [42, 43] for the absorption coefficient have been derived based on semiconductors with similar bandstructure to that of HgCdTe and include the Moss-Burstein shift effect due to doping influences. Measurements of the absorption coefficient performed on high quality short wavelength samples were found to correspond to the Kane model; however, long wavelength samples exhibited some discrepancies due to the appearance of an absorption tail for energies corresponding to those below the material bandgap. A widely used expression for the HgCdTe absorption tail coefficient incorporating a modified Urbach's rule was established by Finkman and Schacham [44] and further described by Hougen [45] for $E_{ph} < E_g$:

$$\alpha(E_{ph}) = \alpha_0 exp\left(\frac{\sigma(E_{ph} - E_0)}{T + T_0}\right) \tag{2.8}$$

in units of cm^{-1},where T is temperature in K, E_{ph} is specified in eV, and

$$\begin{aligned} \alpha_0 &= exp(53.61x - 18.88) \\ E_0 &= -0.3424 + 1.838x + 0.148x^2 \end{aligned}$$

and the fitting parameters are given as T_0=81.9 K and σ=3.267$\times$10^4(1+x) K/eV. For photon energies greater than the bandgap ($E_{ph} > E_g$), a simplified Kane absorption model is used, and the absorption coefficient can be expressed as

$$\alpha(E_{ph}) = \beta(E_{ph} - E_g)^{1/2} \tag{2.9}$$

where

$$\beta = \frac{\alpha_T}{(E_T - E_g)^{1/2}}$$

$$\alpha_T = 100 + 5000x$$

$$E_T = \frac{T_0 + T}{\sigma} ln\left(\frac{\alpha_T}{\alpha_0}\right) + E_0$$

$$E_g = E_T - \frac{0.5}{\frac{\sigma}{T_0+T}}$$

and E_g is approximated from the Urbach tail energy [11].

The direct bandgap nature of HgCdTe results in sharp absorption coefficient curves for given photon energies as shown in Figure 2.3. High absorption coefficients allow HgCdTe detectors to absorb a large percentage of the incoming photons without the need for a thick active layer. This is beneficial for reducing thermal generation and noise caused by excess carriers.

The high frequency dielectric constant ϵ_∞ and the static dielectric constant ϵ_0 are given by [47]

$$\epsilon_\infty = 15.2 - 15.6x + 8.2x^2 \tag{2.10}$$

and

$$\epsilon_0 = 20.5 - 15.6x + 5.7x^2. \tag{2.11}$$

HgCdTe exhibits a moderate dielectric constant which makes the material suitable for integration with circuit elements without increasing the RC time constant, thus

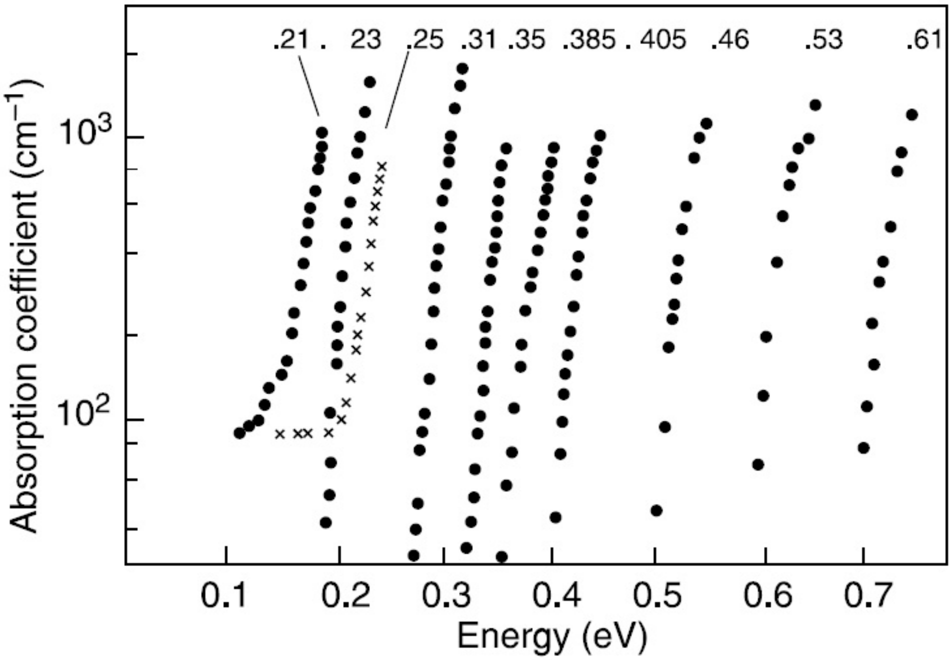

Figure 2.3: Optical absorption coefficient for $Hg_{1-x}Cd_xTe$ for varying x composition as a function of photon energy at room temperature [46].

maintaining short detector response time.

2.2.7 Generation and Recombination Processes

There are three important G-R bulk processes that must be noted because their effects are significant in narrow bandgap semiconductors such as HgCdTe. These are the Shockley–Read–Hall, radiative, and Auger generation processes, shown in Figure 2.4. Carrier generation dominates in the reverse bias mode typical for photodetectors and can significantly influence detector performance by affecting the photon generated signal-to-noise ratio. In order to the address issues related to carrier generation, it is critical to understand the physics behind these mechanisms. The minority carrier lifetimes of the electron-hole pairs resulting from these processes are needed to find the G-R rates, which are then used to calculate the dark current contributions of these mechanisms.

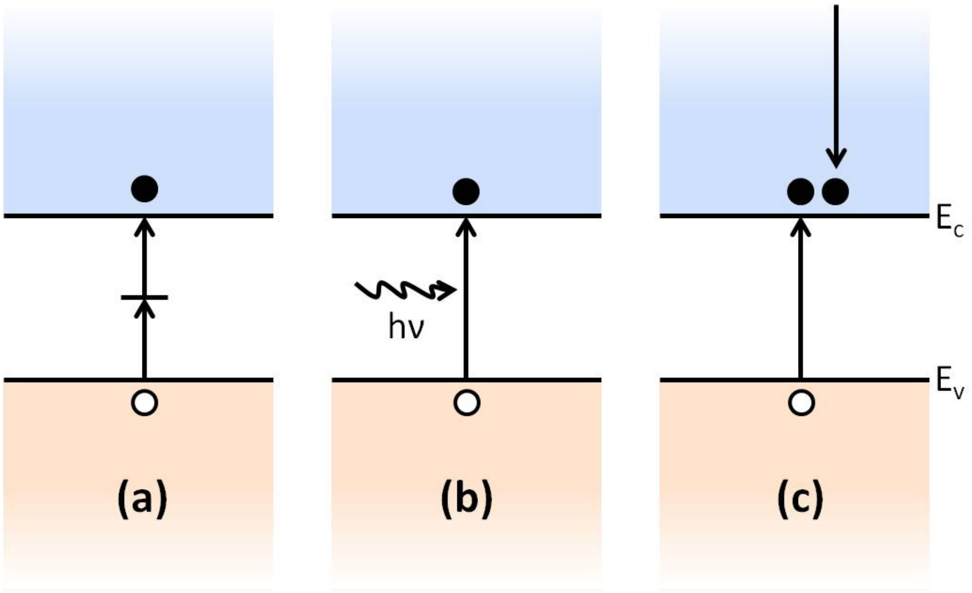

Figure 2.4: Dominant generation mechanisms in narrow bandgap semiconductors: (a) SRH, (b) radiative, and (c) Auger generation.

2.2.7.1 Shockley–Read–Hall Processes

The SRH mechanism illustrated in Figure 2.4a is an extrinsic process; the generation and recombination of electron-hole pairs occurs via intermediate trap states in the forbidden bandgap of a semiconductor material. The trap levels, or SRH centers, can vary in energy and range in position from anywhere near the valence band to near the conduction band. SRH centers are typically introduced by lattice defects or foreign impurities, often a result of processing techniques and material quality and purity. The SRH recombination rate ($\mathrm{cm^{-3}s^{-1}}$) can be determined by accounting for the electron and hole capture cross-sections σ_n and σ_p ($\mathrm{cm^2}$), respectively, yielding [6]

$$R_{net}^{SRH} = \frac{\sigma_n \sigma_p v_{th}(n_0 p_0 - np) N_{trap}}{\sigma_n(n + n_1) + \sigma_p(p + p_1)} \tag{2.12}$$

where the carrier concentrations n_1 and p_1 ($\mathrm{cm^{-3}}$) for the Fermi level coincident in the trap level are given by

$$n_1 = N_c exp\left[-\frac{E_{trap}}{k_B T}\right] \tag{2.13}$$

and

$$p_1 = N_v exp\left[-\frac{(E_g - E_{trap})}{k_B T}\right] \tag{2.14}$$

where N_t is the trap density (cm^{-3}), E_{trap} is the trap level relative to the conduction band (eV), and v_{th} is the carrier thermal velocity (cm/s). The carrier concentrations n_1 and p_1 can also be calculated for the Fermi level at E_{trap} referenced from the valence band by assuming Boltzmann statistics and a parabolic valence band:

$$n_1 = \frac{n_i^2}{p_1} \tag{2.15}$$

where

$$p_1 = 2.51 \times 10^{19} \left(\frac{m_{hh} T}{300}\right)^{3/2} exp\left(\frac{-E_{trap}}{k_B T}\right). \tag{2.16}$$

The trap-limited minority carrier lifetime of a hole in n-type material is given by

$$\tau_{p0} = (\sigma_p v_{th} N_t)^{-1} \tag{2.17}$$

while the minority carrier lifetime of an electron in p-type material can be given by

$$\tau_{n0} = (\sigma_n v_{th} N_t)^{-1}. \tag{2.18}$$

Then, the minority carrier SRH lifetime [48] is expressed as

$$\tau_{SRH} = \frac{\tau_{n0}(p_0 + p_1) + \tau_{p0}(n_0 + n_1)}{p_0 + n_0} \tag{2.19}$$

where τ_{n0} and τ_{p0} are the electron and hole minority carrier lifetimes (s) in bulk material, and n_0 and p_0 are the electron and hole equilibrium carrier concentrations (cm^{-3}), respectively.

In the device model described in the next chapter, the net SRH recombination rate (cm^{-3}s^{-1}) is calculated by [49]

$$R_{net}^{SRH} = \frac{np - n_i^2}{\tau_{n0}(n + n_1) + \tau_{p0}(p + p_1)} \tag{2.20}$$

with

$$n_1 = n_i exp\left(\frac{E_{trap}}{k_B T}\right) \tag{2.21}$$

$$p_1 = n_i exp\left(-\frac{E_{trap}}{k_B T}\right) \tag{2.22}$$

where τ_{n0} and τ_{p0} are the user-defined electron and hole SRH minority carrier lifetimes, respectively, and E_{trap} is the the trap energy relative to the intrinsic Fermi level.

2.2.7.2 Radiative Processes

Radiative generation and recombination are intrinsic mechanisms that depend on the bandstructure of the material; direct bandgap semiconductors exhibit radiative processes due to the high probability of carriers transitioning from the conduction to valence band, or vice versa, without violating the conservation of momentum. Radiative recombination occurs when an electron and hole recombine, resulting in the emission of a photon due to the excess energy. Conversely, radiative generation takes place in the reverse fashion, that is, the absorption of a photon with energy greater than or equal to the material bandgap creates an electron-hole pair as shown in Figure 2.4b.

The radiative lifetime due to external photon absorption and emission can be expressed as

$$\tau_{rad} = \frac{n_i^2}{B_0(n_0 + p_0)} \tag{2.23}$$

where the radiative generation-recombination coefficient B_0 ($\mathrm{cm^3 s^{-1}}$) for is given by [50]

$$\begin{aligned} B_0 = 5.8 \times 10^{-13} \sqrt{\epsilon_\infty} \left(\frac{m_0}{m_e + m_{hh}} \right)^{3/2} \left(1 + \frac{m_0}{m_e} + \frac{m_0}{m_{hh}} \right) \left(\frac{300}{T} \right)^{3/2} \cdot \\ (E_g^2 + 3k_BTE_g + 3.75(k_BT)^2). \end{aligned} \tag{2.24}$$

The radiative recombination rate ($\mathrm{cm^{-3} s^{-1}}$)is expressed as

$$R_{net}^{rad} = B_0(np - n_i^2). \tag{2.25}$$

B_0 is based on the theoretical expression for the absorption coefficient as a function of photon energy, and the bandgap E_g is specified in units of eV. Typically, photons which are emitted in the material as a result of radiative decay are immediately reabsorbed. As a result, the radiative carrier lifetime, measured by the number of escaped photons, often increases depending on the geometry of the structure and material quality. Furthermore, the detector may absorb photons emitted by other devices or passive components of the associated device structure. IR detector performance is fundamentally limited when the radiative generation is primarily due to scene-induced photons.

2.2.7.3 Auger Processes

Intrinsic Auger processes are an important G-R mechanism, especially in narrow bandgap materials where their contributions are more pronounced. Ten types of Auger processes have been identified for semiconductors with the typical arrangement of three energy bands: the conduction band, and the heavy- and light-hole valence bands [1]. The two most notable mechanisms are Auger 1 and Auger 7, shown in Figure 2.5, due to their small threshold energy and large density of states conducive to more carrier-to-carrier interaction [2].

Auger 1, also called the CHCC mechanism, occurs via interaction of two electrons and a heavy-hole. In the case of carrier recombination, the elimination of a heavy-hole-electron pair transfers kinetic energy such that an electron in the conduction band is excited to a higher state. In the reverse case (generation), an electron in the conduction band loses energy via impact ionization, exciting an electron from the heavy-hole band to the conduction band and creating a minority carrier hole in the process. The Auger 1 mechanism is well established to be dominant in n-type HgCdTe materials, especially at high temperatures. Interestingly, the Auger 1 process exhibits unique behavior for degenerately doped n-type materials. With degenerate doping, the Fermi level shifts high into the conduction band due to the low density of states, reducing the concentration of minority carrier holes. This results in an increase in the threshold energy and suppresses Auger 1 processes in highly doped n-type HgCdTe.

The Auger 1 recombination lifetime (s), assuming m_e/m_{hh} <<1, is given by

$$\tau_{A1} = \frac{1}{(n_0 + p_0)(B_1 n_0 + B_2 p_0)} \tag{2.26}$$

where the generation-recombination coefficient B_1 (cm^{6}s^{-1}) is

$$B_1 = \frac{1}{2n_i^2 \tau_{A1}^i} \tag{2.27}$$

and the Auger 1 intrinsic recombination time τ_{A1}^i (s) is defined as [51]

$$\tau_{A1}^i = \frac{3.8 \times 10^{-18} \epsilon_\infty^2 \sqrt{1+\mu}(1+2\mu)}{\frac{m_e}{m_0} |F_1 F_2|^2 \left(\frac{k_B T}{E_g}\right)^{3/2}} exp\left[\left(\frac{1+2\mu}{1+\mu}\right)\frac{E_g}{k_B T}\right] \tag{2.28}$$

where F_1F_2 is the overlap matrix integral ranging in value between 0.1-0.3 [1]. Here,

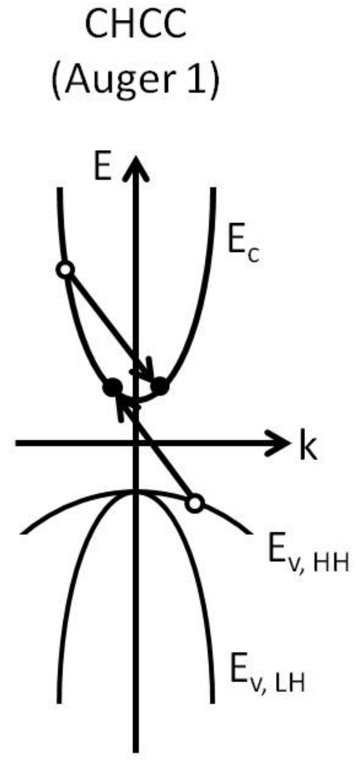

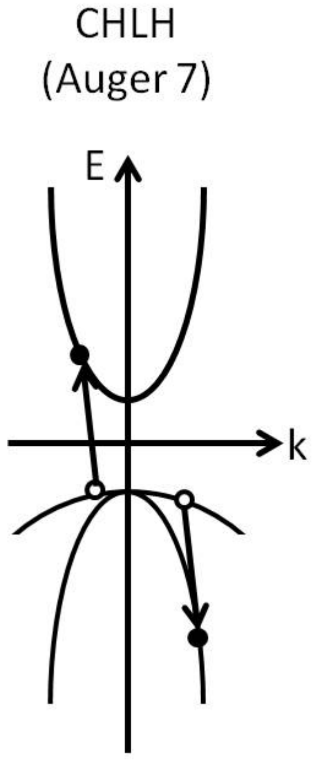

Figure 2.5: Auger 1 and Auger 7 generation processes. Arrows indicate carrier transition; filled and empty circles indicate occupied and unoccupied states, respectively.

μ is the carrier mass ratio

$$\mu = \frac{m_e}{m_{hh}} \tag{2.29}$$

and the second Auger generation-recombination coefficient B_2 (cm^{6}s^{-1}) is

$$B_{2(A1)} = \frac{\sqrt{\mu}(1+2\mu)}{2+\mu} exp\left[-\left(\frac{1-\mu}{1+\mu}\right)\frac{E_g}{k_B T}\right] B_1 = B_A B_1. \tag{2.30}$$

However, the B_A term, which refers to hole-hole collisions, is usually neglected.

The Auger 7 process, known as the CHLH mechanism, is dominant in *p*-type HgCdTe and involves a heavy-hole, a light-hole, and an electron. In the Auger 7 recombination process, an electron in the conduction band eliminates a heavy-hole, and the transferred kinetic energy excites a heavy-hole to the light-hole valence band. In the case of generation, a light-hole transitions to the heavy-hole valence band, and the excess energy creates a heavy-hole-electron pair. Unlike Auger 1, Auger 7 is not affected by degenerate *p*-type doping due to the high density of states. Auger 7 is strongly dependent on temperature and bandgap energy, exhibiting heat-stimulated transitions at higher temperatures and in narrow bandgap materials. The lifetime for Auger 7 processes is calculated in a similar manner to Auger 1; however, to incorporate the Auger 7 mechanism, B_2 is modified to

$$B_{2(A7)} = \left(B_A + \frac{1}{\gamma_{mult}\gamma}\right) B_1 \tag{2.31}$$

where

$$\gamma = \frac{\tau^i_{A7}}{\tau^i_{A1}} = \gamma' \left(\frac{1 - \frac{5k_B T}{4E_g}}{1 - \frac{3k_B T}{2E_g}}\right). \tag{2.32}$$

γ' is approximately 6 based on Kane's nonparabolic band approximation, and the intrinsic Auger lifetime ratio γ is reported within the range of 3-60 [52–54]. The value of the Auger lifetime ratio has been long debated, thus the parameter γ_{mult} can be used to adjust the value appropriately in device modeling.

The net Auger recombination rate (cm^{-3}s^{-1}) [55] can be expressed as

$$R_{net}^{Aug} = (B_1 n + B_2 p)(np - n_i^2). \tag{2.33}$$

2.2.7.4 Carrier Lifetimes

The total carrier lifetime τ_{tot} can be calculated from the independent lifetimes attributed to each recombination mechanism using Matthiessen's rule. The sum of all contributions is given by

$$\frac{1}{\tau_{tot}} = \frac{1}{\tau_{SRH}} + \frac{1}{\tau_{rad}} + \frac{1}{\tau_{A1}} + \frac{1}{\tau_{A7}}. \tag{2.34}$$

Figure 2.6 illustrates theoretical and experimental lifetimes data for an *n*-type (N_D=6.6×10^{14} cm^{-3}) MOCVD Hg$_{0.773}$Cd$_{0.227}$Te sample as a function of temperature. The net carrier lifetime in the LWIR material follows an Auger 1 dependence for temperatures above 200 K, while SRH mechanisms dominate at lower temperatures. Figure 2.7 similarly illustrates the experimentally obtained carrier lifetimes in LWIR HgCdTe dominated by intrinsic Auger mechanisms at higher temperatures and extrinsic SRH mechanisms at lower temperatures. As shown in both studies, radiative recombination lifetimes are relatively high, and materials for high performance IR applications should ideally be limited by intrinsic radiative G-R rather than by Auger or SRH processes.

2.3 MBE Growth of HgCdTe Epilayers

Recently, HgCdTe growth using epitaxial techniques such as liquid phase epitaxy (LPE), metalorganic chemical vapor deposition (MOCVD), and MBE has been of

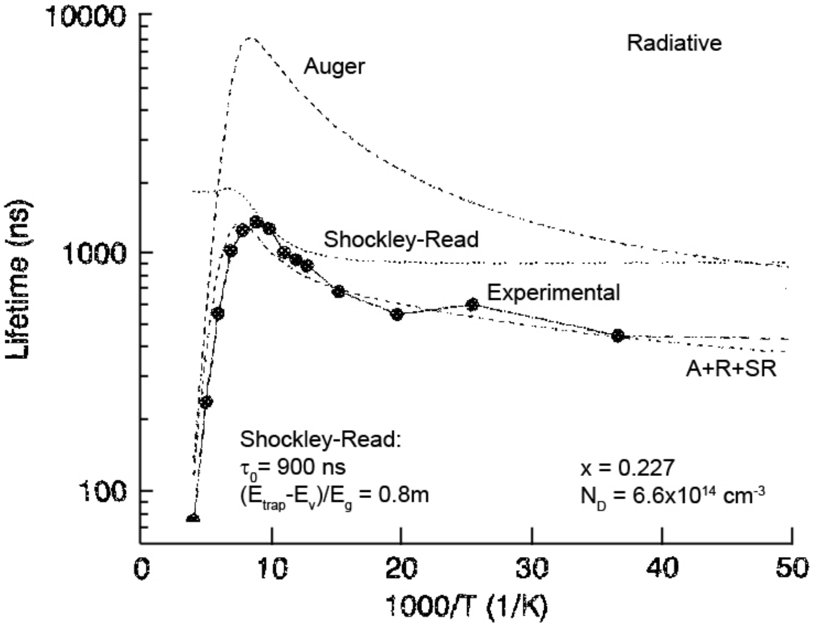

Figure 2.6: Carrier lifetimes in *n*-type (N_D=6.6×10^{14} cm^{-3}) MOCVD $Hg_{0.773}Cd_{0.227}Te$ grown on GaAs as a function of temperature. Adapted from Ref. [56].

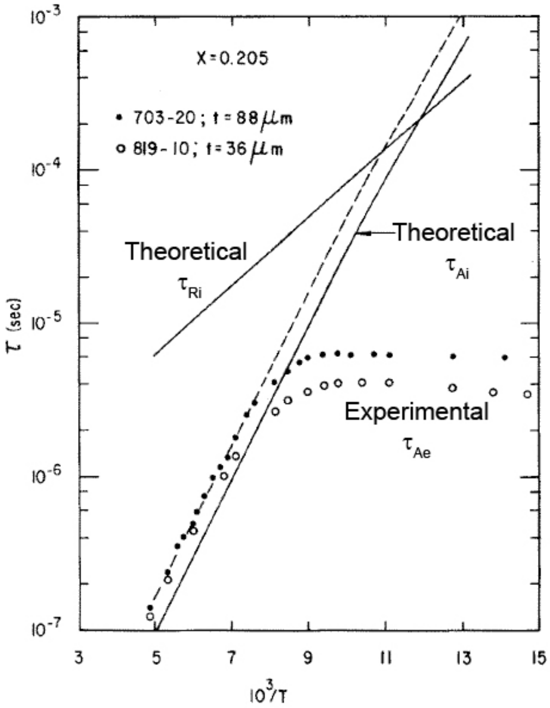

Figure 2.7: Carrier lifetimes in *n*-type (N_D=1.7×10^{14} cm^{-3}) MOCVD $Hg_{0.795}Cd_{0.205}Te$ sample as a function of temperature. Adapted from Ref. [57].

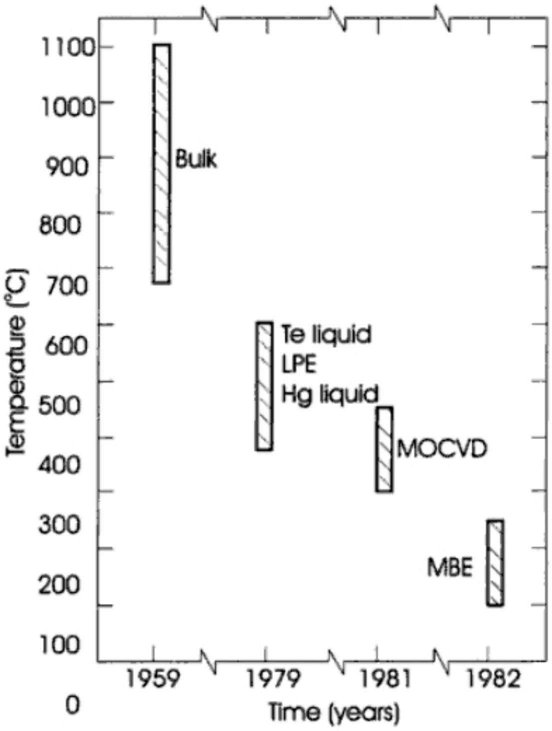

Figure 2.8: Temperature ranges for HgCdTe growth using bulk and epitaxial growth techniques [2].

increasing interest for second- and third-generation detectors [2]. Compared to bulk growth techniques, epitaxial methods offer a number of advantages including the possibility to grow large-area (<30 cm^2) layers and well-controlled layer structures with good lateral homogeneity and abrupt and complex composition and doping profiles. Furthermore, epitaxial growth is performed at low temperatures, making it possible to reduce the native defect density and prevent interdiffusion in the epilayers. Figure 2.8 illustrates the growth temperature ranges for bulk and epitaxial techniques.

The IR industry requires rapid cycle time, low-volume production, and flexible manufacturing of affordable, high performance IR FPAs. Many of the FPA applications impose strict dimensional requirements which can only be met by exercising precise control over growth parameters such as the layer thickness, composition and doping profiles, and doping uniformity.

MBE technology is particularly suited to meet the needs of high performance

IR applications, as it employs low temperature HgCdTe growth under an ultra-high vacuum environment, offers the capabilities for *in situ* *n*-type and *p*-type doping, and allows excellent control over compositional, doping, and interfacial profiles. MBE is one of the most common techniques used to grow epitaxial HgCdTe layers in the United States.

2.3.1 HgCdTe by MBE Growth

MBE growth is performed in an ultra-high vacuum chamber to minimize contamination. The beams of atoms and molecules of the source materials travel in nearly collision-free paths until they arrive at the substrate. MBE is characterized by a slow deposition rate around 1-3 monolayers/s which allows layers to grow epitaxially. The epilayer growth is strongly moderated by surface kinetics and chemistry. The incident atoms become weakly chemically bonded or physically adsorbed to the substrate surface, migrating along the surface with sufficient energy. The temperature of the substrate is held moderately high to provide thermal energy to the atoms for surface propagation. The atom beams can also be turned 'on' or 'off' within a fraction of a second by shuttering the sources, allowing nearly atomically abrupt transitions of the compositional flux within the growth of a monolayer [11]. This capability is especially useful for achieving complex, multi-layer heterostructure devices which require careful control over structural parameters.

MBE HgCdTe epilayers are grown from material sources, or effusion cells, individually containing Hg, Te_2, and CdTe, which are heated independently to achieve a target material flux. The optimal temperature range for MBE HgCdTe growth is 185-190°C. The growth window for HgCdTe is very small because the Hg sticking coefficient is much lower than those of Cd and Te. Typically, the growth temperature should be controlled within ±3°C and the Hg flux within ±5%. The Cd composition must be controlled within ±0.002 to obtain the target cutoff wavelength within ±6%

[11]. It is therefore critical to monitor the the layers *in situ* during growth. Moreover, the growth temperature at the surface of the epilayers influences the presence of extended defects. Surface temperatures which are below the optimal growth condition (<185°C) can result in the accumulation of excess Hg at the surface as the sticking coefficient of the Hg increases with reduced temperatures, causing microtwin defects. The presence of microtwin defects can degrade the electrical properties of the layers and the associated devices. Etch pit density (EPD) values of such materials are typically in the 10^6-10^7 cm^{-2} range. On the other hand, growth temperatures above 190°C can result in out-diffusion of Hg at the surface, creating Hg vacancies and facilitating the formation of void defects. Under optimized growth conditions, the lowest void concentration observed in HgCdTe epilayers is around 100 cm^{-2}. The EPD values of high quality, low defect layers is on the order of 10^4-10^5 cm^{-2} [2].

2.3.2 Native Defects

In HgCdTe, the dominant native defect is the double-ionized acceptor related to the metal lattice vacancies. Undoped as-grown HgCdTe materials exhibit *p*-type conductivity with the hole concentration related to the number of Hg vacancies which is associated with the Cd composition, growth temperature, and Hg partial pressure $P(Hg)$. The hole concentration as a function of the Hg partial pressure is shown in Figure 2.9 and exhibits a $1/P(Hg)$ dependence of the native acceptor concentration. This demonstrates that annealing the HgCdTe material under a Hg overpressure reduces the hole concentration by filling the vacancies. Samples that are annealed at low temperatures and high $P(Hg)$ should exhibit low hole concentrations. Native defects can affect diffusion behavior as they have very high mobilities at low temperatures which correspond to diffusion constants on the order of 10^{-10} cm^{-2}/s. Vacancy diffusion is further enhanced in the presence of dislocations in the HgCdTe material [11].

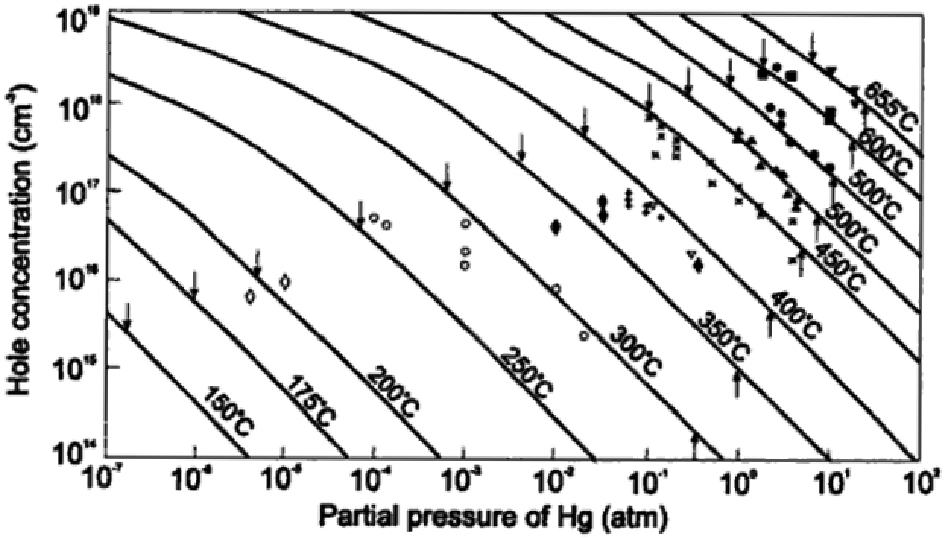

Figure 2.9: 77 K hole concentration of $Hg_{0.8}Cd_{0.2}Te$ as a function Hg partial pressure $P(Hg)$ and annealing temperature for bulk (400 to 655°C) and epilayer (150 to 400°C) samples. Solid curves calculated based on defect model, arrows indicate region of material existence [58].

In the presence of impurities, low temperature (<300°C) annealing of HgCdTe under Hg overpressure can reveal the background concentration of defects. Samples with high residual donor concentrations will exhibit *n*-type conductivity.

During the cooling from high preparation temperatures to room temperature, Te precipitates can form in HgCdTe due to the inability of the material to incorporate the large excess in deviation from stoichiometry. Annealing HgCdTe at higher temperatures in a Hg rich ambient can reduce these precipitates and prevent the multiplication of dislocations. Te precipitates are typically formed during cooling after high temperature processes in Hg deficient environments and may arise in MBE grown materials because of the presence of Te in CdTe and CdZnTe. Precipitates are believed to contribute to G-R trap centers and may also assist in tunneling, resulting in higher dark currents in photodiodes [2].

2.3.3 Dopants

Well controlled, stable *in situ* n-type extrinsic doping of MBE grown HgCdTe is easily achieved for concentrations in the range of 10^{14}-10^{19} cm^{-3}. Indium is most commonly used for n-type doping of HgCdTe due to its high solubility and moderately high diffusion coefficient. While low temperature, post-growth anneals are useful for enhancing the electronic properties of doped epilayers, they are not necessary for the activation of In dopants. For concentrations up to 10^{17} cm^{-3}, near 100% donor efficiency has been reported for epitaxial layers grown by MBE [2]. However, if the In doping concentration is lower than the native defect (Hg vacancy) density, the p-type Hg vacancies can compensate the n-type dopant concentration and significantly reduce the carrier mobility and control of doping. This issue can be addressed by annealing the HgCdTe material at low temperatures (<300°C) [2, 11] under Hg overpressure to eliminate the Hg vacancies.

Acceptor doping is particularly challenging in MBE grown HgCdTe. Intrinsic doping via Hg vacancies is not ideal for several reasons. Firstly, the Hg vacancy concentration profile cannot be well-controlled as the vacancies are not stable against diffusion. Moreover, the native defects can also degrade carrier mobilities. Finally, Hg vacancies can act as SRH trap centers, reducing carrier lifetimes. Thus, p-type doping must be achieved using extrinsic dopants. Elements from both group I and group V can act as acceptors sitting in the cation (Hg, Cd) or anion (Te) lattice sites, respectively. Early studies report that while group I atoms exhibit near 100% dopant activation, as well as excellent transport properties and recombination times, they diffuse out of the doped region during further MBE growth or post-growth annealing. Such behavior is unacceptable for the stable doping and abrupt junction profiles required for IR detectors and negates the usefulness of group I elements as acceptor dopants [2].

On the other hand, *in situ* and *ex situ* doping using group V elements poses its own set of challenges. Ion implantation methods have been shown to cause material defects [21–24] which can reduce minority carrier lifetimes and carrier mobilities. Furthermore, achieving well-controlled, abrupt junction profiles required for certain detector architectures can be difficult with implantation and in-diffusion techniques. Because HgCdTe MBE growth is performed under Te rich conditions, HgCdTe materials are dominated by Hg vacancies, and group V dopants are more likely to sit on the cation (Hg) sublattice, acting as donors rather than acceptors. The dopants must therefore be activated by a standard high temperature anneal (~425°C, 10 min), followed by a lower temperature (250°C, 24 h) Hg vacancy annihilation anneal to fill the Hg cation sites [11].

Arsenic (As) is the preferred *p*-type dopant in HgCdTe due to its large atom size and low diffusion coefficient which allows for stable, better controlled junction formation. During the activation anneal, the high temperature evaporates the Te atoms from the epilayers, allowing the As dopants to transfer to the anion lattice sites. This process typically results in near complete activation for As dopant concentrations up to greater than 10^{18} cm^{-3}. However, the activation anneal negates many of the advantages of low temperature HgCdTe MBE growth. Some efforts have been made to achieve *p*-type doping in as-grown HgCdTe materials by controlling the flow and alternating the shutter pattern of the As, Hg, CdTe, and Te source fluxes during growth [59]. Full *p*-type As activation in as-grown HgCdTe [59] or after low temperature (<300 °C) anneals [60, 61] have been reported using this method.

2.4 Summary

As discussed, HgCdTe is an important material for high performance IR photodetectors and continues to outperform competing materials, achieving near theoretical performance limits. Properties such as the high absorption coefficient, high carrier mobility, and lattice matched bandgap tunability make HgCdTe an especially attractive option for IR detector applications. However, extrinsic and intrinsic G-R processes such as SRH, radiative, and Auger mechanisms are major factors which affect detector performance in narrow bandgap materials and must be taken into account. The analytical and empirical expressions of the fundamental HgCdTe properties presented in this chapter are used in the HgCdTe device modeling described in Chapter III. While there are alternative expressions available for certain material properties, those detailed in this chapter reflect what is widely used in the field.

Furthermore, MBE is quickly becoming the preferred technology for achieving advanced detector architectures for HgCdTe IR FPA applications. HgCdTe epilayers grown by MBE can be precisely controlled to produce complex heterostructures made of high quality material. HgCdTe MBE technology has developed to the extent where the quality of the HgCdTe epilayers grown on lattice-matched bulk CdZnTe substrates now depend on the substrate itself. One of the remaining challenges of MBE grown HgCdTe is achieving high quality, well-controlled, stable *p*-type doping.

CHAPTER III

HgCdTe Device Model

3.1 Overview of Device Modeling

A significant portion of this work relies on numerical device modeling to predict and analyze the performance characteristics of various alternative detector structures. Numerical modeling is preferred over analytical modeling for simulating multi-layer structures because it provides a more realistic account of device behavior by incorporating variations in geometric and material parameters. This is especially useful for designing new detector architectures for which analytical models have not been developed.

In this study, device design and optimization calculations were performed using the commercial software Sentaurus Device, a package within the Synopsys TCAD tool suite. Sentaurus Device is an advanced, general purpose device simulator that numerically models the electrical behavior of a single semiconductor device by discretizing the physical properties of the material into a non-uniform mesh of nodes [49]. The classical drift-diffusion transport model is implemented to simulate devices based on the $Hg_{1-x}Cd_xTe$ compound semiconductor. Empirical expressions of HgCdTe material parameters, as well as recombination mechanisms and rates described in the previous chapter, are incorporated into the device model to improve accuracy.

3.2 Simulation Methodology

3.2.1 Transport Model

The carrier transport in the semiconductor is simulated by implementing the widely used drift-diffusion model defined by the governing Poisson and current continuity equations. The Poisson equation is given by

$$\nabla \cdot \epsilon \phi = -q(p - n + N_D - N_A) - \rho_{trap} \tag{3.1}$$

where ϵ is the electrical permittivity (F/m), ϕ is the electrostatic potential (V), q is the elementary electronic charge (C), p and n are the hole and electron concentrations (cm^{-3}), respectively, N_D is the ionized donor concentration (cm^{-3}), N_A is the ionized acceptor concentration (cm^{-3}), and ρ_{trap} is the charge density attributed to traps and fixed charges (cm^{-3}). The electron and hole continuity equations represent the conservation of particles and are expressed as

$$\nabla \cdot \overrightarrow{J}_n = qR_{net} + q\frac{\partial n}{\partial t} \tag{3.2}$$

$$-\nabla \cdot \overrightarrow{J}_p = qR_{net} + q\frac{\partial p}{\partial t} \tag{3.3}$$

where $\overrightarrow{J}_n$ and $\overrightarrow{J}_p$ are the electron and hole current densities (A/cm^2), respectively, and R_{net} is the net electron-hole recombination rate (cm^{-3}s^{-1}). In HgCdTe, the net recombination rate is the usually taken as the sum of the net SRH, Auger, and radiative G-R rates, as defined and discussed in the previous chapter.

The electron and hole current densities are given by

$$\overrightarrow{J}_n = -nq\mu_n \nabla \Phi_n \tag{3.4}$$

$$\overrightarrow{J}_p = -pq\mu_p \nabla \Phi_p \tag{3.5}$$

where μ_n and μ_p are the electron and hole mobilities (cm^2/Vs) and Φ_n and Φ_p are the electron and hole quasi-Fermi potentials (V), respectively.

Full coupled solutions of the Poisson's equation and electron and hole current continuity equations are determined using a Newton-method solver [49]. The partial differential equations are discretized over the simulation grid and solved at each node within the device geometry. The steady-state numerical calculations are performed using an iterative algorithm in which a linear system is solved at each step in the simulation.

3.2.2 Boundary Conditions

Dirichlet boundary conditions were applied at the ohmic contacts, where charge neutrality and equilibrium conditions are assumed. The boundary values are fixed for the surface potential Φ_s and surface electron and hole concentrations n_s and p_s, respectively. The charge neutrality and equilibrium conditions at the surface are given by

$$n_s - p_s = N_D - N_A \tag{3.6}$$

and

$$n_s p_s = n_{i,eff}^2. \tag{3.7}$$

At the surface, the quasi-Fermi potentials for electrons Φ_n and holes Φ_p are equal and set to the applied bias of the electrode.

3.2.3 Optical Generation in Heterostructure

In a heterostructure HgCdTe device, the optical absorption of the incident photons will vary depending on the photon wavelength and Cd composition of the material. Thus, the change in absorption coefficient over the structure must be included in the optical generation rate G_{opt}. For example, Figure 3.1 illustrates a simple, two-layer $Hg_{1-x}Cd_xTe$ heterostructure with layers Region 1 (x_1) and Region 2 (x_2). Assuming a uniform absorption coefficient $\alpha(x,\lambda)$ (cm^{-1}) in each region and illumination with photon flux ϕ (W/cm^2) and energy E_{ph} (J) at y_0, G_{opt} ($cm^{-3}s^{-1}$) is then given by

$$G_{opt} = \begin{cases} \frac{\phi}{E_{ph(\lambda)}} \times \alpha(x_1,\lambda) e^{-\alpha(x_1,\lambda)} y & 0 \le y \le y_1 \\ \frac{\phi}{E_{ph(\lambda)}} \times \alpha(x_2,\lambda) e^{-\alpha(x_1,\lambda)} e^{-\alpha(x_2,\lambda)} (y - y_1) & y_1 \le y \le y_2 \end{cases} \tag{3.8}$$

3.2.4 Incorporating HgCdTe Material Parameters

The analytical and empirical expressions of HgCdTe material parameters described in Chapter II are incorporated in the device model. Mole fraction dependent properties such as the $Hg_{1-x}Cd_xTe$ bandgap, electron affinity, dielectric constant, and absorption coefficient are calculated using a cubic spline interpolation [49], while the electron and hole mobilities and electron effective mass are calculated using a linear interpolation. An individual material parameter set is defined for each region of the device, allowing the user to separately modify the properties in each layer of a heterostructure design.

3.3 Carrier Statistics

The HgCdTe numerical model incorporates Fermi-Dirac statistics for parabolic bands. The electron and hole densities (cm^{-3}) are given by

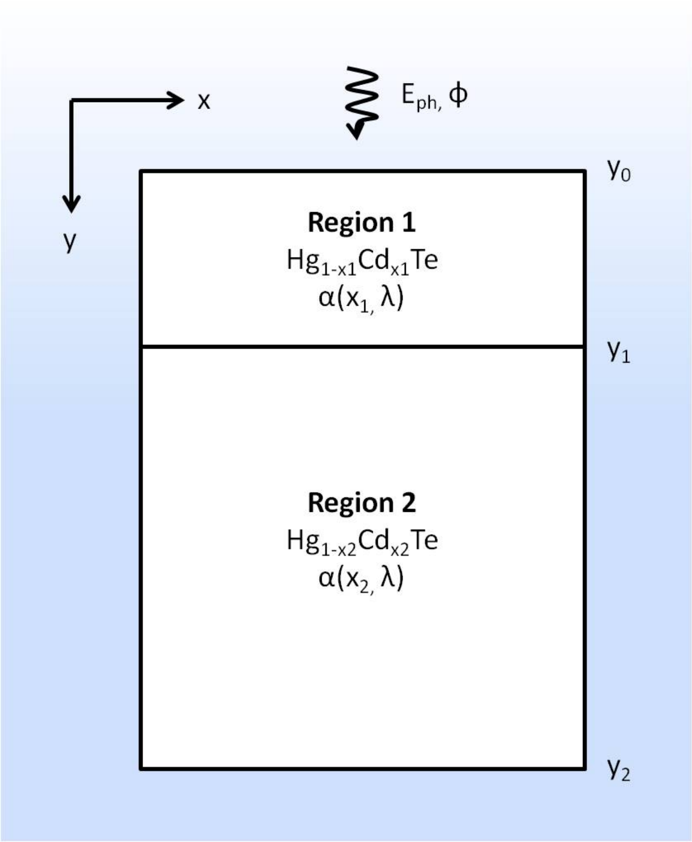

Figure 3.1: $\mathrm{Hg}_{1-x}\mathrm{Cd}_xTe$ heterostructure with different absorption coefficient (α) in each region.

$$n = N_c F_{1/2}\left(\frac{E_{F,n} - E_c}{k_B T}\right) \tag{3.9}$$

and

$$p = N_v F_{1/2}\left(\frac{E_v - E_{F,p}}{k_B T}\right) \tag{3.10}$$

where $E_{F,n}$ and $E_{F,p}$ are the quasi-Fermi energies of electrons and holes (eV), respectively, and $F_{1/2}$ is the Fermi integral of order 1/2.

3.4 Model Validation

p-*n* homojunction and DLPH structures were constructed in Sentaurus Device, as shown in Figure 3.2. These structures consist of two layers: a highly doped *p*-type cap layer (wide bandgap, $x_1 > x_2$ for DLPH) (Region 1) and a lightly doped *n*-type absorber layer (Region 2). The device model assumed step doping profiles (100% donor and acceptor ionization) with the electrical junction coinciding with the metallurgical junction. Series resistance and surface recombination effects in the device were neglected. In simulations involving optical illumination, the incident light source was defined to be 0.1 μm away from the top surface. Anti-reflective properties were not specified at the optical entrance, but the reflectivity at the junction interfaces was defined to be zero.

The parameters used to define the properties of each $Hg_{1-x}Cd_xTe$ layer are

- t (μm): layer thickness
- N_D, N_A (cm^{-3}): donor and acceptor doping concentrations, respectively (assuming 100% ionization)
- x: Cd alloy fraction

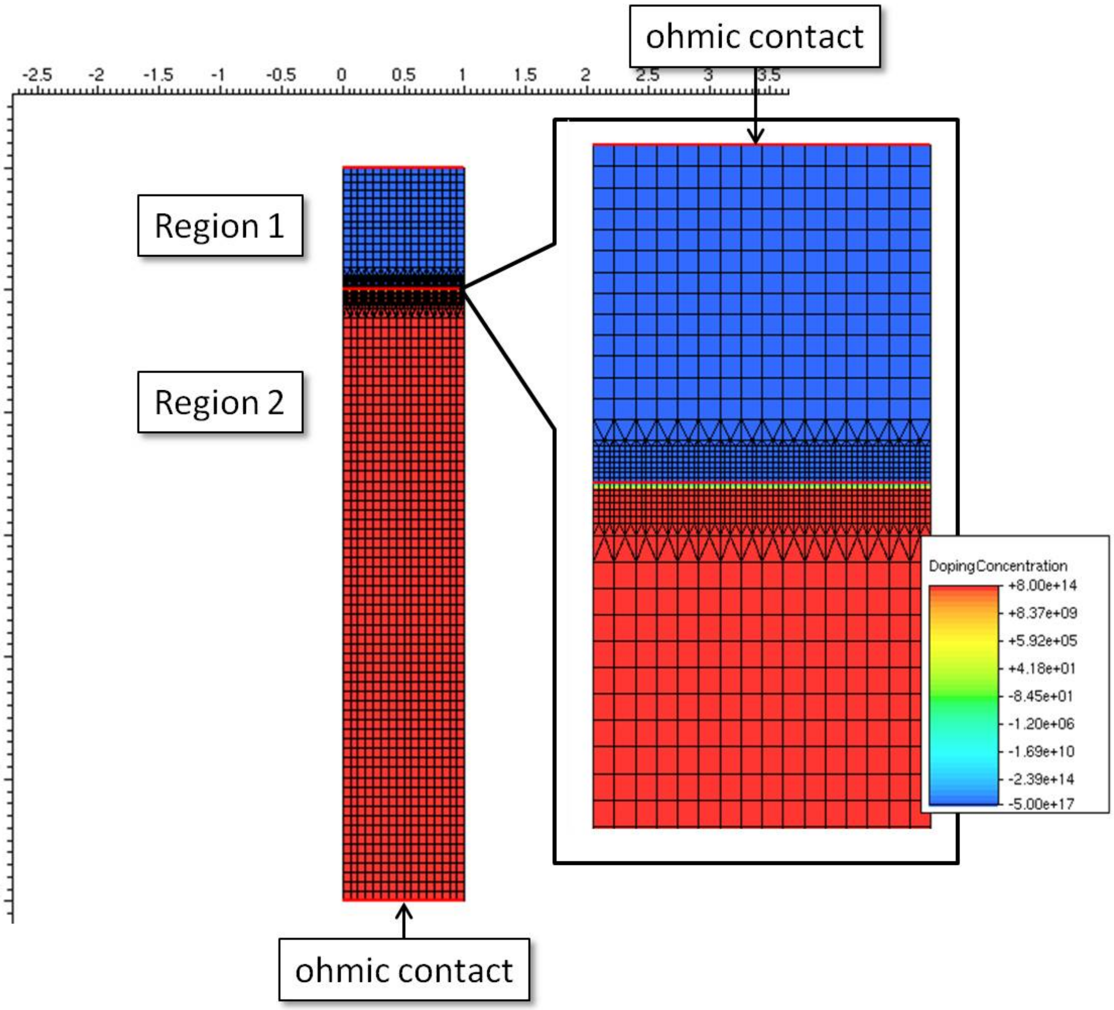

Figure 3.2: Geometric boundary and mesh structure of sample HgCdTe p-n homojunction photodiode. Palette indicates doping concentration and polarity.

- k: ratio of hole to electron mobility (commonly set to $0.01\mu_e$ for modeling)
- F_1F_2: Auger 1 matrix overlap integral between values of 0.1-0.3
- γ: Auger 7 to Auger-1 intrinsic carrier lifetime ratio between values of 3-60 (defined as 6 throughout this study with γ_{mult}=1)
- E_{trap} (eV): SRH trap level relative to the intrinsic Fermi level E_i
- τ_{n0}, τ_{p0} (s): SRH minority carrier lifetimes for electrons and holes, respectively

The device parameters were obtained by back-extracting the values used to fit the calculated current-voltage characteristics for the *p*-*n* homojunction and DLPH devices to experimental data [62–65]. The SRH minority carrier lifetimes and E_{trap} values were used as primary fitting parameters. Varying τ_{n0} and τ_{p0} was found to significantly affect the overall magnitude of J_{dark}, and the values were used to fit selected current-voltage data [63]. The E_{trap} value was adjusted to fine-tune the dark current value to match the temperature-dependent behavior for MWIR and LWIR cutoff devices. The F_1F_2 overlap matrix integral was determined by sweeping through values in the accepted range of 0.1 to 0.3 and comparing the dark current density values to those obtained for respective MWIR and LWIR data. The F_1F_2 parameter did not significantly affect the dark current density in the *p*-*n* diodes, and the final value was selected based on that obtained in a past fitting study [66].

The Cd composition x of the absorber layer was determined by calculating the bandgap required to achieve the target cutoff wavelength for photons with energy E_{ph} using the relation $E_{ph}(x,T) = 1.24/\lambda_{co}$ (eV). Table 3.1 shows an example of the Cd compositions used to achieve the target cutoff wavelength over a range of temperatures. Table 3.2 lists the specific simulation parameters for MWIR and LWIR *p*-*n* homojunction and DLPH structures.

The R_0A products obtained from the 1-D numerical model were compared to experimental data and an analytical model developed based on experimental data

Cd composition x for λ_{co} at varying T					
λ_{co} (μm)	E_g (eV)	77 K	180 K	200 K	300 K
5	0.2480	0.3031	0.2884	0.2850	0.268
6	0.2060	0.2771	0.2604	0.2570	0.2379
7	0.1770	0.2586	0.2406	0.2365	0.2163
8	0.1550	0.2447	0.2259	0.2215	0.2002
9	0.1370	0.2340	0.2144	0.2102	0.1879
10	0.1240	0.2254	0.2052	0.2010	0.1780
11	0.1120	0.2184	0.1978	0.1935	0.1700
12	0.1030	0.2126	0.1916	0.1872	0.1633

Table 3.1: Example of Cd composition x values used corresponding to cutoff wavelength λ_{co} and material bandgap E_g for varying temperatures.

MWIR p-n homojunction and DLPH Parameters (λ_{co} = 5 μm)						
Layer	Thickness	Cd composition	Doping	E_{trap}	SRH lifetime	F_1F_2
Top	$t_1 = 1\ \mu$m	$x_1 = x_2$ (DLPH: + 0.1)	$N_A = 5\times10^{17}$ cm^{-3}	$0.25E_g$	$\tau_{n0} = 10\ \mu$s	0.3
Absorber	$t_2 = 5\ \mu$m	x_2 = varied for λ_c	$N_D = 8\times10^{14}$ cm^{-3}		$\tau_{p0} = 1\ \mu$s	

LWIR p-n homojunction and DLPH Parameters (λ_{co} = 12 μm)						
Layer	Thickness	Cd composition	Doping	E_{trap}	SRH lifetime	F_1F_2
Top	$t_1 = 1\ \mu$m	$x_1 = x_2$ (DLPH: + 0.1)	$N_A = 5\times10^{17}$ cm^{-3}	$0.25E_g$	$\tau_{n0} = 10\ \mu$s	0.3
Absorber	$t_2 = 10\ \mu$m	x_2 = varied for λ_c	$N_D = 8\times10^{14}$ cm^{-3}		$\tau_{p0} = 1\ \mu$s	

Table 3.2: Simulation parameters of MWIR and LWIR p-n homojunction and DLPH photodiodes.

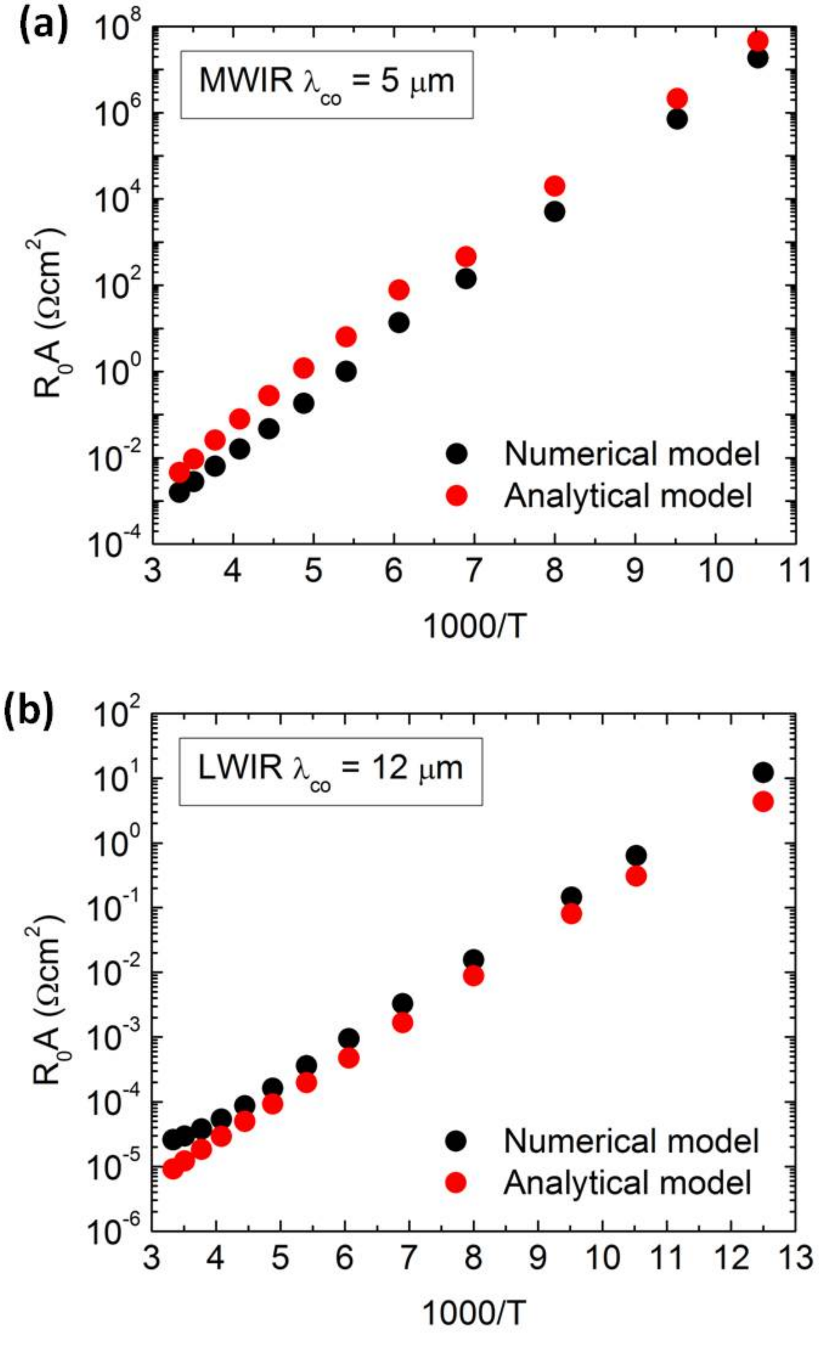

Figure 3.3: Comparison of R_0A obtained from the numerical model using parameters in Table 3.2 and an analytical model based on experimental data Ref. [64] for a *p*-*n* homojunction structure as a function of temperature.

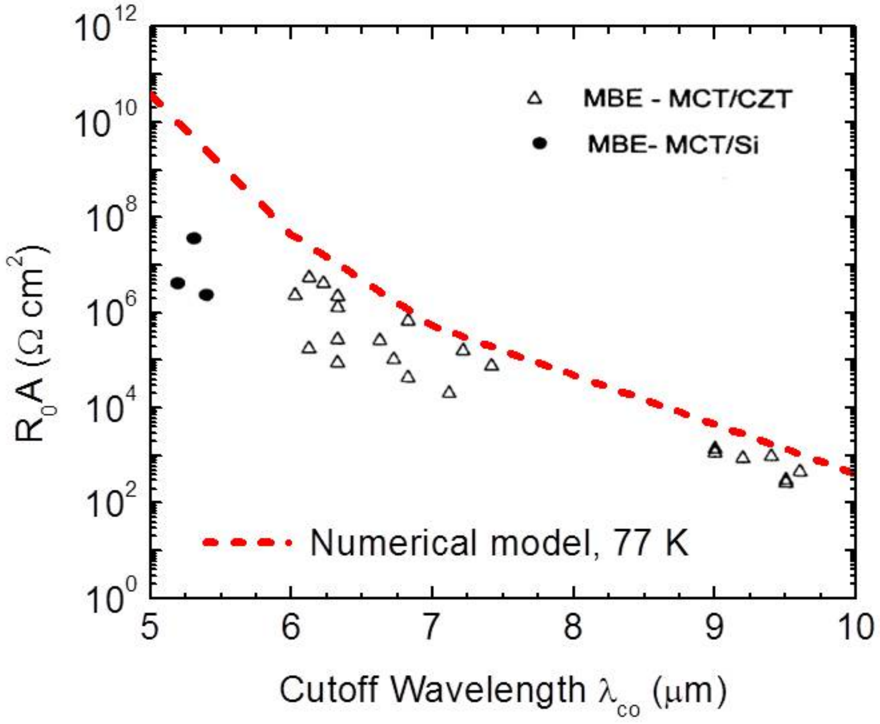

Figure 3.4: Comparison of numerical DLPH model results to median R_0A products at 77 K as a function of cutoff wavelength (MWIR to LWIR) for *p*-*n* HgCdTe DLPH structures grown on CdZnTe and on Cd/Si substrates by MBE [15].

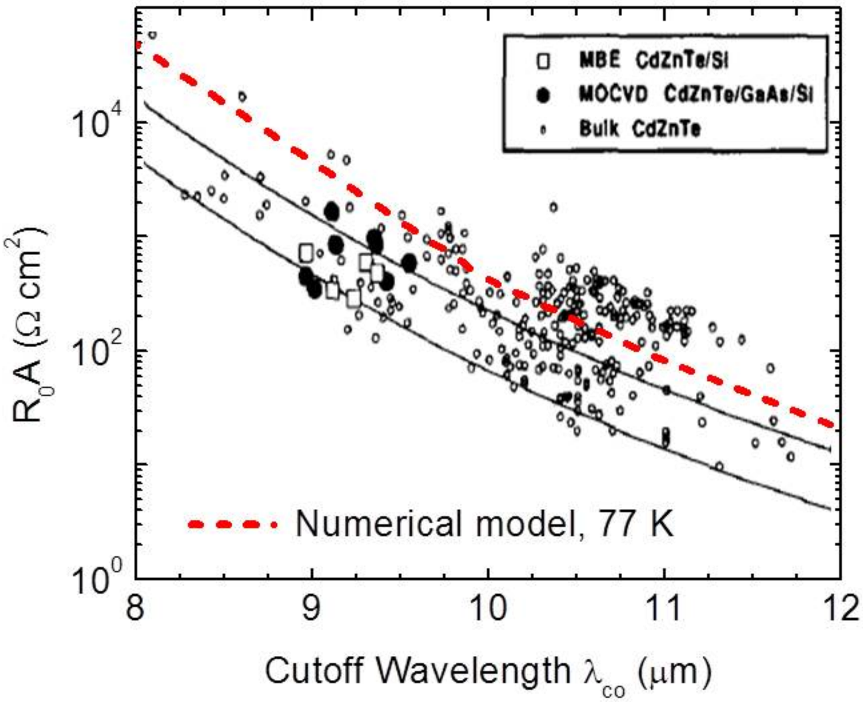

Figure 3.5: Comparison of numerical DLPH model results to 78 K R_0A values as a function of cutoff wavelength for LWIR HgCdTe DLHJ stuctures grown on varying substrates using different techniques. [14].

[64, 67]. Figure 3.3 illustrates the numerically calculated R_0A product as a function of temperature for MWIR and LWIR *p*-*n* homojunction diodes. The values closely agree with those obtained using an empirically-based analytical model [64], confirming the numerical model follows the expected trends described by conventional HgCdTe *p*-*n* homojunction devices. Further comparisons of numerical R_0A values for MWIR and LWIR DLPH devices (Figures 3.4 and 3.5) also show good agreement with experimental data for HgCdTe DLPH detectors [14, 15].

3.5 Summary

A 1-D numerical device model was created in the commercial software package Sentaurus Device as a tool to simulate device behavior and performance characteristics of the alternative detectors which are examined in subsequent chapters. To provide an accurate representation, HgCdTe material properties described in Chapter II were incorporated in the model with specific structural parameters defined for each layer within a device. The device model was validated by comparing calculated values to published experimental data on standard HgCdTe DLPH devices.

CHAPTER IV

Predicted Performance Advantages of Auger-Suppressed HOT Devices

4.1 Background and Motivation

The dark current and noise current that determine the required operating temperature for high performance IR HgCdTe detectors are limited by the generation of free carriers by Auger processes, and reducing the cooling requirements of infrared photon detection systems without sacrificing performance is a non-trivial objective.

Device structures with combinations of exclusion (P^+/π or N^+/ν) and extraction (P^+/ν or N^+/π) junctions in $P^+/\nu/N^+$ and $P^+/\pi/N^+$ configurations have demonstrated suppression of Auger mechanisms by reducing the absorber carrier density below thermal equilibrium in reverse bias [30]. The dark current in these HOT structures has been shown to be lower than that achieved by standard *p*-*n* junction photodiodes [62, 63, 68] and exhibits higher performance for a given operating temperature. A comprehensive assessment of the behavior and performance improvements of the proposed Auger-suppressed HgCdTe infrared photodiodes ($P^+/\nu/N^+$ structure) compared with the equivalent state-of-the-art HgCdTe infrared DLPH devices (P^+/ν structure) is presented in this chapter. Past studies employing similar analytical and numerical methods [55, 64, 66, 68, 69] have examined the electrical

MWIR DLPH Parameters (λ_{co} = 5 μm)						
Layer	Thickness	Cd composition	Doping	E_{trap}	SRH lifetime	F_1F_2
Top	t_{top} = 1 μm	$x_{top} = x_{abs} + 0.1$	N_A = 5×10^{17} cm^{-3}	0.25E_g	τ_{n0} = 10 μs	0.3
Absorber	t_{abs} = 5 μm	x_{abs} = varied for λ_c	N_D = 8×10^{14} cm^{-3}		τ_{p0} = 1 μs	

MWIR HOT Parameters (λ_{co} = 5 μm)						
Layer	Thickness	Cd composition	Doping	E_{trap}	SRH lifetime	F_1F_2
Top	t_{top} = 1 μm	$x_{top} = x_{abs} + 0.1$	N_A = 5×10^{17} cm^{-3}	0.25E_g	τ_{n0} = 10 μs	0.3
Absorber	t_{abs} = 3 μm	x_{abs} = varied for λ_c	N_D = 8×10^{14} cm^{-3}		τ_{p0} = 1 μs	
Bottom	t_{bot} = 1 μm	$x_{bot} = x_{abs} + 0.1$	N_D = 5×10^{17} cm^{-3}			

Table 4.1: MWIR DLPH and HOT device simulation parameters.

LWIR DLPH Parameters (λ_{co} = 12 μm)						
Layer	Thickness	Cd composition	Doping	E_{trap}	SRH lifetime	F_1F_2
Top	t_{top} = 1 μm	$x_{top} = x_{abs} + 0.1$	N_A = 5×10^{17} cm^{-3}	0.25E_g	τ_{n0} = 10 μs	0.3
Absorber	t_{abs} = 10 μm	x_{abs} = varied for λ_c	N_D = 8×10^{14} cm^{-3}		τ_{p0} = 1 μs	

LWIR HOT Parameters (λ_{co} = 12 μm)						
Layer	Thickness	Cd composition	Doping	E_{trap}	SRH lifetime	F_1F_2
Top	t_{top} = 1 μm	$x_{top} = x_{abs} + 0.1$	N_A = 5×10^{17} cm^{-3}	0.25E_g	τ_{n0} = 10 μs	0.3
Absorber	t_{abs} = 3 μm	x_{abs} = varied for λ_c	N_D = 8×10^{14} cm^{-3}		τ_{p0} = 1 μs	
Bottom	t_{bot} = 1 μm	$x_{bot} = x_{abs} + 0.1$	N_D = 5×10^{17} cm^{-3}			

Table 4.2: LWIR DLPH and HOT device simulation parameters.

characteristics of various multi-layer HgCdTe detectors; however, study of the differences and performance advantages of Auger-suppressed photodiodes over conventional *p*-*n* devices has not been reported. In this chapter, detector behavior is calculated for MWIR and LWIR DLPH and HOT detectors, and an analysis of predicted improvements in required operating temperatures is discussed.The premise of this study is to demonstrate temperature-dependent trends in the behavior of HOT versus DLPH structures, and the focus remains on the overall outcome of these comparative device calculations.

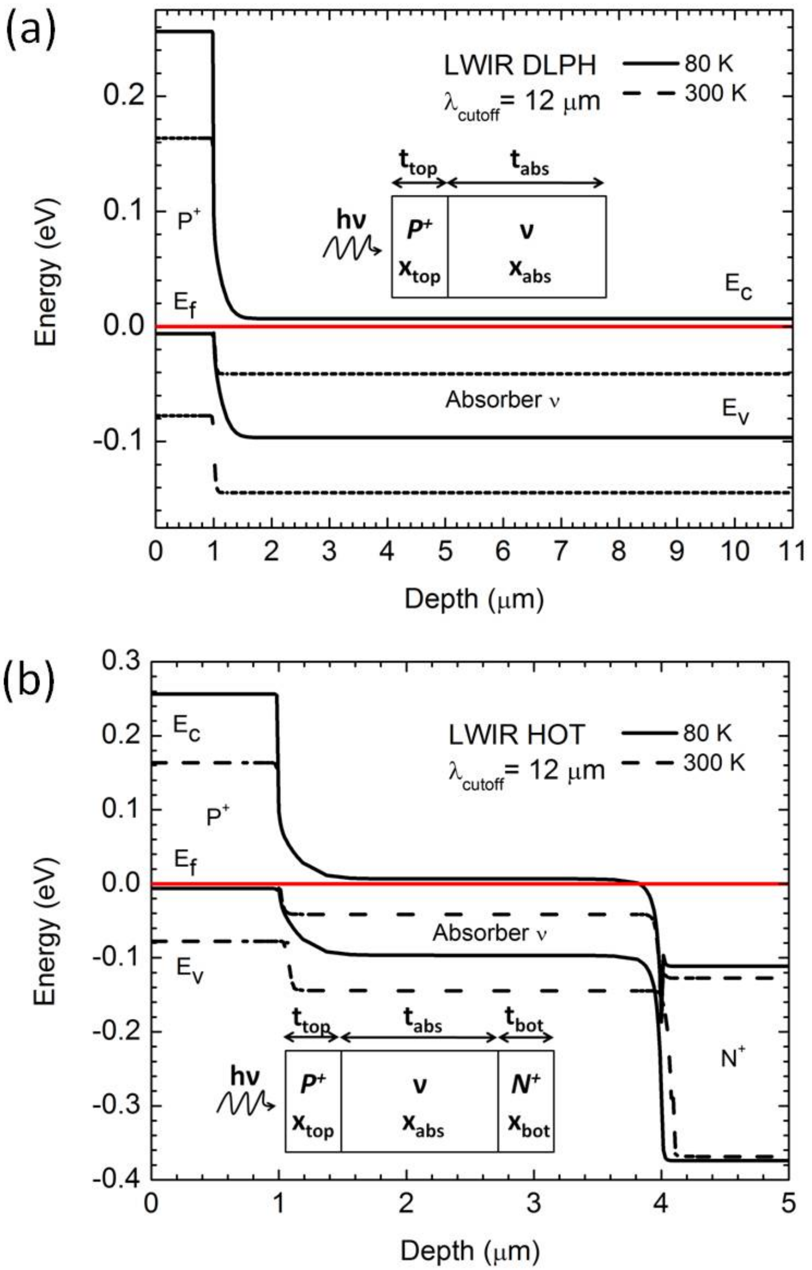

Figure 4.1: Energy band diagram at equilibrium for LWIR (a) DLPH and (b) HOT structures at 80 K and 300 K. Basic device structures as insets.

4.2 Modeling the HgCdTe HOT Detector

The conventional p-n DLPH structure shown in the inset of Figure 4.1 consists of two layers, a highly doped, wide bandgap P^+ cap layer in contact with a lightly doped, narrow bandgap ν absorber region. The HOT device comprises three layers: two highly doped, wide bandgap P^+ and N^+ layers contacting a lightly doped, narrow bandgap ν middle layer as illustrated in the inset of Figure 4.1b. Tables 4.1 and 4.2 list specific simulation parameters for the MWIR and LWIR DLPH and HOT devices.

Detectivity calculations were first performed with 300 K background scene temperature and accounted for a 20° field-of-view ($f_\sharp$=2.835), and later with $T_s = T_d$, where the scene matched the device temperature. The $P^+/\nu/N^+$ structure was chosen in this study due to the relative ease in achieving controllable lightly doped n-type absorber regions using techniques such as molecular beam epitaxy, whereas controllable low p-type doping with a low density of Shockley–Read–Hall centers is still a technological challenge. The absorber layer thicknesses for the DLPH and HOT structures were chosen according to previous simulations performed for devices in similar MWIR and LWIR spectral response windows to optimize the benefits and trade-offs of Auger suppression and optical absorption [68]. Detector speed was not a significant consideration, as HgCdTe detectors are typically limited by carrier speeds, generally operating in the MHz, while FPA systems run at much lower frame rates.

4.3 Results and Discussion

4.3.1 J_{dark} Characteristics and R_0A Product

Representative calculated energy band diagrams for both LWIR DLPH and HOT structures at equilibrium are plotted in Figure 4.1 for temperatures of 80 K and 300 K. Representative current-voltage characteristics calculated for both MWIR device structures at three temperatures between 125 K and 300 K are shown in Figure 4.2.

Similarly, representative current-voltage characteristics calculated for both LWIR device structures at three temperatures between 105 K and 205 K are d illustrate in Figure 4.3.

The dark current density in the MWIR HOT structure is approximately between one and two orders of magnitude lower than that observed in the DLPH structure for all temperatures. In the LWIR HOT structure, J_{dark} exhibits approximately a one order of magnitude reduction compared to the DLPH device for temperatures up to 205 K. The reduction in dark current density in both MWIR and LWIR HOT structures is due to the Auger suppression mechanism initiated by the exclusion and extraction junctions. Under reverse bias, the minority holes are removed from the absorber region through the P^{+}/ν extraction junction. With increasing reverse bias, the holes are extracted from the absorber region more rapidly than they can be replenished from the N^{+} layer through the exclusion junction. Thus, the hole concentration decreases significantly below its thermal equilibrium value. In order to maintain charge neutrality in the absorber, the electron concentration is also reduced below equilibrium. The overall decrease in the intrinsic carrier concentration then reduces the Auger recombination rate in the active region. A clear negative differential resistance (NDR) is observed in the I-V characteristics of both MWIR and LWIR HOT structures as the result of the Auger suppression mechanism. This behavior becomes more prominent as temperatures increase, but is apparent at lower temperatures for the LWIR devices where Auger processes are stronger in the narrow bandgap material. In HOT devices, the operating bias is selected corresponding to a region on the I-V curve where Auger process are suppressed.

The calculated dark current density at 300 mV reverse bias as a function of temperature is given for both MWIR and LWIR device structures in Figure 4.4a. The dark current values are shown for constant cutoff wavelengths of 5 μm (MWIR) and 12 μm (LWIR), to allow direct comparisons of detector performance at varying tem-

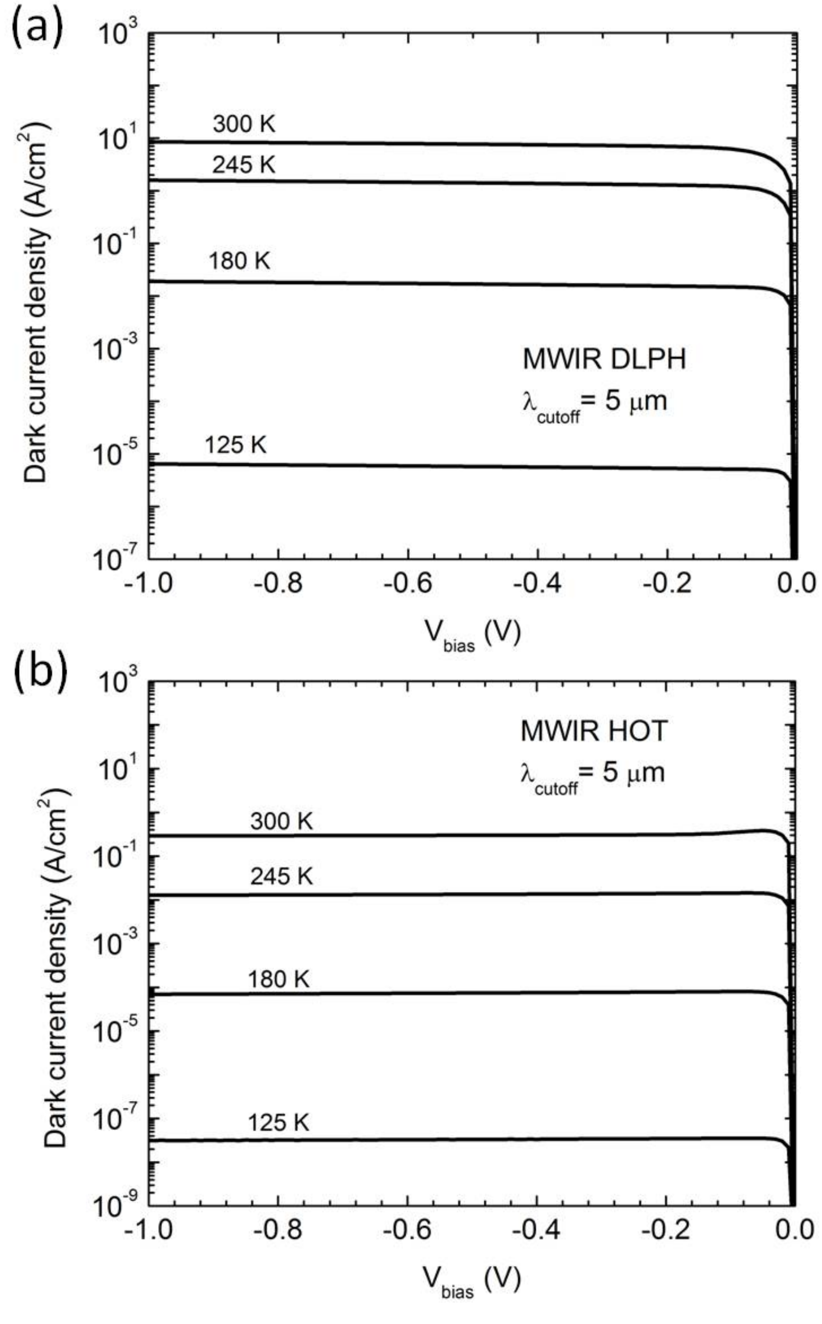

Figure 4.2: Calculated current-voltage characteristics for MWIR (a) DLPH and (b) HOT structures at various temperatures.

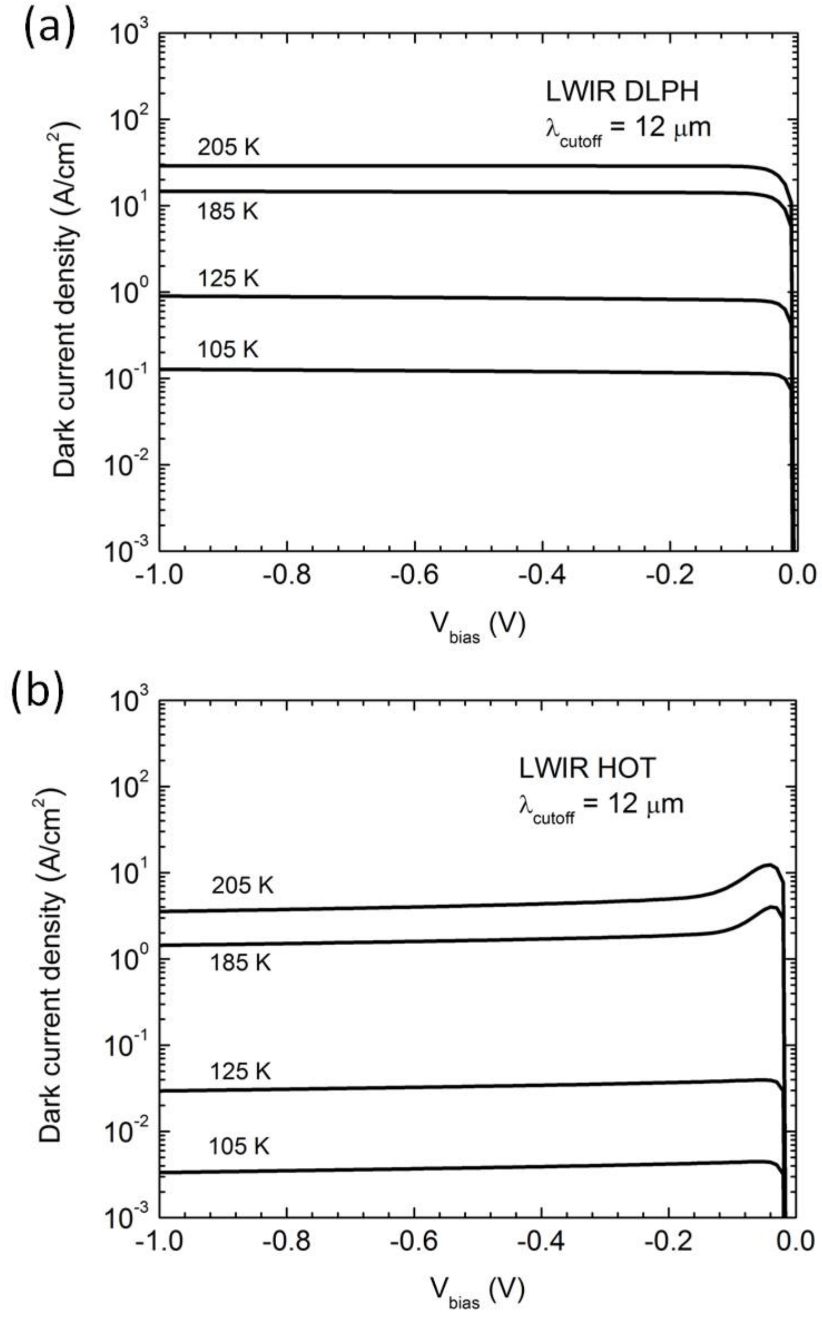

Figure 4.3: Calculated current-voltage characteristics for LWIR (a) DLPH and (b) HOT structures at various temperatures.

peratures. The cutoff wavelength was fixed at each temperature by adjusting the Cd fraction x in the absorber layer of the device. At all temperatures, the HOT structure exhibits equal or lower dark current density than the DLPH device due to Auger suppression. In Figure 4.4a, there is a significant reduction in dark current density for the MWIR and LWIR HOT devices at low temperatures where the dark current is limited predominantly by SRH processes.

At higher temperatures, all devices become diffusion limited. The dark current in the MWIR devices still exhibits strong, competing effects of SRH generation, and Auger suppression results in a large current decrease in the HOT device. In contrast, LWIR devices are limited by Auger generation for a wider temperature range, where the dark current density in the HOT device demonstrates an order of magnitude reduction in comparison with the DLPH structure. At temperatures above 165 K, LWIR devices begin to exhibit a convergence of dark current values corresponding to the diffusion current which overwhelms the effect of the Auger suppression provided by the HOT structure.

As discussed in Chapter I, R_0A values provide an important metric for standard p-n junction photodetectors. However, Auger suppression in HOT devices is bias dependent; in this case, the operating current in reverse bias is not accurately reflected by R_0A. Alternatively, a comparison to standard p-n junction photodetectors can be inferred using an equivalent R_0A based on the dark current in the Auger-suppressed region using the relation $R_0A = \frac{k_B T_d}{q} J_{dark}(V_{bias})$. R_0A values for DLPH, HOT, and p-n junction [70] structures operating at 300 mV reverse bias are compared in Figure 4.4b, where an expected increase in the equivalent R_0A values is observed for the HOT device corresponding to the Auger suppression.

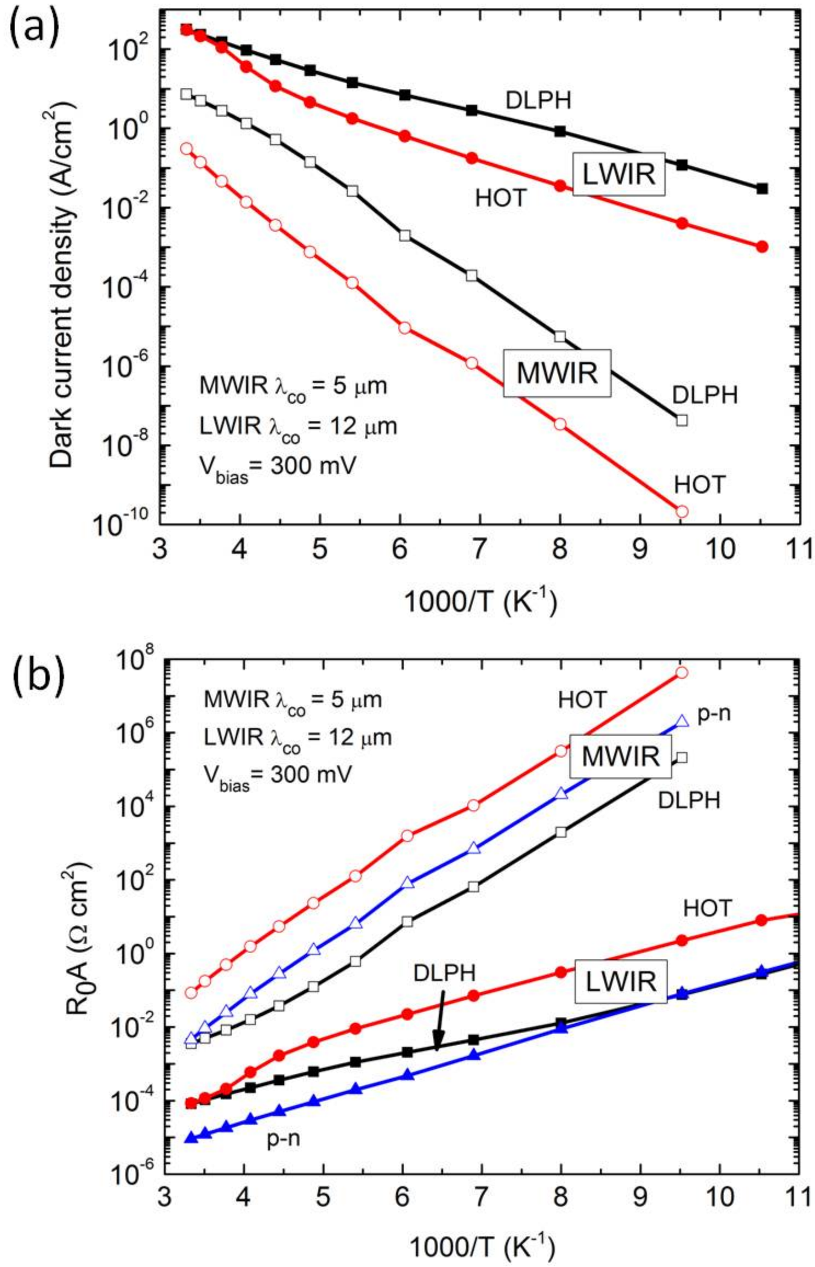

Figure 4.4: Calculated (a) dark current density and (b) equivalent R_0A as a function of temperature for MWIR and LWIR DLPH and HOT devices.

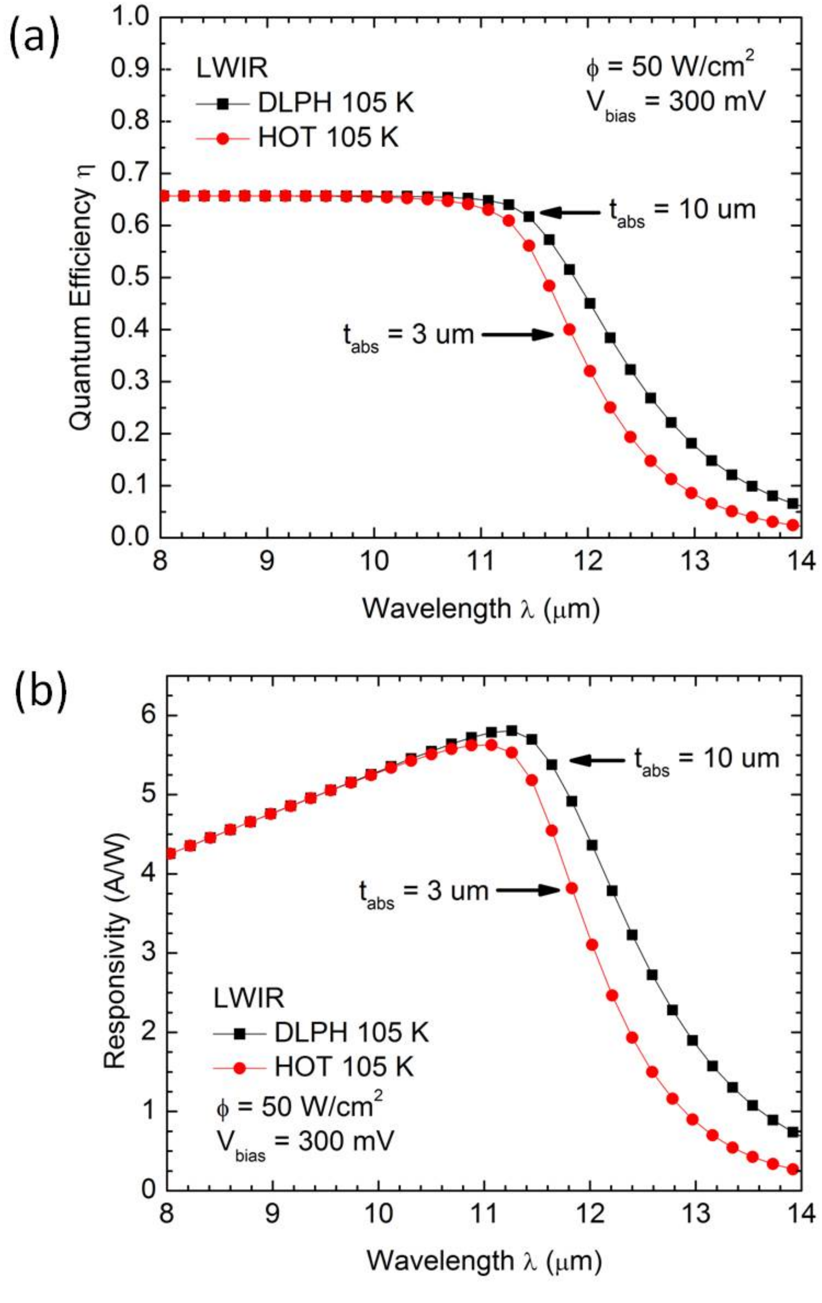

Figure 4.5: Calculated (a) quantum efficiency and (b) responsivity as a function of incident wavelength for DLPH and HOT structures.

4.3.2 Spectral Response

The simulated quantum efficiency and responsivity for DLPH and HOT LWIR devices at a given temperature are shown in Figure 4.5. The calculated values are similar for both structures at shorter incident wavelengths, with the HOT device exhibiting slightly higher quantum efficiency and responsivity than DLPH; this may be attributed to increased minority carrier diffusion lengths and a corresponding improvement in the collection of photogenerated carriers for the HOT device. Near the band-edge, the DLPH device, exhibits higher quantum efficiency and responsivity due to increased IR absorption in the thicker material structure.

4.3.3 Peak D^* and BLIP Operation

Figure 4.6a shows the peak detectivity D^* (T_s=T_d) of the MWIR and LWIR structures as a function detector temperature. Similar to the dark current calculations, the absorber Cd fraction was adjusted at each temperature to maintain a constant cutoff wavelength. The BLIP D^* values for a 300 K scene were obtained by examining the saturation detectivity for HOT and DLPH structures. In the MWIR devices, the D^* for a 300 K scene saturates at temperatures below ∼155 K, where the detector noise current in both structures is limited by the background scene. Above ∼155 K, the generation rate of thermally induced intrinsic carriers begins to increase, and the detector noise current in both devices becomes diffusion limited. The detectivity, therefore, begins to decrease with increasing T_d, and the temperature dependent dark current dominates the background induced noise. At elevated temperatures, the HOT device exhibits higher detectivity than the DLPH structure as a result of the lower, Auger-suppressed dark current. The temperatures for BLIP (300 K scene) operation in the MWIR HOT and DLPH structures in Figure 4.6 are 203 K and 155 K, respectively. The MWIR HOT device continues to exhibit detectivities higher than those achieved by the MWIR DLPH structure for temperatures above 155 K. The

LWIR HOT device structure exhibits a significant improvement in detectivity over the LWIR DLPH device structure, where BLIP (300 K scene) performance is achieved for temperatures below 145 K and 102 K for the HOT and DLPH structures, respectively. The D^* values for the LWIR HOT device structure maintains an improvement over the DLPH device structure for $T_d < 145$ K due to the Auger suppression. However, the improvement in the HOT device is reduced for $T_d > 145$ K due to increased intrinsic thermal generation. It should be noted that the conditions where significant thermal generation mitigates the improvements of Auger suppression is far above the temperature required to achieve 300 K BLIP operation.

To further analyze the influence of Auger suppression for a wider range of cutoff wavelengths, the maximum BLIP temperatures T_{BLIP} (300 K scene) and their differences ΔT_{BLIP} for DLPH and HOT devices are calculated for varying cutoff wavelengths and summarized in Figure 4.7. T_{BLIP} decreases for both structures with increasing cutoff wavelengths and corresponds to the reduction in the absorber bandgap which facilitates the generation of carriers, contributing to the increase in dark current density. The HOT BLIP temperatures are consistently higher over the range of cutoff wavelengths due to the Auger suppression mechanism which minimizes the dark current, increasing the T_{BLIP} achieved by the device. Furthermore, a large difference of ΔT_{BLIP} ranging from 43 K - 50 K is achieved over these cutoff wavelengths, marking significant improvement in cooling requirements for the HOT structure over the conventional DLPH device. Contrary to initial expectations, the ΔT_{BLIP} values do not increase with longer cutoff wavelengths. This behavior may be attributed to the physical limitations of Auger suppression in the partially depleted absorber region.

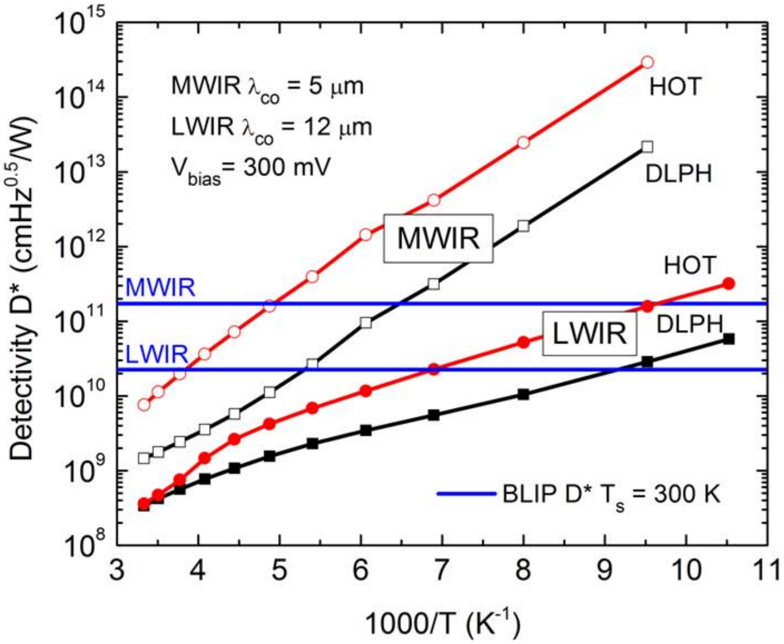

Figure 4.6: (a) Calculated detectivity values for MWIR and LWIR DLPH and HOT devices.

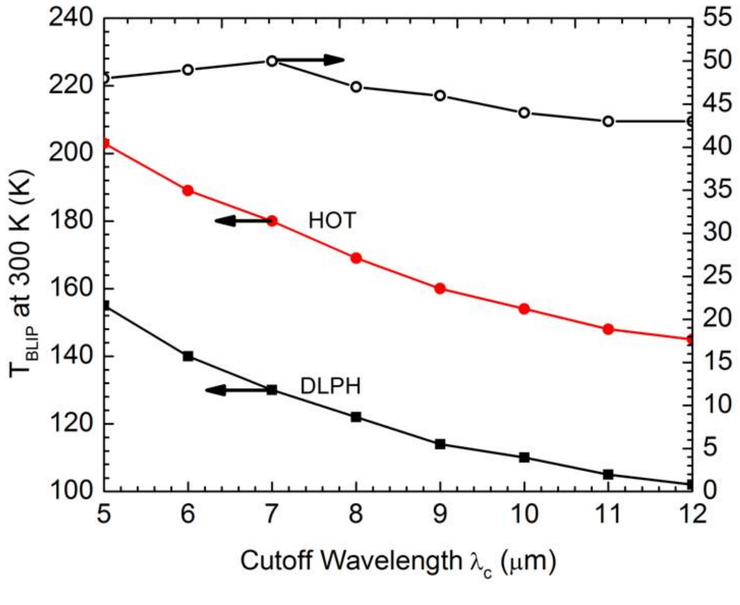

Figure 4.7: Calculated 300 K BLIP performance temperatures and difference in maximum BLIP temperature for varying cutoff wavelengths for DLPH and HOT devices. DLPH and HOT absorber widths are 5 μm and 3 μm, respectively, and devices are biased at 300 mV.

4.4 Conclusion

The electrical behavior and performance characteristics of the Auger-suppressed HOT HgCdTe photodiode and the conventional DLPH detector were analyzed using numerical and analytical models. DLPH and HOT devices were examined in MWIR and LWIR windows, and device metrics were compared as a function of operating temperature. Quantitative simulations show that the improvements of HgCdTe HOT technology are strongly dependent on the complex relationship of a number of competing parameters such as temperature dependent generation mechanisms, cutoff wavelength, and the absorber bandgap. Overall, both MWIR and LWIR HOT devices exhibit approximately one to two orders of magnitude increase in D^* with a general square root dependency on noise current in comparison to DLPH devices operating at the same temperature. The calculated D^* values of the MWIR HOT device show that BLIP operation can be achieved at $\sim$203 K compared with $\sim$155 K of the DLPH detector operating with T_s =300 K. Similarly, LWIR devices achieve BLIP conditions at $\sim$145 K and $\sim$102 K for HOT and DLPH structures, respectively, for a similar scene temperature. The calculated results for the Auger-suppressed photodiode predict a significant advantage over the leading DLPH technology with increased operating temperatures between $\sim$40-50 K for a wide range of cutoff wavelengths.

CHAPTER V

Arsenic Diffusion Study in HgCdTe for Low p-type Doping in Auger-Suppressed Photodiodes

5.1 Background and Motivation

As discussed in the previous chapter, increasing the operating temperature of infrared photon detection systems without sacrificing performance is an important aspect of recent photodetector research. At high temperatures, the carrier density in the lightly doped absorber region of HgCdTe detectors increases due to thermally generated intrinsic carriers and the dark current becomes dominated by Auger generation and recombination processes. As described in Section 4.1, HOT device structures with layers in $P^+/\nu/N^+$ and $P^+/\pi/N^+$ configurations (combinations of exclusion and extraction junctions under reverse bias) have demonstrated suppression of Auger mechanisms by reducing the absorber carrier density below thermal equilibrium in reverse bias [30].

To maximize the benefits of the $P^+/(\nu \text{ or } \pi)/N^+$ design, it is important to achieve effective control of the doping concentration and distribution within the absorber region [68]. Past studies have reported reduced Auger processes in p-doped HgCdTe compared with n-doped HgCdTe due to the difference in Auger 1 and Auger 7 carrier lifetimes [71, 72]. An example of J_{dark} values calculated using a numerical model for equivalent HOT structures with different absorber doping in Figure 5.1 illustrates the effects of p-type versus n-type doping on Auger suppression as a function of material quality reflected by SRH minority carrier lifetimes (τ_{SRH}). Therefore, it is preferred to fabricate devices with the $p^+/\pi/N^+$ arrangement. In-situ As doping of HgCdTe has been demonstrated by MBE [26–29]; however, controllable p-type doping at low concentrations with long minority carrier lifetimes has been difficult to achieve. In this study, another approach is taken by implementing implantation and deep diffusion techniques to achieve controllable low p-type doping. Previous work has demonstrated a novel technique designed to achieve deep diffusion of As as a p-type dopant [25] by annealing ion-implanted HgCdTe at a low substrate temperature and under low Hg partial pressure. These methods have resulted in low As dopant levels in the absorber layer ranging from 10^{15} cm^{-3} to 10^{16} cm^{-3}. The main objective of this work is to obtain a low p-type doping concentration and a P^+/π step structure by combining shallow As implantation with deep diffusion under low Hg pressure. In this study, As diffusion is studied in HgCdTe under low Hg pressure to determine resulting dopant depth profiles. Diffusion coefficients are extracted from dopant profiles and compared to previous reports with the goal of achieving an optimized process for good control of arsenic diffusion and P^+/π step profiles for detector devices exhibiting Auger suppression.

5.2 Experiment Methodology

$Hg_{1-x}Cd_xTe$ samples were grown by MBE at EPIR Technologies, Inc. using a Riber 32 MBE machine. The samples were grown with absorber alloy compositions of $x \approx 0.20$ and $x \approx 0.30$ corresponding to LWIR and MWIR detection, respectively. The absorber layer is contacted by wider bandgap layers on the top and bottom sides. The full layer structure of an MWIR sample is shown in Figure 5.2. The samples were grown with intentional n-type indium doping to provide a controlled

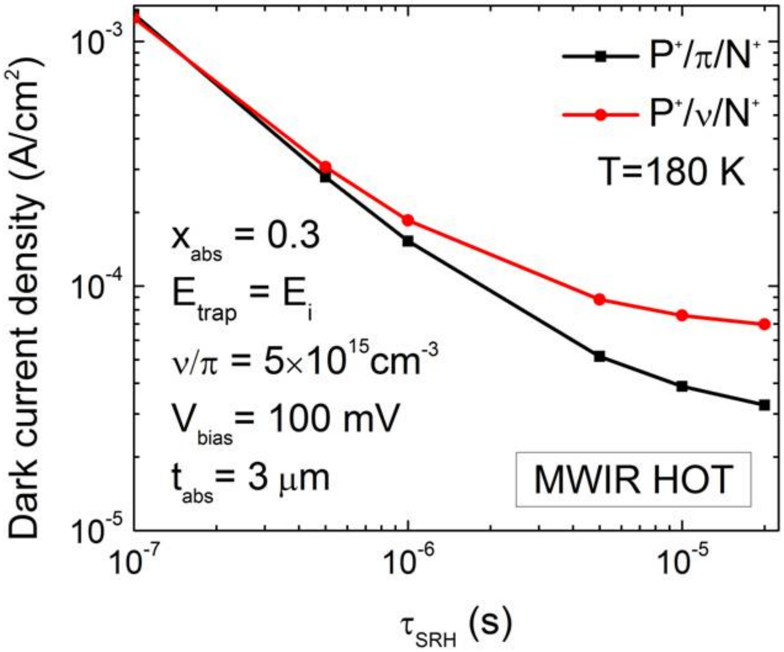

Figure 5.1: Calculated dark current density values for equivalent MWIR HOT devices with *p*-type and *n*-type absorber as a function of material quality (τ_{SRH}).

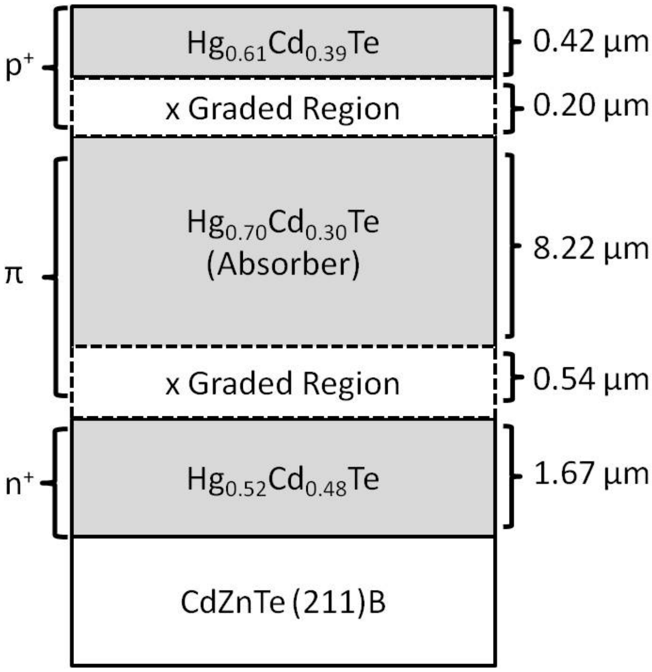

Figure 5.2: Layer structure of MBE grown $Hg_{1-x}Cd_xTe$ MWIR samples.

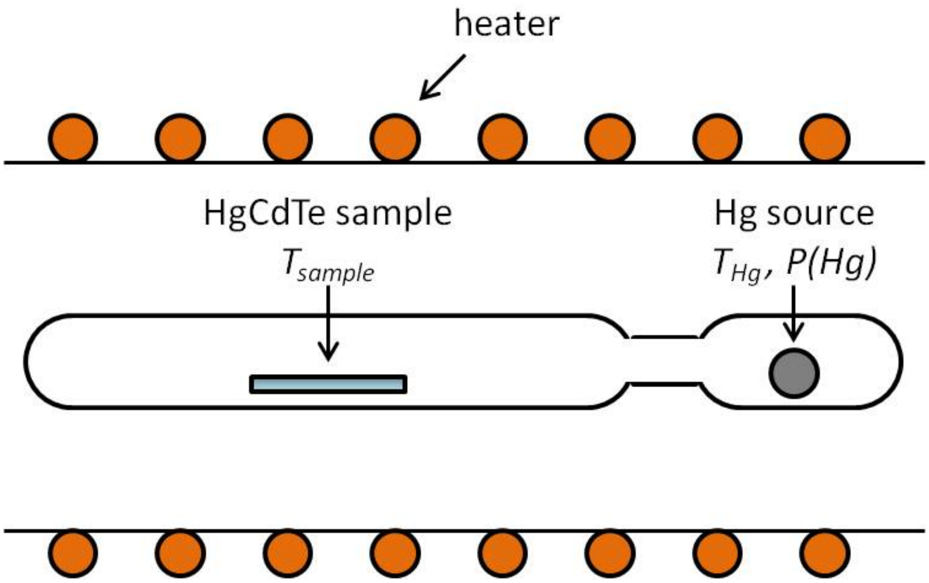

Figure 5.3: Schematic of sealed quartz ampoule separating HgCdTe sample and Hg source in two-zone annealing furnace.

baseline n-type concentration of $\sim 10^{15}$ cm^{-3}. The LWIR samples were implanted with an As dose of 5×10^{13} cm^{-2} and a beam energy of 200 keV, while the MWIR samples were implanted with a dose of 5×10^{12} cm^{-2} at 350 keV. The implantation and energy values were chosen to correspond to past internal diffusion experiments using similar conditions. The low diffusivity in HgCdTe due to the large group V atom size and shallow activation energy make As a primary choice for p-type doping due to its controllability of junction formation as described in Chapter II. Here, it is noted that the differences in the implantation conditions between the LWIR and MWIR samples were due to the limited availability of MBE grown HgCdTe samples with comparable SIMS data. However, the focus of this study is to emphasize the relative changes in the As diffusion coefficients and diffusion depths across different experiments within the respective spectral response range.

The samples were annealed under Hg overpressure using a three-step annealing process as follows: 1) deep diffusion, 2) activation, and 3) Hg vacancy annihilation. To obtain deep diffusion of arsenic as initially demonstrated by Wijewarnasuriya et

LWIR HgCdTe (x $\approx$ 0.2) Sample Conditions		
Implant Condition	$5\times10^{13}\text{cm}^{-2}$; 200 keV	
Diffusion Anneal	LWIR 1	LWIR 2
T_{Hg}/T_{sample} (Duration)	240°C/300°C (16 h)	300°C/300°C (20.5 h)
$P(Hg)$	0.07 atm	0.32 atm
Activation Anneal T_{Hg}/T_{sample} (Duration)	440°C/450°C (15 min)	
Vacancy Anneal T_{Hg}/T_{sample} (Duration)	240°C/250°C (20 h)	

Table 5.1: Experimental conditions for deep diffusion anneals of MBE grown LWIR samples.

al. [25], several experiments were performed on the LWIR and MWIR samples with varying deep diffusion annealing parameters. The main parameters of variation are the anneal duration and Hg source temperature and corresponding Hg partial pressure $P(Hg)$. All samples were held at 300°C during the deep diffusion anneal. For each condition, the samples were sealed in a quartz ampoule and placed into a two-zone annealing furnace as shown in Figure 5.3, separating the samples from the Hg source. The partial pressure of Hg was controlled by the Hg source temperature (T_{Hg}), and the corresponding pressure values were determined from a look-up table [73]. The Hg source temperature was set to less than or equal to the sample temperature (T_{sample}) to prevent condensation of Hg droplets on the sample surface. Tables 5.1 and 5.2 describe the experimental parameter set-up for annealing conditions for both LWIR and MWIR samples.

Activation and vacancy annihilation anneals were carried out at 450°C for 15 minutes and at 250°C for 20 hours, respectively. A 10°C difference between the sample and Hg source was maintained to prevent Hg droplet condensation during the post-diffusion anneals and quenching. The As diffusion profiles in the HgCdTe layers were measured by secondary ion mass spectroscopy (SIMS) at Evans Analytical Group. As diffusion coefficients $D(As)$ were then extracted from the profiles using a dopant distribution model proposed by Nash et al. [74],

MWIR HgCdTe (x ≈ 0.3) Sample Conditions					
Implant Condition	5×10^{12}cm^{-2}; 350 keV				
Diffusion Anneal	MWIR 1	MWIR 2	MWIR 3	MWIR 4	MWIR 5
T_{Hg}/T_{sample}	240°C/300°C	270°C/300°C			300°C/300°C
Duration	20 h	12 h	16 h	20 h	12
$P(Hg)$	0.0639 atm	0.139 atm			0.277 atm
Activation Anneal T_{Hg}/T_{sample} (Duration)	440°C/450°C (15 min)				
Vacancy Anneal T_{Hg}/T_{sample} (Duration)	240°C/250°C (20 h)				

Table 5.2: Experimental conditions for deep diffusion anneals of MBE grown MWIR samples.

$$C_{As}(d,t) = \frac{Q}{\sqrt{2\pi}\sqrt{2D(As)t+\sigma^2)}}exp^{-\frac{(d-R)^2}{(2\sigma^2+4D(As)t)}} \tag{5.1}$$

where d is the depth from the sample surface, t is the annealing duration, Q is the implant dose, and R and σ are the fitting parameters for peak depth and standard deviation, respectively. Due to limited resources, SIMS measurements were not performed on the original implanted samples for the current experiments. However, an approximate fit was determined from past samples as-implanted with As under similar conditions as those described in this report. The Gaussian fitting was performed by considering only data points above a threshold value 10% of the peak As concentration. The Gaussian distribution was fit over the depth range corresponding to the thickness of the wide bandgap P^+ cap layer. The fitting does not account for non-uniformities in the Hg vacancy concentration due to the Cd composition gradient at the P^+/π interface. The R and σ parameters were calculated from coefficients extrapolated from a parabolic fit to the Gaussian as-implanted profile, and $D(As)$ values were determined by fitting to within roughly 35% average error of the data. Linear fittings were also performed to approximate the As concentration in the narrow bandgap absorber region. SIMS data points below the detection limit of 5×10^{14} cm^{-3} were excluded from the fitting.

5.3 Results and Discussion

The SIMS profiles for LWIR materials annealed with varying Hg partial pressure are shown in Figure 5.4. Comparing the deep diffusion junction depths, deeper As diffusion is observed in the sample annealed under lower Hg pressure (0.07 atm). The P^+/π junction is defined by the interface at which the HgCdTe material changes from the wide bandgap cap layer to the narrow bandgap absorber region. Here, the deep diffusion junction is defined as the depth at which the Gaussian and linear fittings intersect. The data in Figure 5.4a exhibits a diffusion junction of 1.5 μm and an As doping concentration in the range of 10^{15}-10^{16} cm^{-3}. The cause of the unexpected increase in As concentration in the absorber region of Figure 5.4a is uncertain and may possibly be due to defects associated with the implantation process or as-grown defects. However, since the Gaussian distribution component of the diffusion process is of primary interest, these outlying data points are excluded from the linear fit. The data in Figure 5.4b exhibits a diffusion junction of 0.6 μm and an As doping level in the range of 10^{14}-10^{15} cm^{-3}. The As concentration in the absorber region is an order of magnitude lower for the sample annealed at a lower Hg pressure due to the increased diffusion of As atoms through a higher concentration of Hg vacancies. As diffusion coefficients of $D(As) = 6{\times}10^{-14}$ cm^2 s^{-1} (LWIR 1) and $D(As) = 2{\times}10^{-15}$ cm^2 s^{-1} (LWIR 2) were extracted for samples in Figure 5.4. It is noted that the samples were annealed at different $P(Hg)$ values and durations; however, the data makes a strong case that annealing at a lower Hg partial pressure even for a shorter time increases the effects of deep diffusion more significantly than annealing at higher $P(Hg)$. Similarly, Figure 5.5 compares MWIR samples annealed at different Hg partial pressure for 20 hours. Again, deeper diffusion is observed in the sample annealed at lower Hg partial pressure (MWIR 1; $P(Hg) = 0.0639$ atm). A deep diffusion junction of approximately 0.7 μm is observed in MWIR 1, while a junction depth of about 0.58 μm is observed for sample MWIR 4. The absorber As concentrations in samples MWIR 1 and MWIR

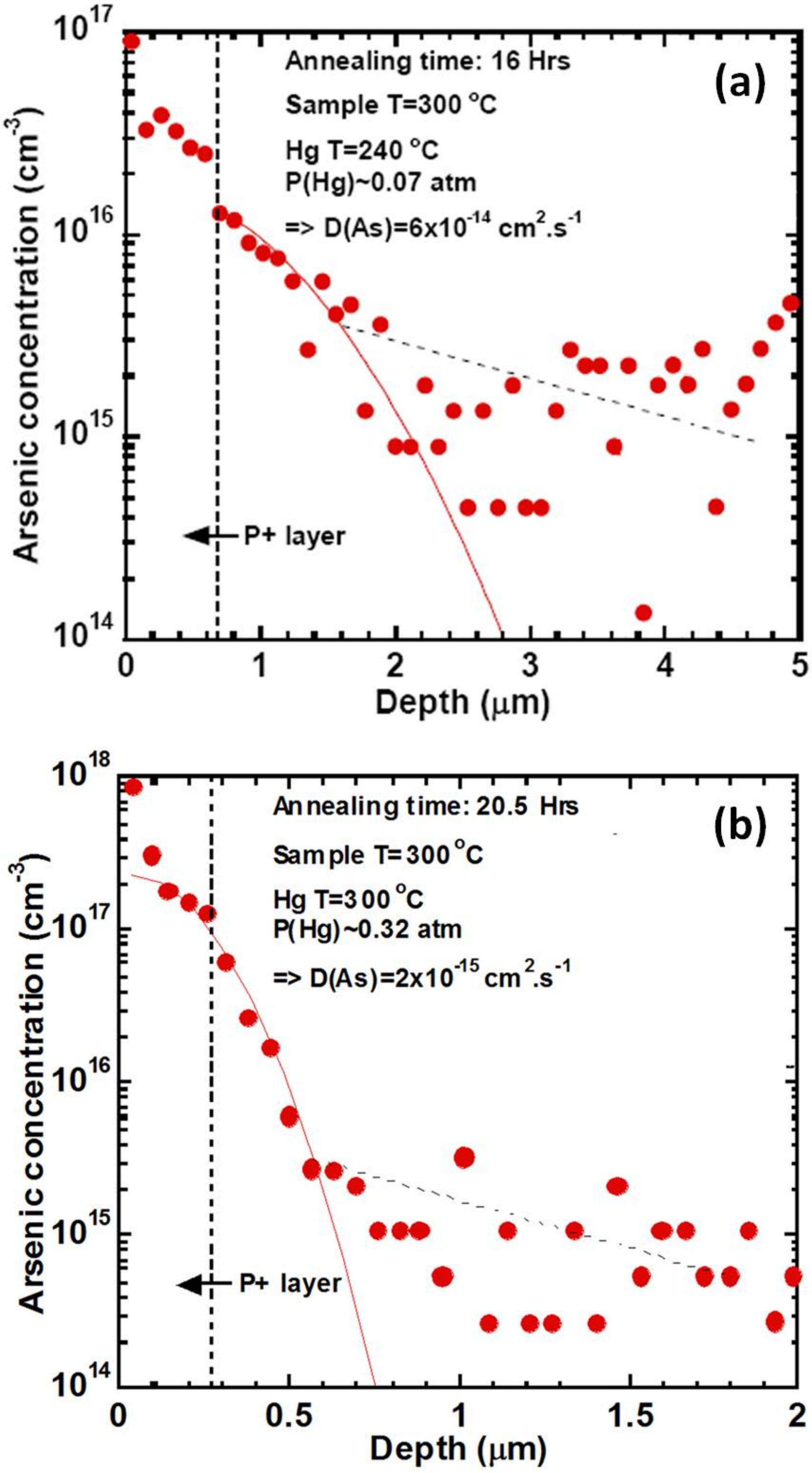

Figure 5.4: SIMS data of LWIR As diffusion profile for (a) LWIR 1 with 16 h anneal at $P(Hg) = 0.07$ atm and (b) LWIR 2 with 20.5 h anneal at $P(Hg) = 0.32$ atm.

4 are between 4.6×10^{14} cm^{-3}-1.69×10^{15} cm^{-3} (MWIR 1) and 3.64×10^{14}-1.7×10^{15} cm^{-3} (MWIR 4) with diffusion coefficients of $D(As) = 1.35\times10^{-15}\pm1.5\times10^{-16}$ cm^2 s^{-1} (MWIR 1) and $D(As) = 7.5\times10^{-16}\pm1.5\times10^{-16}$ cm^2 s^{-1} (MWIR4). The As concentration values in the absorber are not necessarily reflected in the figures because the range of the fit extends farther into the sample than indicated in these plots. The dependence of the extracted diffusion coefficients on Hg partial pressure is smaller than observed for the LWIR sample, but dependence is detected nonetheless.

The SIMS profiles of MWIR samples annealed for varying durations of 12 hours and 16 hours under the same Hg partial pressure of 0.139 atm are shown in Figure 5.6. Sample MWIR 2 has a diffusion junction depth of around 0.5 μm, an As doping level between 3.35×10^{14}-2×10^{15} cm^{-3}, and $D(As) = 7.5\times10^{-16}\pm1.5\times10^{-16}$ cm^2 s^{-1}; MWIR 3 has a diffusion junction of approximately 0.57 μm, an As doping concentration of 5.91×10^{14}-1.58×10^{15} cm^{-3}, and $D(As) = 7.5\times10^{-16}\pm1.5\times10^{-16}$ cm^2 s^{-1}. The diffusion coefficients for the two samples are essentially the same due to similar Hg vacancy concentrations expected for the same Hg partial pressure and substrate temperature for both samples. As expected, deeper diffusion, as well as lower As concentration, is observed in sample MWIR 3, which was annealed for several hours longer than sample MWIR 2. Figure 5.7 illustrates a comparison between the data sets in both MWIR experiments by superimposing the SIMS data and fitting curves.

All samples exhibited consistent P^+/π step-junction profiles with an As concentration contrast of approximately one to two orders of magnitude in the P^+ and π regions. Two primary components in the arsenic diffusion profiles are observed: 1) a Gaussian and 2) a linear component, as indicated in Figures 5.4 - 5.7. These characteristics contribute to the P^+/π profile of interest. As reported in past studies,[75, 76] the movement of As in HgCdTe during annealing can be described by fast and slow diffusion components. The Gaussian distribution profile is believed to be attributed

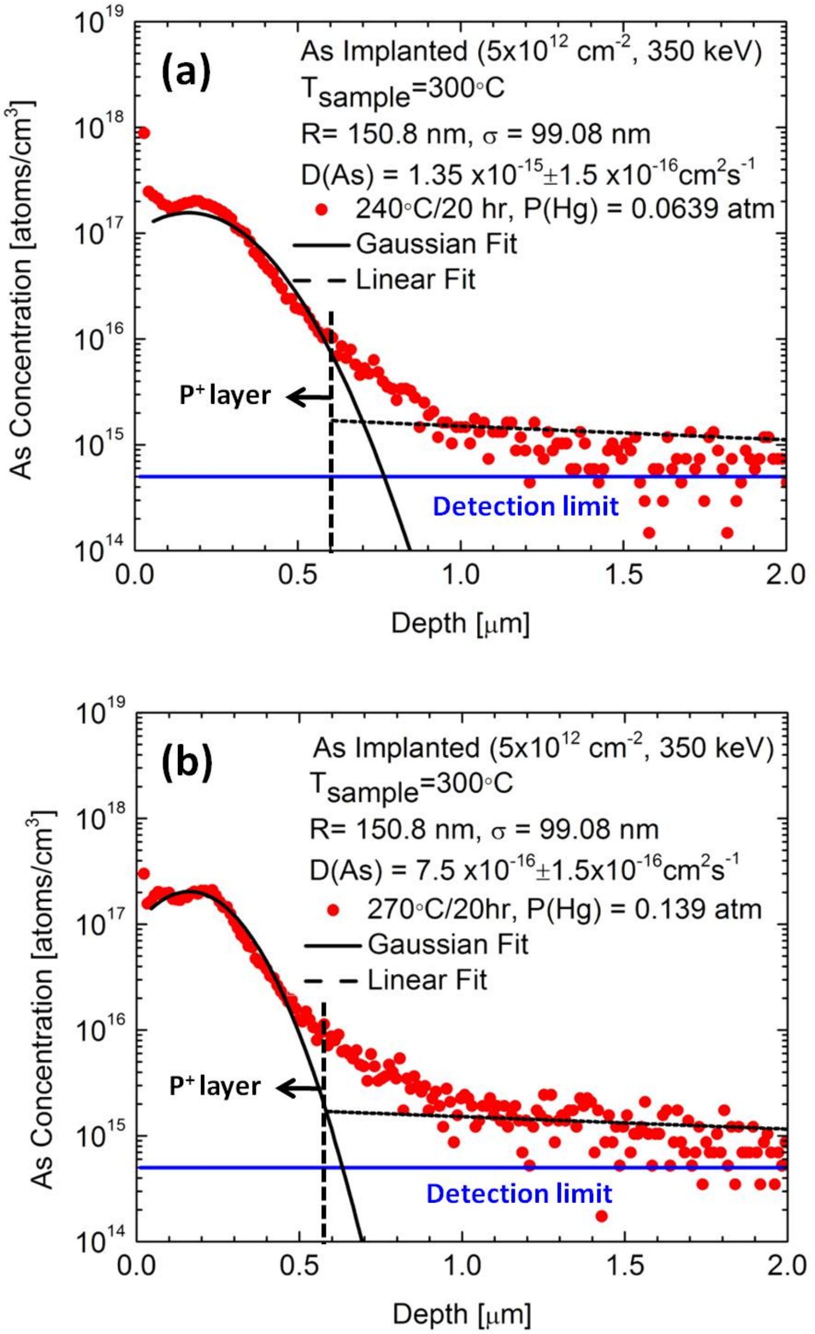

Figure 5.5: Diffusion profiles of MWIR samples (a) MWIR 1 and (b) MWIR 4 for 20 h anneal at $P(Hg) = 0.0639$ atm and $P(Hg) = 0.139$ atm, respectively.

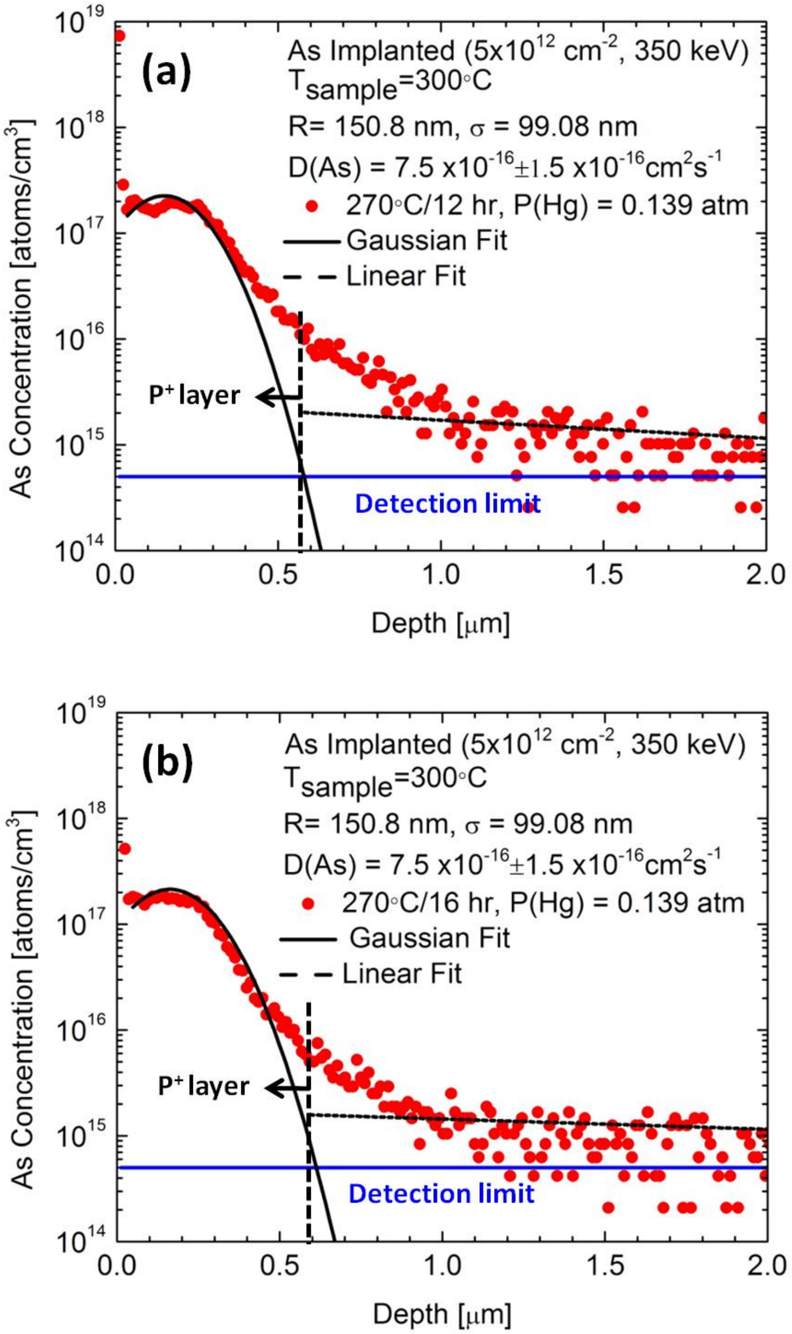

Figure 5.6: Diffusion profiles of MWIR samples (a) MWIR 2 and (b) MWIR 3 for 12 and 16 h anneals, respectively, at $P(Hg) = 0.139$ atm.

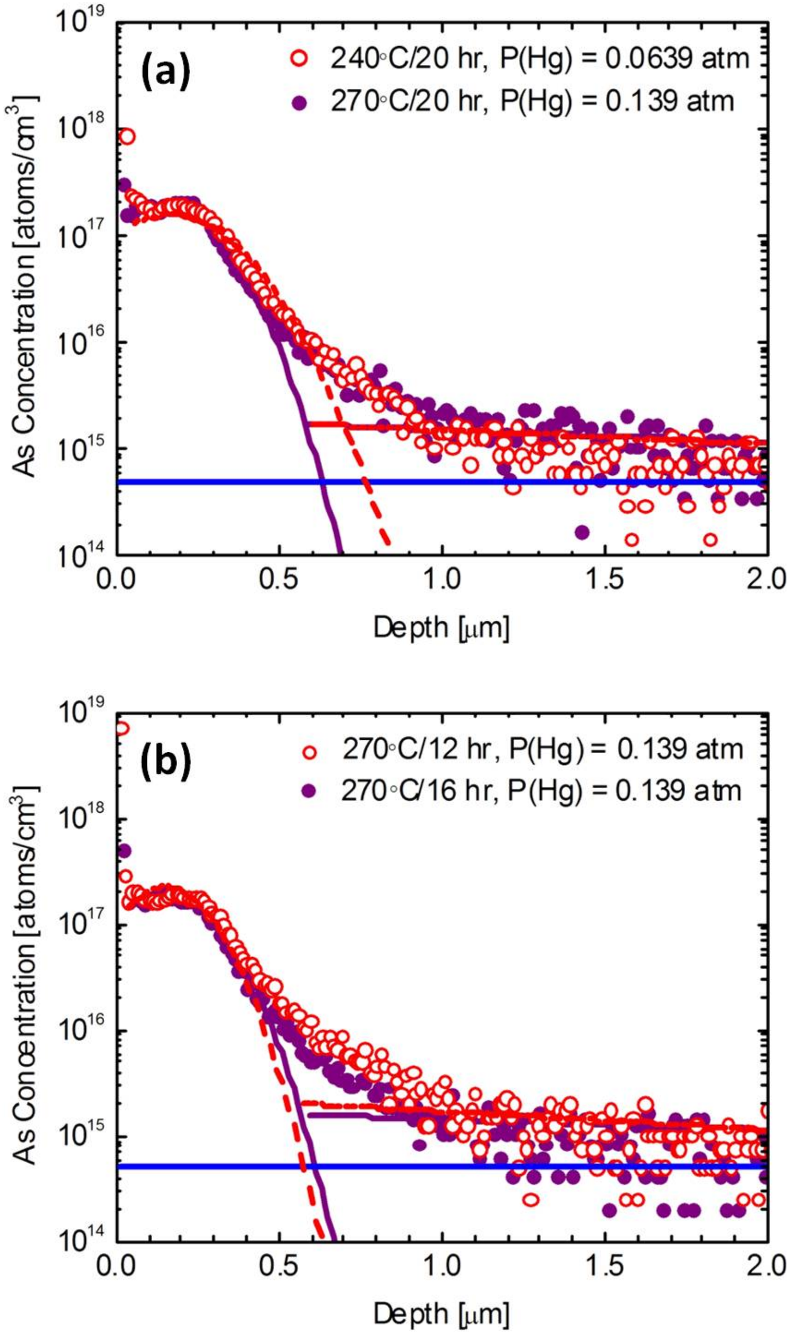

Figure 5.7: Comparison overlays for (a) MWIR 1 vs. MWIR 4 and (b) MWIR 2 vs. MWIR 3. Dashed lines (- -) correspond to fits for data points represented by open circles (◦).

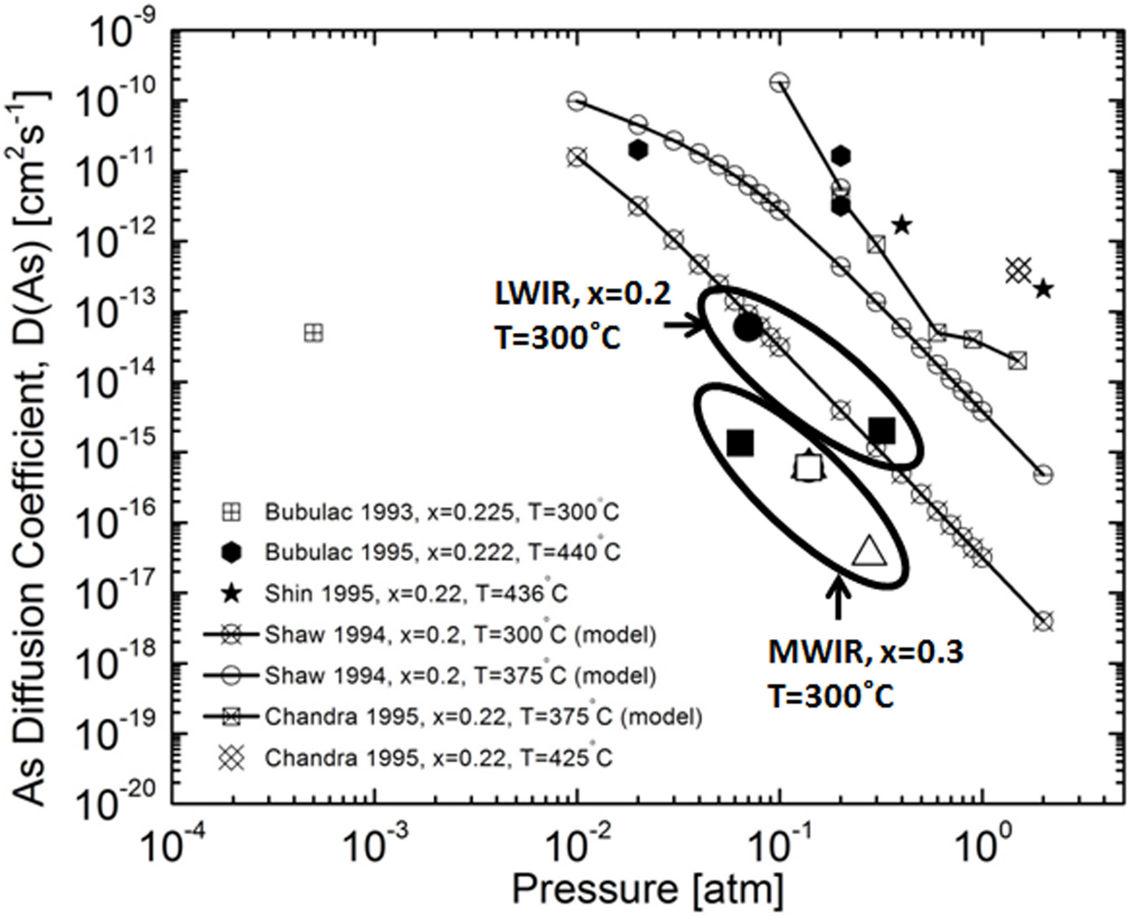

Figure 5.8: Comparison of As diffusion coefficients as a function of $P(Hg)$ for past reported diffusion studies and current LWIR and MWIR experiments [75–79].

to the slower diffusion of arsenic atoms traveling primarily via Hg vacancies. Furthermore, the linear tail of the profile may possibly be a result of arsenic channeling or diffusion by means of other local defects associated with the ion implantation process or as-grown material characteristics. The linear diffusion is not well-controlled and does not seem to follow the trend of the Gaussian profile. The mechanism behind its behavior still remains uncertain and would benefit from further investigation; nonetheless, this component serves to provide low As concentration in the absorber region.

The extracted diffusion coefficients follow the general trend of the inverse relationship between the arsenic diffusion coefficient and the Hg partial pressure as described in numerous past diffusion experiments [75–82]. Figure 5.8 compares the extracted diffusion coefficients against values obtained in past studies. It is important to note that the data points from this study correspond to MBE-grown MWIR and LWIR samples annealed at a low substrate temperature of 300°C for longer annealing times, while most of the past studies focused on LWIR samples grown by MOCVD and LPE methods and annealed for short durations at higher substrate temperatures. There is a difference in the diffusion coefficients obtained for the LWIR and MWIR samples in this study, and this variation is explained by using an experimentally determined expression proposed by Holander-Gleixner et al. [83], which relates the cadmium fraction x, material temperature T, and Hg partial pressure to the equilibrium vacancy concentration C_v in HgCdTe. The relationship is expressed as

$$\begin{aligned} C_v(x,T,P(Hg)) = (5.08\times 10^{27} + 1.1\times 10^{28}x)\frac{1}{(P(Hg))} \\ \cdot exp[-\frac{((1.29+1.36x-1.8x^2+1.375x^3))}{(k_BT)}]. \end{aligned} \tag{5.2}$$

Thus, a lower equilibrium vacancy concentration is present in MWIR samples compared with LWIR, and therefore, the As atoms diffuse more slowly in the MWIR samples, as described by the diffusion coefficients. Similarly, the difference in diffusion coefficients found between the LWIR samples in the current study and those of previous experimental diffusion studies can be explained using Equation 5.2. Past studies focused not only on HgCdTe materials with low x values, but the samples were also annealed at considerably higher temperatures. This reduces the exponential term in Equation 5.2 and increases the equilibrium vacancy concentration in these materials, making them more conducive to arsenic diffusion in HgCdTe and increasing the values of the arsenic diffusion coefficients. The LWIR diffusion coefficients for samples annealed at 300°C lie close to the projected values from the diffusion coefficient model proposed for $Hg_{0.8}Cd_{0.2}Te$ by Shaw et al. [75] for the same temperature. Slight differences in the $D(As)$ values may correspond primarily to non-idealities introduced by the actual experiment. Further studies are needed to compare the diffusion coefficients of LWIR, as well as MWIR, samples annealed at lower substrate temperatures to existing diffusion coefficient models.

5.4 Conclusion

The $P^+/\pi/N^+$ structure device is of high interest due to its ability to reduce Auger generation and recombination mechanisms that limit detector performance at high operating temperatures. In this study, the methods of shallow As ion implantation and deep diffusion annealing were combined to obtain controllable deep diffusion of low arsenic concentrations in HgCdTe HOT samples while retaining the P^+/π step structure. Low As concentrations of 3.35×10^{14}- 2×10^{15} cm^{-3} were achieved in the absorber region using low Hg partial pressure and long anneal times. Reduced arsenic diffusion coefficients were observed in comparison to past studies conducted on HgCdTe samples held at higher substrate temperatures. Lower As diffusion coefficients were also extracted for MWIR samples in comparison to LWIR samples, and this difference is attributed to reduced Hg vacancy concentration associated with alloys with higher cadmium fraction.

CHAPTER VI

Design and Modeling of HgCdTe nBn Detectors

6.1 Overview and Status of nBn Detectors

As HgCdTe IR technology continues to push boundaries to increase operating temperature and achieve larger format array sizes, addressing performance limitations in state-of-the-art *p*-*n* junction photodiodes becomes critical. Decades of research and development on HgCdTe material growth and fabrication process have resulted in the achievement of detectors with dark current limited by intrinsic thermal generation processes (Auger), rather than by extrinsic dark current mechanisms such as surface conduction, Shockley–Read–Hall centers, or trap assisted tunneling for a wide range of operating conditions. However, there are still issues related to controlled *p*-type doping of HgCdTe, namely those associated with *in situ* *p*-type doping via MBE growth techniques. Advanced device structures designed to suppress intrinsic Auger processes and/or achieve multi-spectral detection capabilities will require more complex heterojunction structures that are difficult to attain given the current challenges associated with *p*-type doping of MBE grown HgCdTe. These needs motivate the efforts to explore alternative architectures to overcome these technological setbacks.

Recently, a unipolar IR detector design for III-V InAs-based compound semiconductors with a type-II band offset was proposed by Maimon et al. [31]. The device is termed the nBn detector and provides several advantages over conventional *p*-*n* junction photodiodes by significantly reducing SRH and surface leakage currents and achieving in higher temperature operation. The nBn structure illustrated in Figure 1.16 consists of all n-type layers: a lightly doped n-type absorbing layer ($\sim 10^{16}$ cm^{-2}), a wide bandgap and undoped barrier layer (InAsSb or AlAsSb), and a highly doped contact layer ($\sim 10^{18}$ cm^{-2}). The absorber layer is approximately one to two times the optical absorption length, the barrier layer width is between 50-100 nm to prevent electron tunneling, and the contact layer is typically on the order of several tens of nanometers thick. More interestingly, the heterojunctions at the interfaces of the barrier and contacting n-type layers in the InAs-based system have a nearly zero valence band offset, and the bandgap difference is observed exclusively in the conduction band. The barrier height is large enough ($>$1 eV) to prevent current conduction by thermal excitation of electrons. This special set-up allows the conduction band barrier to selectively block the flow of the majority carrier electron current while simultaneously allowing the flow of minority hole carrier current. Thus, the current is limited to the thermal and photogenerated carriers from the absorber layer. The nBn device is designed to be operated in flatband or with slight depletion, and devices have been reported to operate at 0.6 V bias [33] to enhance photocurrent collection.

The InAs-based nBn detector proposed by Maimon et al. [31] is designed to inhibit two major mechanisms: the SRH and surface leakage currents, and the related noise current. Typically, mid-bandgap SRH trap centers are activated in the depletion region of narrow bandgap photodiodes under bias, and the resulting SRH G-R processes are a major source of dark current, especially at lower temperatures. In the nBn detector, most of the applied bias is dropped across the undoped, wide bandgap barrier layer, reducing SRH G-R processes in the depletion region. If the nBn detector is processed in such a way that the device is delineated by etching only up to but not beyond the contact layer, the wide bandgap barrier can also serve as a passivation layer, suppressing surface leakage currents that would otherwise arise

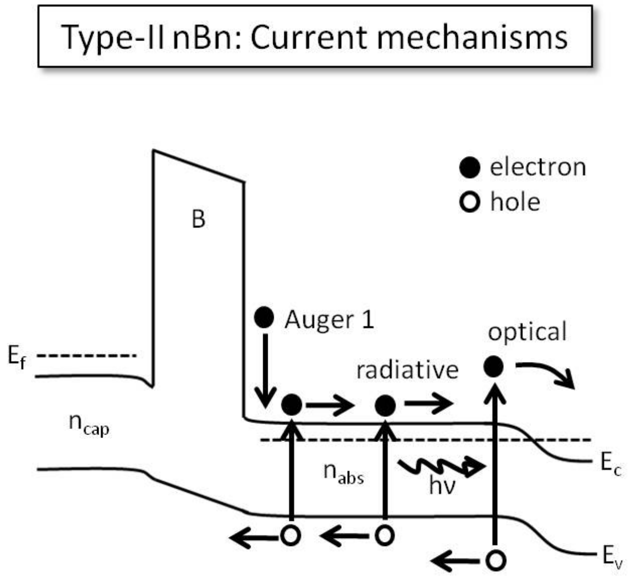

Figure 6.1: Various current mechanisms in type-II, III-V nBn detector under bias.

in the narrow bandgap absorber. This is a significant advantage for III-V materials for which good passivation is not well known and overcomes the limitations imposed by surface leakage currents in addition to eliminating the requirement of separate and complicated passivation steps. Figure 6.1 illustrates the mechanisms that which contribute to the current in an ideal type-II, III-V nBn device: intrinsic Auger 1 generation dominant in n-type materials, background flux induced radiative generation, and optical generation.

A number of related studies [31, 33, 84, 85] have examined the performance of bulk III-V nBn devices. The preliminary data on these devices demonstrate significantly lower dark current and noise compared to p-n photodiodes. Figure 6.2 shows an Arrhenius plot of current of an MBE grown MWIR InAs nBn device with an AlAsb barrier under 295 K background scene conditions [31]. At high temperatures, the device exhibited a thermal activation energy close to that of the InAs bandgap, demonstrating the effective suppression of significant SRH contributions which would otherwise be indicated by a thermal activation energy value near $E_g/2$. Furthermore, the initial data show the device operates in BLIP conditions at temperatures below

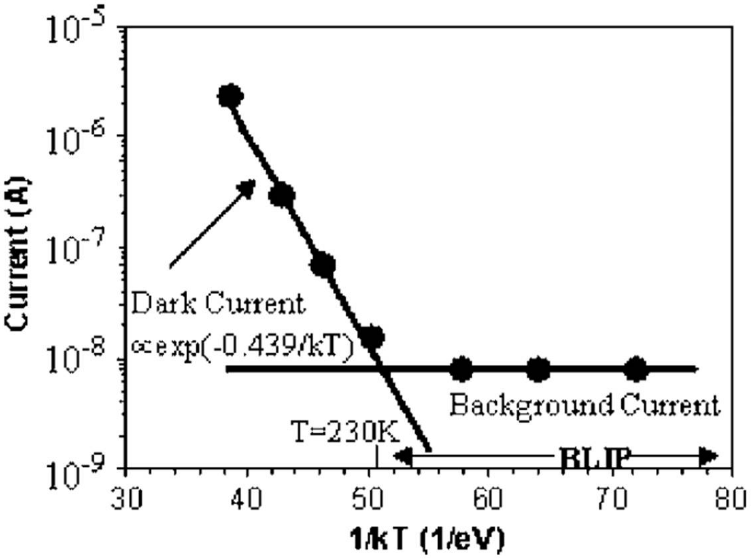

Figure 6.2: Measured dark current of InAs nBn exposed to room temperature background radiation. Adapted from Ref. [31].

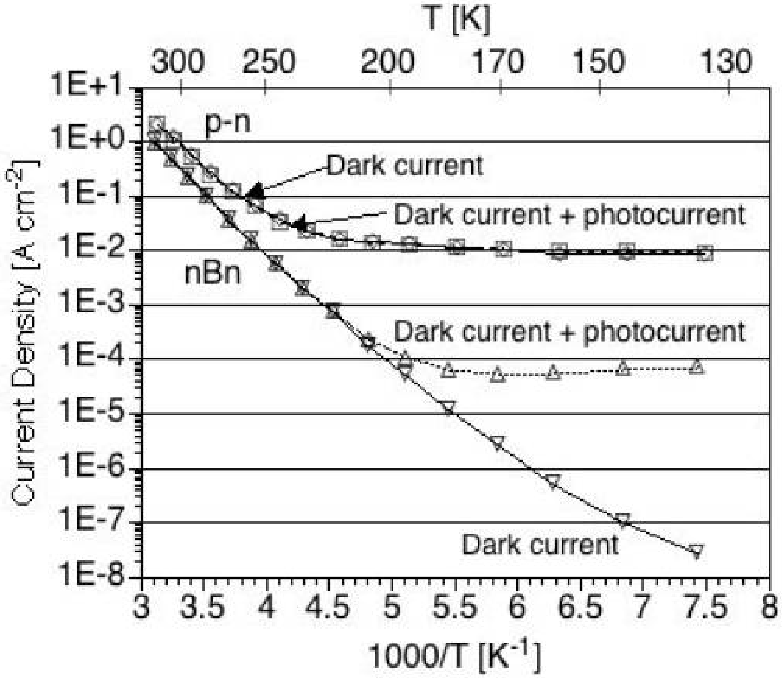

Figure 6.3: Measured current density as a function of temperature for InAs nBn device and commercially obtained InAs reference *p*-*n* photodiode for dark and 300 K blackbody illumination conditions at nominal reverse bias [32].

230 K, at least 100 K higher than values reported for commercial InAs *p*-*n* photodiodes [31]. More importantly, the nBn current at these temperatures is reported to be diffusion limited. HgCdTe and InSb MWIR photodiodes, on the other hand, are limited by SRH under BLIP conditions. Figure 6.3 illustrates the comparative performance of a MWIR InAs nBn device and a reference InAs *p*-*n* photodiode [32]. The dark current density of the *p*-*n* device saturates around 220 K, limited by temperature independent surface conduction. The nBn device, however, is not affected by surface currents down to approximately 135 K. There is roughly a five order of magnitude difference in the measured dark current densities of the nBn and *p*-*n* devices. The data also show that the unpassivated InAs nBn achieves BLIP conditions at approximately 195 K and is thus able to detect the 300 K blackbody where the reference *p*-*n* diode cannot. Other studies have been pursued to further develop barrier integrated devices based on III-V materials such as type-II strained superlattice nBn detectors [84–88], *n*-*N* detectors [89], and XBn photodetectors [90]. The nBn structure serves as a basis for various alternative architectures for high temperature operation.

6.2 Type-I Heterojunction HgCdTe nBn Device

The nBn device structure may also be applicable to implementation in a HgCdTe system which would offer a significant advantage over conventional HgCdTe *p*-*n* junctions by eliminating requirements for *p*-type material and thus, avoiding lower material quality due to implantation induced defects [21–24]. Furthermore, the removal of additional implantation and annealing steps would simplify the detector fabrication process. HgCdTe implementation of the nBn structure has not been pursued since its initial conception [91]. Given the status of the present *p*-*n* junction technology and the advantages of HgCdTe material such as large bandgap tunability and lattice matching capabilities for IR applications, an investigation of an HgCdTe nBn device is warranted and may provide a breakthrough technology for next-generation

MWIR (λ_{co} = 5 μm) and LWIR (λ_{co} = 12 μm) nBn Parameters						
Layer	Thickness	Cd composition	Doping	E_{trap}	SRH lifetime	F_1F_2
Top	$t_{n_{cap}} = 1\ \mu$m	$x_{cap} = x_{abs} + 0.1$	$N_D = 5{\times}10^{15}$ cm^{-3}	$0.25E_g$	$\tau_{n0} = 10\ \mu$s $\tau_{p0} = 1\ \mu$s	0.3
Barrier	$t_B = 50$ nm	$x_{B,M} = 0.64$ $x_{B,L} = 0.45$	$N_D = 7{\times}10^{14}$ cm^{-3}			
Absorber	$t_{abs} = 10\ \mu$m	x_{abs} = varied for λ_c	$N_D = 7{\times}10^{14}$ cm^{-3}			

MWIR (λ_{co} = 5 μm) and LWIR (λ_{co} = 12 μm) DLPH Parameters						
Layer	Thickness	Cd composition	Doping	E_{trap}	SRH lifetime	F_1F_2
Top	$t_{p+} = 1\ \mu$m	$x_{p+} = x_{abs} + 0.1$	$N_A = 5{\times}10^{17}$ cm^{-3}	$0.25E_g$	$\tau_{n0} = 10\ \mu$s $\tau_{p0} = 1\ \mu$s	0.3
Absorber	$t_{abs,M} = 5\ \mu$m $t_{abs,L} = 10\ \mu$m	x_{abs} = varied for λ_c	$N_D = 8{\times}10^{14}$ cm^{-3}			

Table 6.1: MWIR and LWIR nBn and DLPH device simulation parameters.

infrared detectors. In this study, the performance characteristics of optimized MWIR and LWIR HgCdTe nBn devices are simulated using a numerical model and compared to MWIR and LWIR *p*-*n* DLPH structures [63–65]. The calculated results will be analyzed and discussed for a better understanding of this alternative detector design.

6.3 Modeling the HgCdTe nBn Detector

To examine the feasibility and performance of the HgCdTe nBn detector, numerical simulations were performed using the commercial software Sentaurus Device. The simulation methodology and model validation utilized in this study are described in detail in Chapter III. Table 6.1 lists the specific material parameters used in the simulations of MWIR and LWIR nBn and DLPH structures.

6.3.1 HgCdTe nBn Device Structure

Like the InAs-based nBn, the HgCdTe nBn structure consists of three *n*-type layers: 1) a top contact or cap, 2) a wide bandgap barrier, and 3) a thick, narrow bandgap absorber. The basic structure and band diagram of the HgCdTe nBn device in operation is shown in Figure 6.4. While the overall operation mechanisms of the two types of devices are similar, there are several key differences. Firstly, the heterojunction interfaces of the HgCdTe nBn exhibit a type-I band line-up. This is an important feature because it implies there exists a non-zero valence band offset at the barrier layer interfaces in the HgCdTe device structure. The presence of a valence band barrier poses a non-trivial challenge to the operation of the HgCdTe nBn detector which relies on the conduction of minority carrier holes. However, this issue can be addressed by carefully optimizing the structural parameters of the device as discussed in the subsequent section. Moreover, a significant valence band barrier ΔE_v exists at equilibrium such that a top negative bias is required for the operation of the HgCdTe nBn detector. Finally, due to the nature of HgCdTe, the conduction band barrier ΔE_c is less than 1 eV. The low ΔE_c value increases the likelihood of carriers tunneling through or overcoming the barrier by thermal excitation. This can be addressed by reducing the bandgap and/or slightly reducing the doping concentration of the cap layer, or increasing the barrier layer thickness. Careful selection of structural parameters is necessary to maximize device performance.

6.3.2 Preliminary Design Considerations

Compared to other III-V structures that have been demonstrated, the HgCdTe nBn structure presented here consists of lower doping concentrations in the cap and absorber regions and employs lightly and similarly doped absorber and barrier layers. The choice to dope the barrier layer was made under the assumption that the realization of a very thin, undoped barrier during MBE growth would be challenging and potentially unrealistic. The light doping results in the formation of a bias-induced depletion region that extends into the nBn active layer when an operating voltage is applied. SRH G-R processes are therefore present in the narrow bandgap region; however, dark current contributions due to the thermal G-R processes appear to be nominal as evidenced by the low overall nBn dark current density achieved compa-

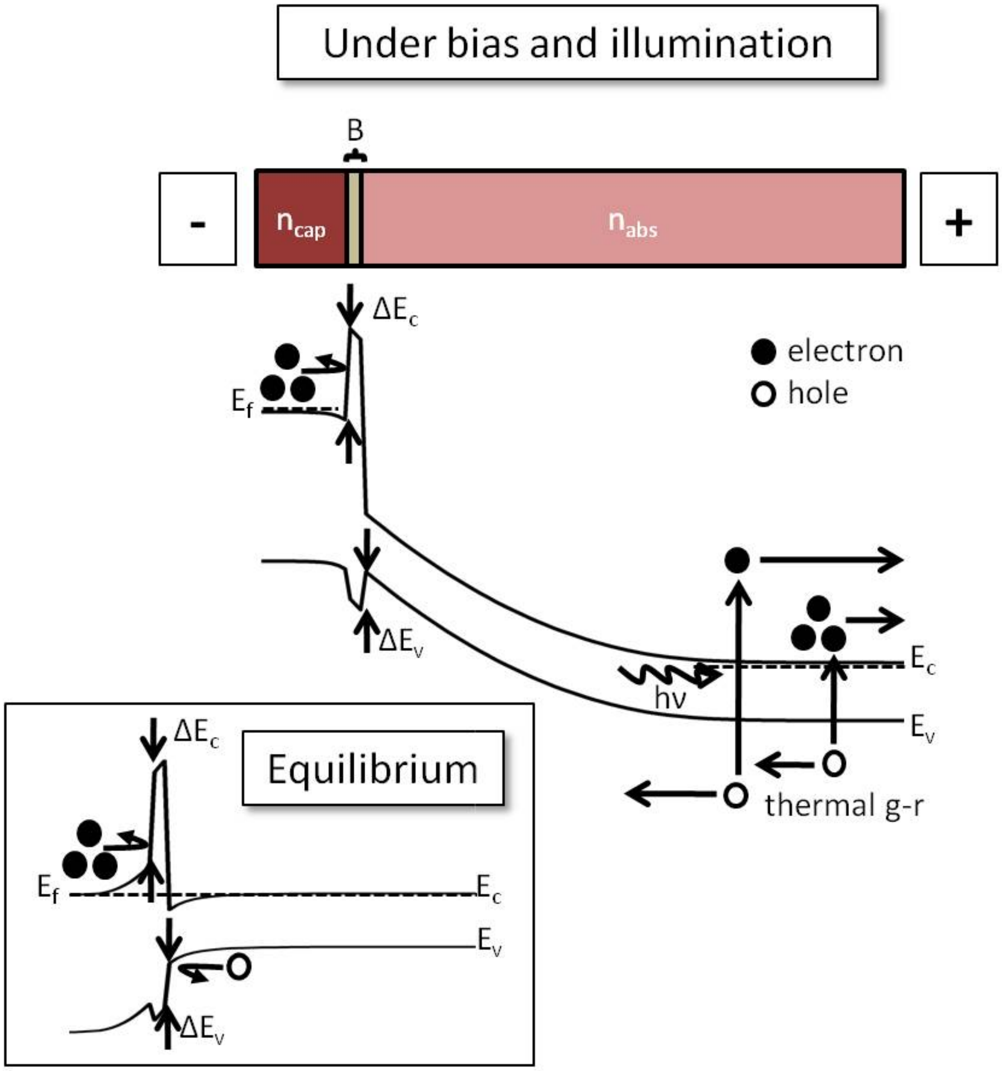

Figure 6.4: Schematic and band diagrams of HgCdTe nBn detector at equilibrium (inset) and under reverse bias and illumination conditions.

rable to the DLPH structure as discussed in the next section. Further reduction in the barrier doping, to the extent that it is possible to implement experimentally, is expected to minimize the width of the depletion region in the active layer.

The nBn cap layer (n_{cap}) was designed to have a wider bandgap for improved valence band alignment, as illustrated in the band diagrams in Figure 6.4, and the Cd composition $x_{cap} = x_{abs}$+0.1 is chosen in this work.

A value of 450 mV reverse bias (negative voltage applied to n_{cap} region) was selected for nBn device calculations to ensure operation in the dark saturation current region when determining performance characteristic values. Biases below 450 mV may also be sufficient for operation as long as the J_{dark} is at or above the saturation threshold. Bias trade-offs include improved carrier collection at the expense of conduction band barrier height with increasing bias.

The optimization calculations of the MWIR and LWIR nBn structures were performed at temperatures of 95 K and 80 K, respectively. Band-to-band tunneling contributions were not included in this study and will be examined along with other tunneling mechanisms in future work. Furthermore, strain effects were not included in the calculations despite the large bandgap differences at the heterojunction interfaces of the barrier layer. Misfit dislocations are not expected to be a significant issue due to the high bandgap tunability of HgCdTe with small lattice mismatch.

The MWIR and LWIR nBn device structures were optimized to achieve the highest peak D^* (optimal combination of low dark current and high responsivity) by varying values for absorber thickness t_{abs}, barrier thickness t_B, doping concentration n_{cap}, and barrier composition x_B.

6.3.2.1 Optimizing Absorber and Barrier Layer Thicknesses

The absorber layer thickness affects the overall absorption of the long infrared wavelengths, and larger calculated responsivity was observed for structures with larger

t_{abs}. An absorber length of 10 μm was determined to be the most optimal for both MWIR and LWIR nBn devices. While these values were used for performance calculations, shorter absorber lengths may be more practical for actual nBn structures where thermal G-R processes in the bulk can negatively affect performance more significantly than the benefits provided by the increased absorption.

The t_B parameter exhibits a trade-off with thinner t_B resulting in higher J_{dark} but also high D^* values. It is noted that $t_B = 40$ nm was used for certain optimization aspects such as barrier composition and cap layer doping prior to barrier thickness optimization; however, the optimized value of $t_B = 50$ nm is selected as the ideal upper limit for the HgCdTe nBn device performance. Although tunneling contributions were not accounted for in this simulation study, preliminary calculations show the tunneling probability and associated current contributions are relatively small. Tunneling current through the barrier may be controlled by providing a sufficient barrier width and/or height, where optimal barrier parameters accounting for tunneling current may shift from the values of this study and will be examined in future work. Experimentally, potential issues with compositional uniformity and interdiffusion at the junctions, as well as tunneling effects on device performance, may need to be considered when fabricating a narrow barrier layer.

6.3.2.2 Optimizing Cap Layer Doping Concentration

Because the HgCdTe nBn conduction band barrier is less <1 eV, high n_{cap} doping concentrations can increase dark current density due to the greater number of majority carriers surmounting the barrier. Optimization was performed to select a moderate cap layer doping concentration of 5×10^{15} cm^{-3}, lower than the values typically used for *p*-type doping of the cap layer in the DLPH structure.

6.3.2.3 Optimizing Barrier Layer Composition

The choice of barrier composition x_B was found to be the most critical parameter in determining device behavior, where the dependence of peak D^* on barrier composition for both MWIR and LWIR nBn devices is shown in Figure 6.5a and Figure 6.6. The x_B value has the largest influence in determining both the barrier height ΔE_c in the conduction band that limits majority carrier electron flow to reduce dark current, as well as the barrier height in the valence band ΔE_v that would inhibit the collection of photogenerated carriers. Therefore, a trade-off exists where careful selection of the barrier composition is required. Too low a composition can result in increased noise current due to the larger number of majority carriers surmounting the conduction band barrier and contributing to the overall current; too high a composition can result in a large valence band barrier which inhibits carrier collection and reduces the device responsivity as shown in Figure 6.5b. Optimal x_B values of 0.64 and 0.45 were determined for MWIR and LWIR nBn devices, respectively, at fixed temperatures. It is noted that the large MWIR Cd composition causes the HgCdTe bandgap to behave somewhat differently than lower composition (x <0.5) HgCdTe materials as a function of temperature which can affect device performance. This issue can be countered by optimizing the x_B value for the temperatures at which the device will most likely be operated.

6.3.3 Final Design Considerations

The proposed nBn structure requires etching past the barrier layer for isolation in mesa configuration due to the doping in the barrier layers. This process may result in surface defects which can cause sidewall leakage currents. Thus, any exposed HgCdTe material must be passivated with ZnS or CdTe, a well-established technique. The optimal material and geometric values selected for the nBn and DLPH structures are specified in Table 6.1. The optimized parameters for the ideal HgCdTe

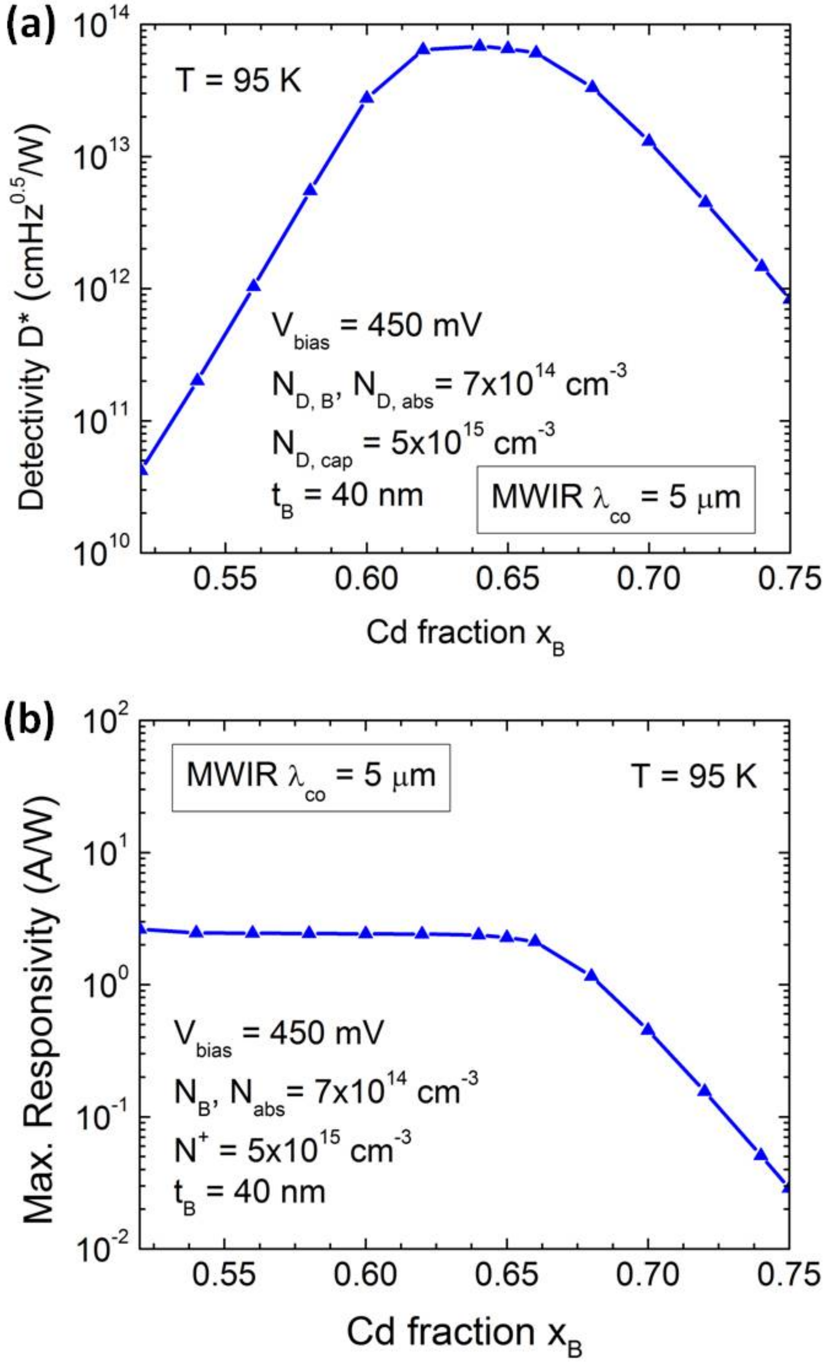

Figure 6.5: Optimization of x_B for MWIR nBn structure by examining (a) peak detectivity and (b) peak responsivity values at 95 K.

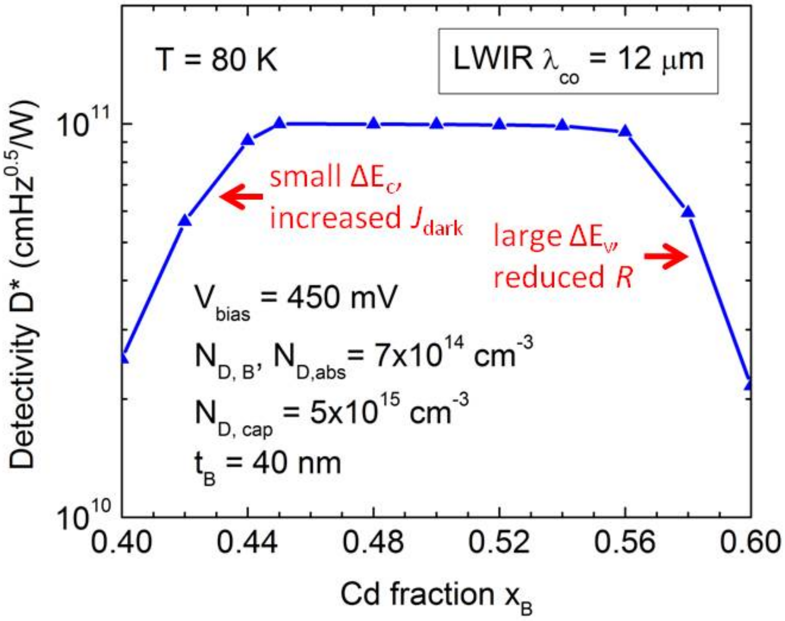

Figure 6.6: Optimization of x_B for LWIR nBn structure by examining peak detectivity values at 80 K.

LWIR DLPH device were selected using similar methodology as described for the nBn structure. Extrinsic, process-induced current components are not included in the device modeling. The final optimized structural parameters for the MWIR and LWIR HgCdTe nBn devices are listed in Table 6.1. The optimized band diagrams of an LWIR HgCdTe nBn are illustrated in Figure 6.7a and 6.7b at equilibrium and under reverse bias conditions, respectively.

6.3.4 Current Contributions in HgCdTe nBn Device

Figure 6.8 summarizes the mechanisms that affect the current in a type-I, HgCdTe nBn device. These mechanisms include intrinsic Auger 1 generation dominant in n-type materials, background flux induced radiative generation, SRH generation due to activated trap centers in depletion region, barrier tunneling, perimeter leakage, and optical generation. While barrier tunneling and perimeter leakage non-idealities were

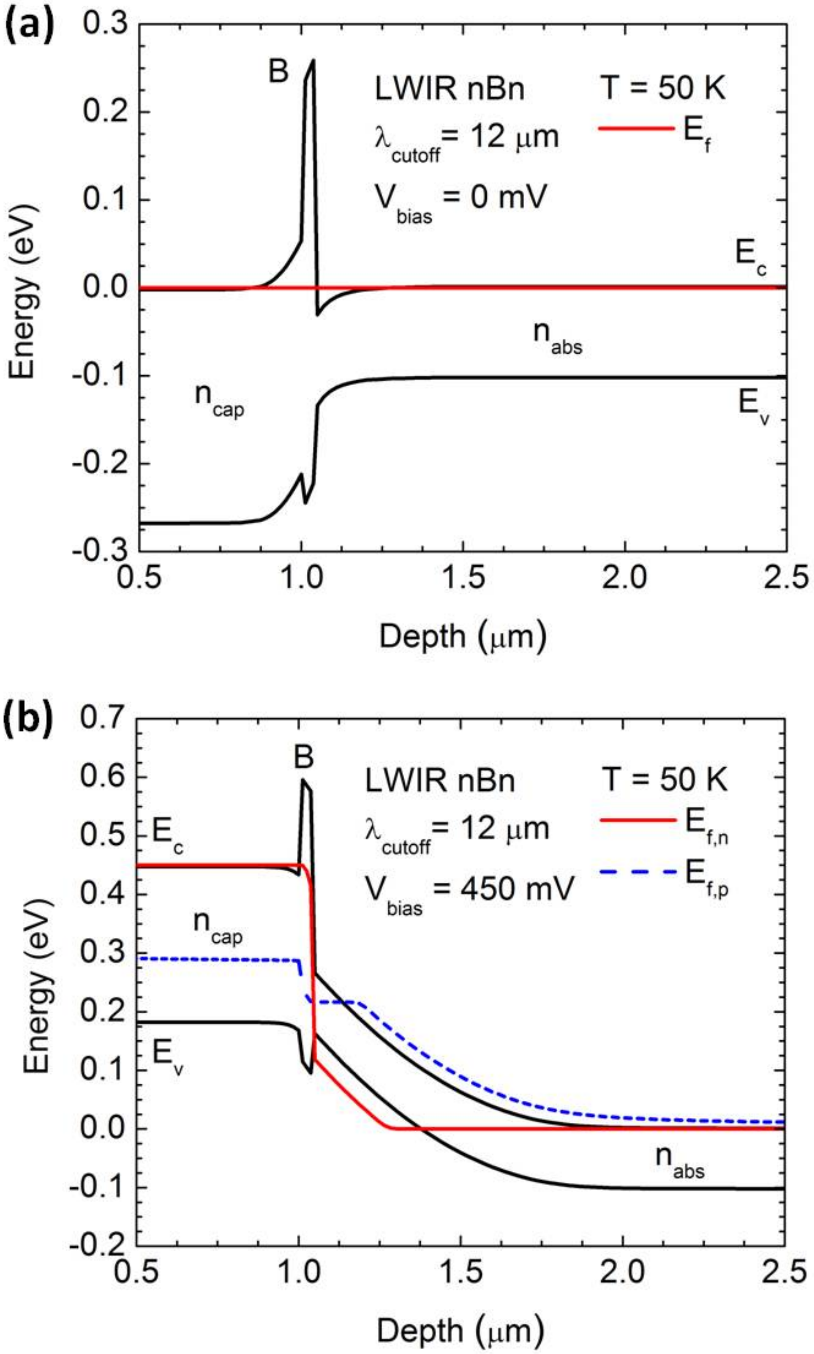

Figure 6.7: Calculated energy band diagrams of HgCdTe nBn photodetector device (a) at equilibrium and (b) under reverse bias.

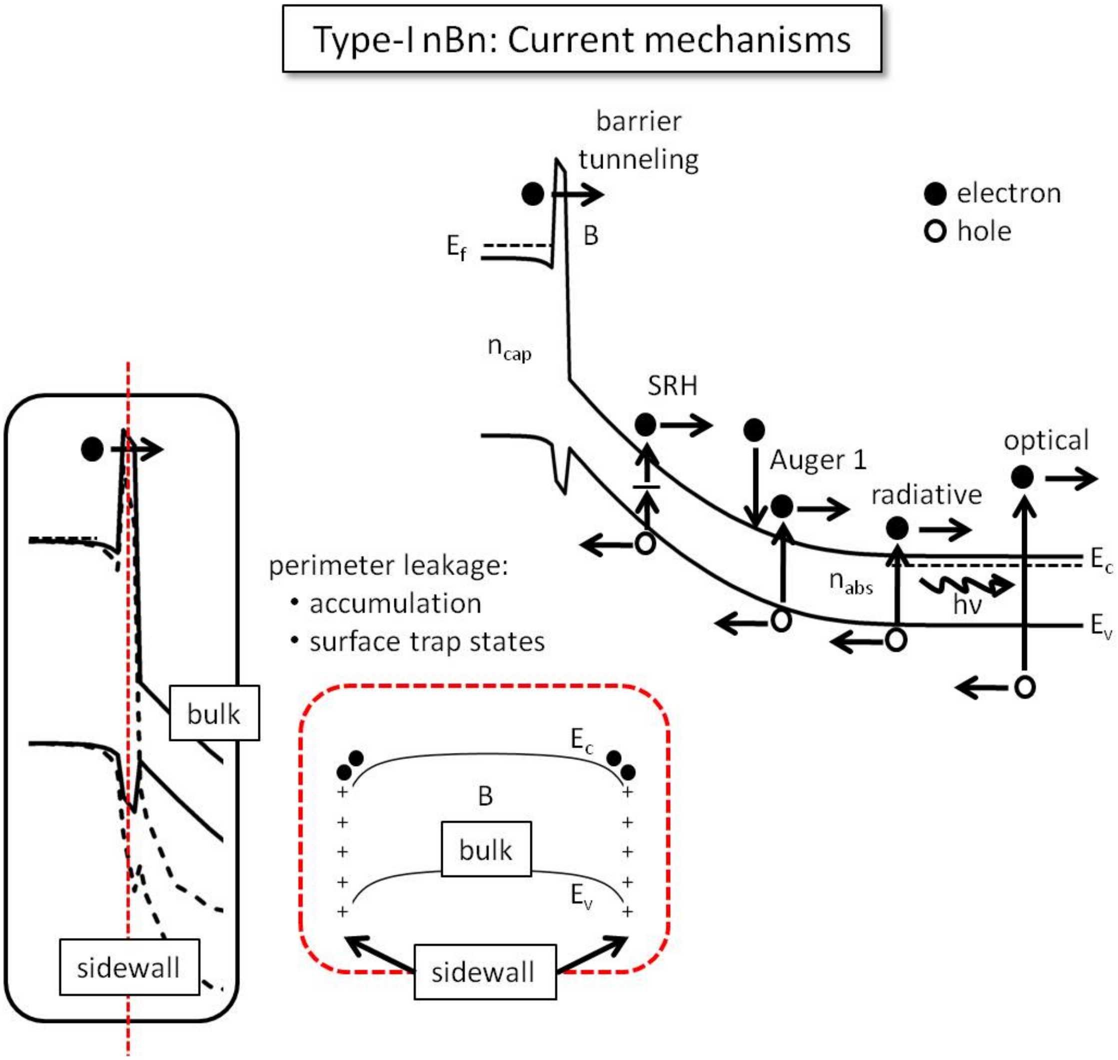

Figure 6.8: Various current mechanisms in type-I, HgCdTe nBn detector under bias.

neglected in the numerical device model, these effects are important to consider in actual fabricated device structures such as those discussed in Chapter VII.

6.4 Results and Discussion

6.4.1 J_{dark} Characteristics

The representative current-voltage characteristics for the LWIR nBn device are shown in Figure 6.9 for several temperatures between 80 K and 95 K. Unique behavior is observed for the nBn I-V characteristics due to the barrier in the valence band.

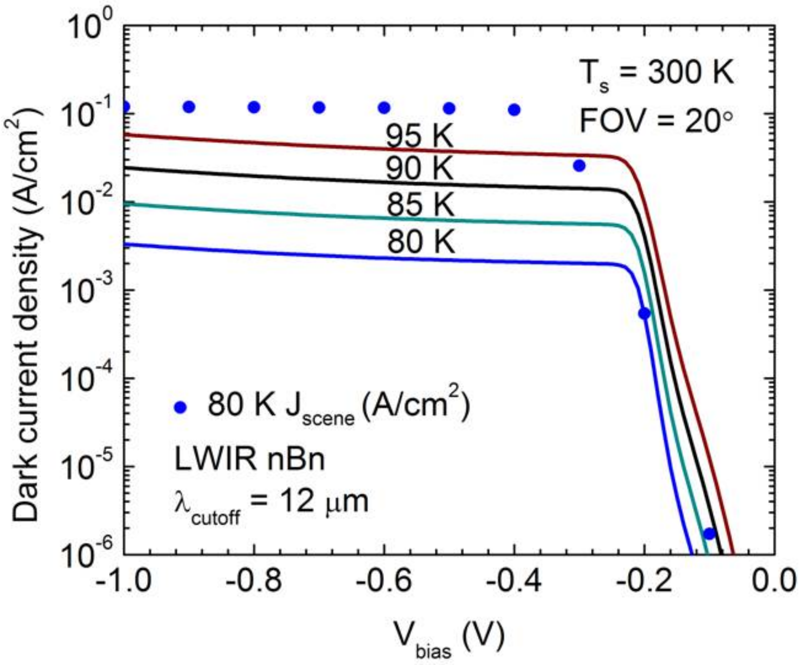

Figure 6.9: Simulated LWIR nBn current-voltage characteristics at varying temperatures and 300 K background scene induced current in 80 K device.

A 'turn-on' feature is evident, reflected as an inflection in the current for a given bias and indicating the proper alignment of the n_{cap} and absorber region bandedges and unrestricted flow of hole current arising from minority carrier generation in the absorber layer. At larger reverse biases beyond the turn-on region, the dark current density saturates. The dark current density is SRH limited for the temperatures shown.

The dark current density values for MWIR and LWIR devices as a function of temperature for specified biases are shown in Figure 6.10. All calculations for the DLPH structure were performed at a 300 mV bias, which may be considered larger than conventional operating biases for typical p-on-n devices. Verification in the author's previous simulation work [92] has shown no significant changes in dark current density for lower biases. At lower temperatures, a convergence in the nBn and DLPH device J_{dark} values is observed in both MWIR and LWIR devices as shown in

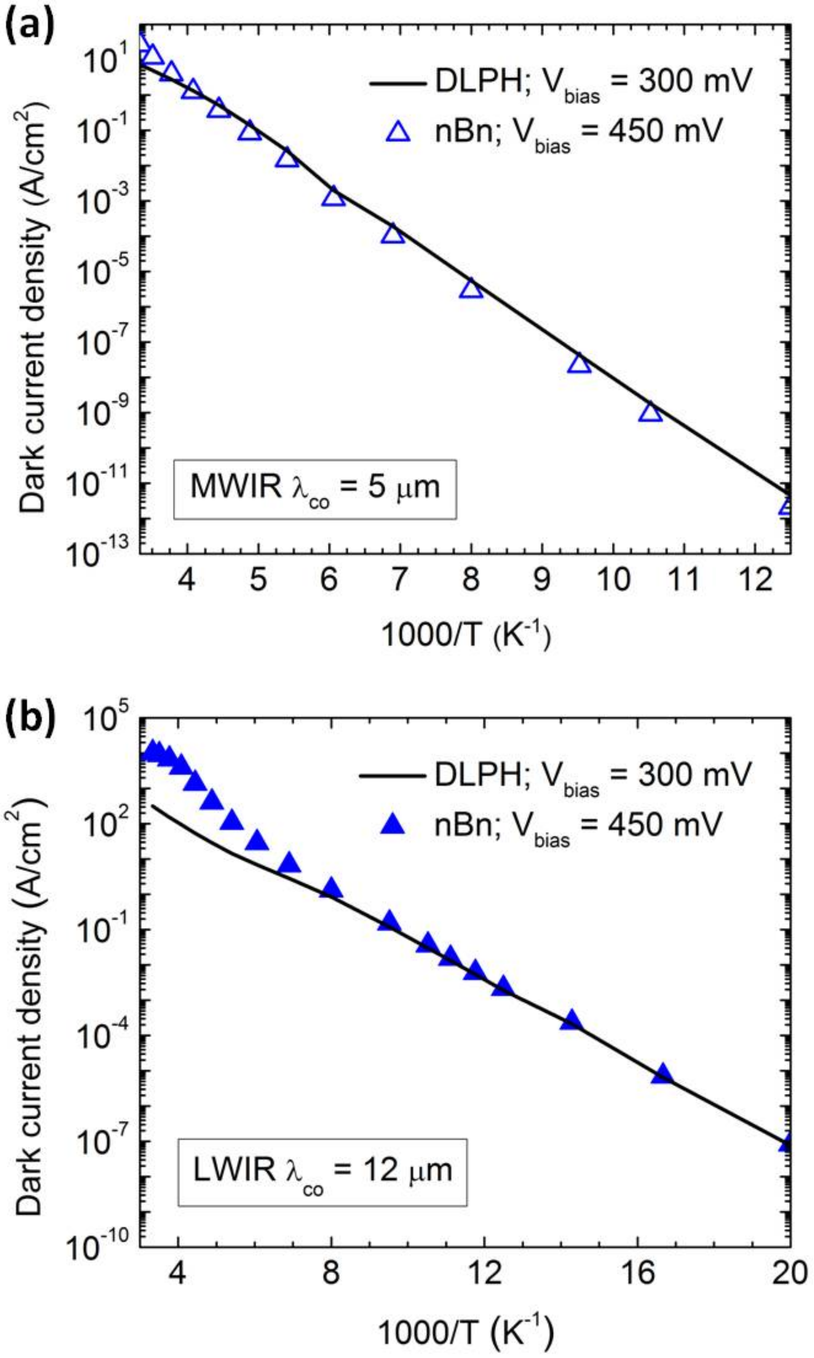

Figure 6.10: Calculated dark current density at varying temperatures for (a) MWIR and (b) LWIR nBn and DLPH structures.

Figure 6.10. This behavior is attributed to SRH-limited current in both structures caused by extrinsic generation processes in the depletion region formed in the absorber layer. A closer look shows that the J_{dark} values for the MWIR nBn device are slightly lower than MWIR DLPH devices. This is believed to be due to the increase in the barrier bandgap for $Hg_{1-x}Cd_xTe$ with large x values with decreasing temperature,(the optimized x_B is held constant over temperature) which in turn increases both ΔE_c and ΔE_v, further suppressing majority carriers from the cap layer but also reducing hole current. This behavior is also reflected in slightly decreased peak D^* values due to reduced responsivity observed for a similar range of temperatures as shown in Figure 6.12a. With increasing temperature, the MWIR nBn device exhibits higher dark current becoming diffusion limited for temperatures greater than ∼150 K. The LWIR nBn device is diffusion limited for temperatures above ∼120 K. At higher temperatures, the J_{dark} values for MWIR and LWIR nBn devices become larger than those of the DLPH structure and are attributed to the increasing numbers of majority carriers surmounting the conduction band barrier. This behavior is more pronounced in the LWIR nBn device which has a smaller conduction band barrier.

6.4.2 Spectral Response

Figure 6.11 shows the responsivity of both nBn and DLPH structures as a function of wavelength. The optical responses are comparable for the optimized devices, with slightly lower responsivity values calculated for nBn near the cutoff wavelength, resulting from reduced carrier collection due to the valence band barrier. A slight increase observed in responsivity at shorter wavelengths may be attributed to effects of photogenerated carriers modifying the nBn barrier height. However, this is not of significant concern as the noise current would be equivalently amplified, leaving the overall D^* unaffected.

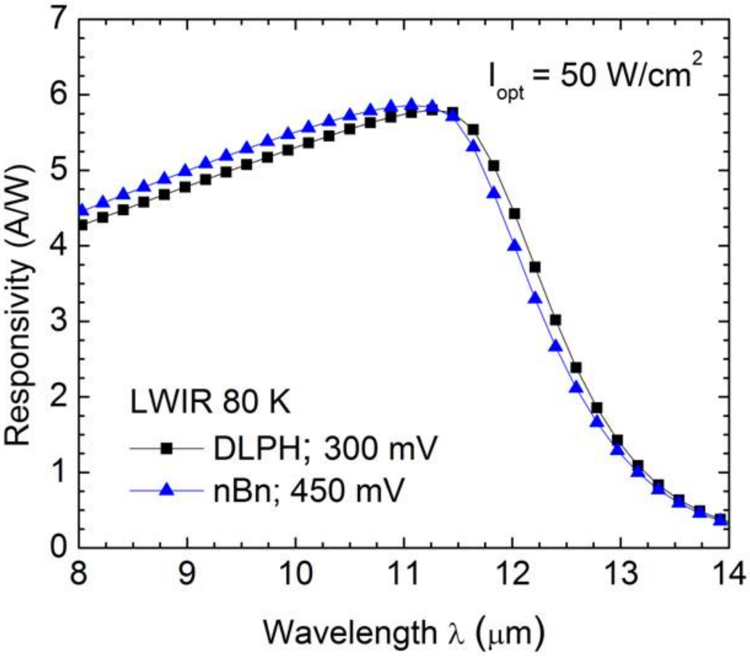

Figure 6.11: Simulated responsivity for LWIR nBn and DLPH structures at 80 K.

6.4.3 Peak D^*

The peak D^* values for MWIR and LWIR devices as a function of temperature are illustrated in Figure 6.12. Overall, comparable peak D^* values are observed for both MWIR and LWIR nBn and DLPH structures in the range of temperatures examined. Further improvement of performance characteristics may be achieved by reiterating the structural optimization of the devices for specific operating temperatures. Unrealistic quantum efficiency values greater than 100% were obtained for the nBn devices at temperatures above 225 K (MWIR) and 95 K (LWIR). The anomalous behavior may be attributed to non-ideal changes in the simulated potential barriers due to photogenerated carriers, but D^* values for temperatures within those ranges were ignored for the time being due to the uncertainty and validity of the underlying mechanism.

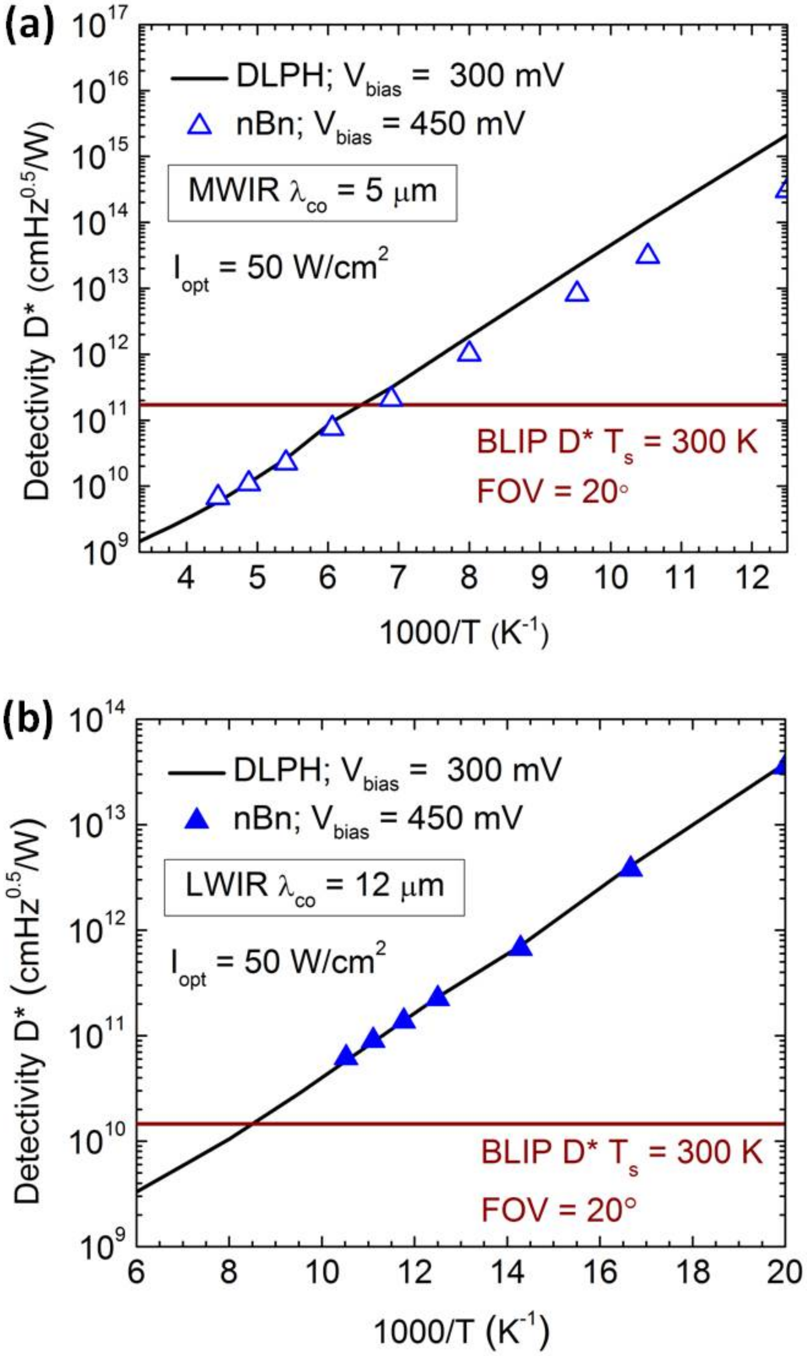

Figure 6.12: Calculated peak detectivity at varying temperatures for (a) MWIR and (b) LWIR nBn and DLPH structures.

6.5 Conclusion

This investigation has demonstrated that the HgCdTe nBn device is potentially capable of achieving performance equivalent to the ideal DLPH detector. Comparable responsivity, low J_{dark}, and high D^* values rival those of the DLPH device without requiring p-type doping in this alternative unipolar design. This initial study suggests that the HgCdTe nBn detector may be a promising solution for achieving high performance with a simplified device architecture. The structure is well suited to address processing technology limitations such as achieving low, controllable *in situ* p-type doping with molecular beam epitaxy growth techniques. Moreover, strategic structural optimizations in future work may lead to enhanced HgCdTe nBn performance with significant reduction in SRH G-R processes, resulting in values closer to those obtained by InAs-based nBn devices. Furthermore, the selective carrier conduction mechanism facilitated by the barrier-integrated design may be incorporated into next-generation detector structures [93] to suppress intrinsic Auger carrier generation. The following chapter focuses on realizing the HgCdTe nBn device as a proof of concept.

CHAPTER VII

Experimental Demonstration of MWIR and LWIR HgCdTe nBn Detectors

7.1 Background and Motivation

High-performance IR photodetectors are based on narrow bandgap semiconductors including HgCdTe, In(As,Sb), lead salt, and InAs/GaSb strained layer superlattices, where a *p*-*n* junction photodiode is typically used for IR focal plane arrays. While the conventional *p*-*n* configuration has proven successful for IR detectors, device fabrication and the achievement of excellent performance characteristics are challenging in narrow bandgap materials due to surface conducting paths and control over doping levels and defect concentrations. As suggested by the modeling study in Chapter VI, a unipolar nBn approach may be adopted for type-I HgCdTe IR detectors to address some of these challenges. A HgCdTe implementation of the unipolar nBn design would enable further development of advanced next-generation HgCdTe devices such as stacked multi-spectral detectors where complex doping profiles may not be feasible with both *n*-type and *p*-type doping. The combined benefits of a simplified fabrication process and the favorable HgCdTe material properties for IR applications strongly motivate the study of the HgCdTe nBn device.

This chapter describes the first-reported experimental demonstration of MBE grown MWIR and LWIR HgCdTe nBn single element photodetectors. Results from electrical and optical measurement are used to evaluate the detector performance and understand the limiting mechanisms. The objective of this study is to realize a working HgCdTe nBn detector validated by barrier influenced I-V characteristics and wavelength dependent photoresponse.

7.2 Experimental Approach

An overview of the experimental approach is illustrated in Figure 7.1. The prototype development comprises two iterations. In the first iteration, MWIR and LWIR nBn layer structures loosely based on optimized parameters were grown in separate runs by MBE, but processed in the same lot during device fabrication. The samples were then electrically and optically characterized to examine nBn device operation and behavior. Based on the initial results, strategic modifications were made to the MWIR nBn structure to improve performance, and the changes were incorporated into the second-iteration layer growth. New devices were fabricated from the second-iteration nBn structure, and electrical and optical measurements were performed to characterize the detector. The following sections describe each portion of the study in detail.

7.3 Experiment Methodology: MBE nBn Layer Growth

7.3.1 HgCdTe nBn Layer Growth

The HgCdTe nBn structures were grown by MBE engineers at a collaborating company, EPIR Technologies, Inc. 30 mm×30 mm bulk CdZnTe (211)B-oriented substrates purchased from Nikko Materials, Inc., were chemically cleaned and etched in a bromine/methanol solution prior to MBE growth. The substrates were placed into the growth chamber of a Riber 32 MBE system equipped with a reflection high-

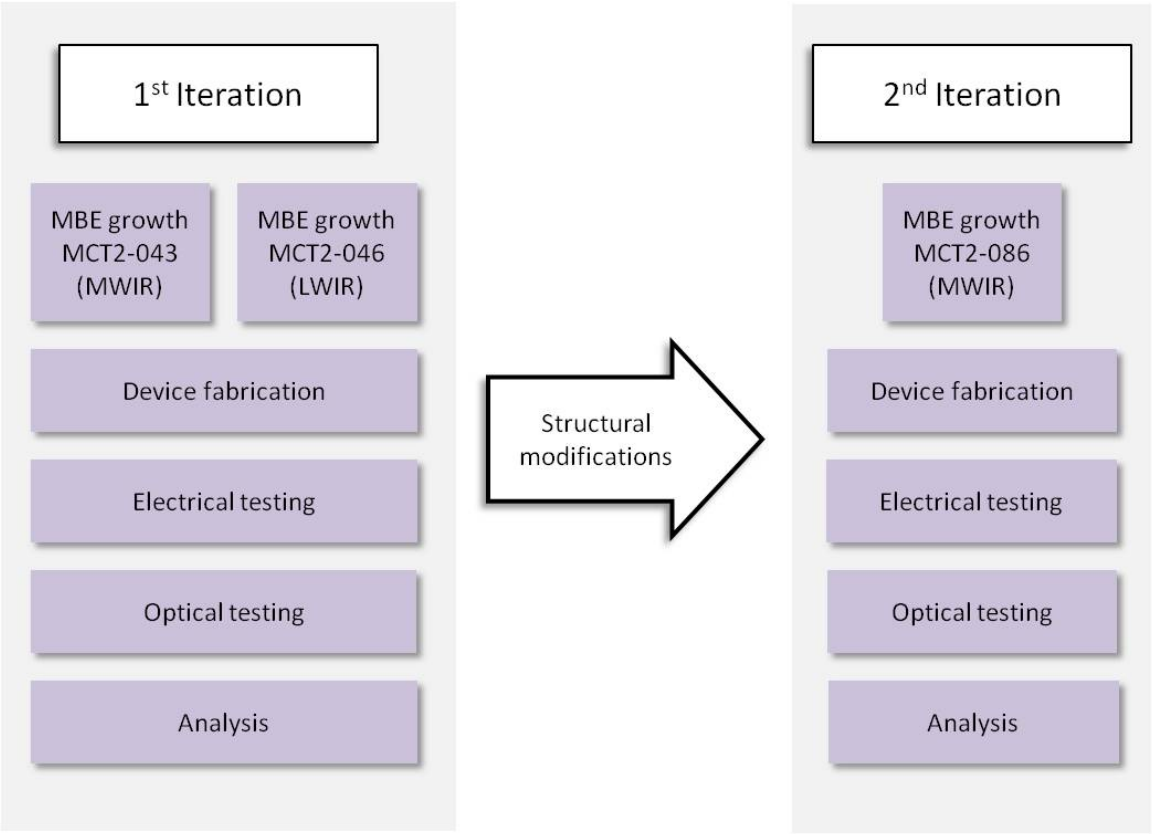

Figure 7.1: Experimental approach of first and second iteration HgCdTe nBn device prototypes.

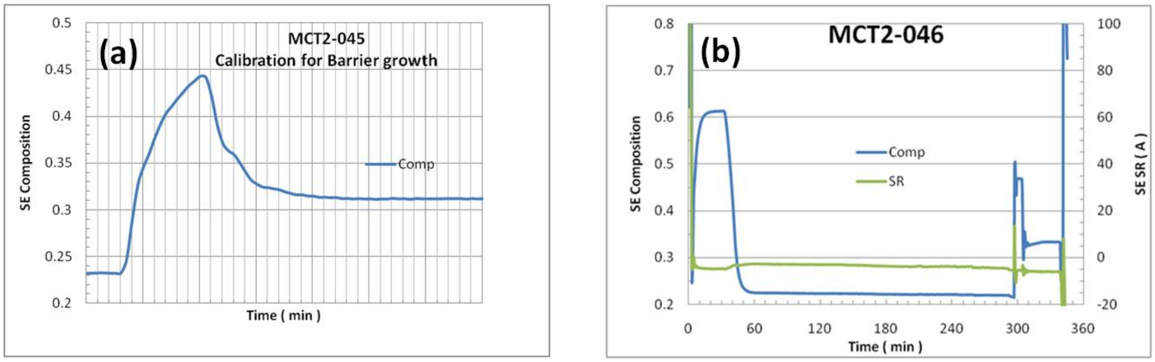

Figure 7.2: SE data showing (a) Cd composition for LWIR nBn calibration (MCT2-045) sample and (b) Cd composition and surface roughness for optimized first-iteration LWIR (MCT2-046) nBn structure.

energy electron diffraction (RHEED) gun, a Hg cell, and a pyrometer. Each substrate was heated to above 350° to remove excess Te and native oxides present on the growth surface and expose fresh CdZnTe for HgCdTe nucleation. The substrate temperatures were measured using a pyrometer. RHEED was used to monitor substrate preparation, growth of the crystal layers, and interface formation. The epitaxial growth conditions were optimized to facilitate 2-D growth of HgCdTe on the substrate from the onset of nucleation. Solid Te, Hg, and CdTe source materials were used in the effusion cells, and the cell fluxes were adjusted by controlling the cell temperature to achieve the target compositions and growth rates for the HgCdTe material. Because the effusion cells can take several minutes to achieve the target flux for any given composition, continuous material growth can result in an undesired composition gradient in the sample structure as observed in Figure 7.2a. To obtain the abrupt compositional and electrical interfaces required in the nBn structure, MBE growth was stopped to allow the effusion cells to stabilize at the desired temperature before resuming growth.

7.3.2 In-situ Spectroscopic Ellipsometry

In-situ spectroscopic ellipsometry (SE) was used to monitor the Cd composition and surface roughness of the HgCdTe layers. Figure 7.2a shows a calibration run of a LWIR nBn structure exhibiting large composition gradients at the interfaces due to the reaction time of the effusion cell flux. The SE Cd composition variation corresponds to the LWIR absorber layer (∼0.23), the barrier layer (∼0.44), and the cap layer (∼0.32). The SE composition and surface roughness of an optimized LWIR nBn detector is shown Figure 7.2b. Although an intentional compositional gradient is introduced between the buffer and absorber, the Cd composition exhibits little to no gradient at the nBn interfaces due to the calibrated growth technique.

Optical models were developed to fit the experimental SE data to determine parameters such as surface roughness and optical constants which are related to layer composition. Overall, the samples showed low levels of surface roughness over the entire run. Some optical oscillations were observed in the initial stages of the barrier and collector growth in the samples which are attributed to the change in composition dependent optical constants.

7.3.3 Optical and Structural FTIR Characterization

Ex-situ Fourier transform infrared spectroscopy (FTIR) transmission spectra measurements were taken at room temperature following each growth run to characterize the structural thickness and active layer composition and the interference fringes observed in the transmission spectra above the cutoff wavelength (defined as the value for which the absorption coefficient is 1000 cm^{-1}) were fitted to determine the HgCdTe layer thickness. Figure 7.3 shows the transmission spectra obtained for the first-iteration MWIR and LWIR nBn structures. The Cd composition of the absorber layer was back calculated from the cutoff wavelength using the expression by Hansen et al. [35]. The FTIR measurements were used to optimize the cell temperatures in

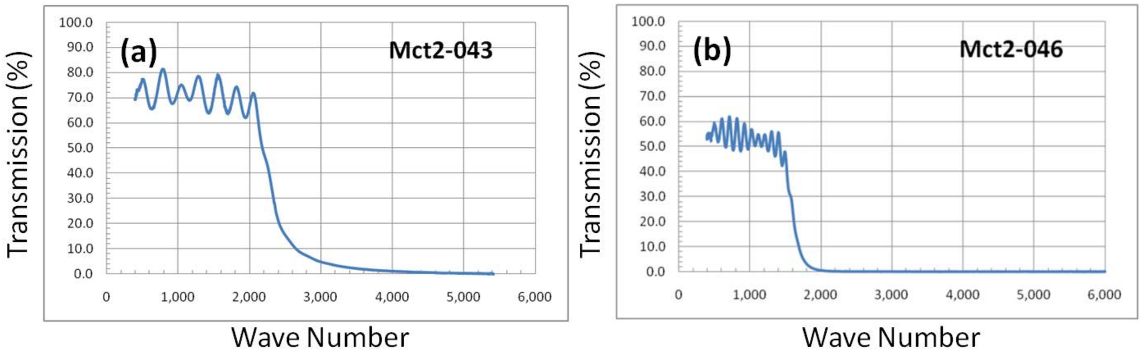

Figure 7.3: FTIR spectra measurements of first-iteration (a) MWIR (MCT2-043) and (b) LWIR (MCT2-046) nBn structures.

FTIR Characterization Data for HgCdTe nBn				
Sample	Cutoff Wavenumber	λ_{co}	FTIR (x_{abs})	FTIR Thickness (μm)
MCT2-043	2171.5	5.64	0.2855	5.52
MCT2-046	1637.3	8.72	0.2367	14.36
MCT2-086	2357.6	5.02	0.3025	8.94

Table 7.1: Surface morphology data for first-iteration MWIR (MCT2-043) and LWIR (MCT2-046) and second-iteration MWIR (MCT2-086) HgCdTe nBn epitaxial structures.

subsequent growth iterations. Table 7.1 lists the optical and structural properties of the nBn layer samples measured using FTIR spectroscopy.

7.3.4 Surface Morphology

Following growth, the HgCdTe nBn sample surfaces were examined closely for defects. One of the major challenges of HgCdTe MBE growth is controlling the density of lattice dislocations and macroscopic defects which can affect IR device performance. The defect densities can be reduced and controlled by optimizing growth conditions. Surface morphology characterization of the samples was performed using a Normaski microscope. The Normarski microscope is an interference microscope which employs a polarization differential technique to create a pseudo-3D image effect emphasizing the details of a sample's surface.

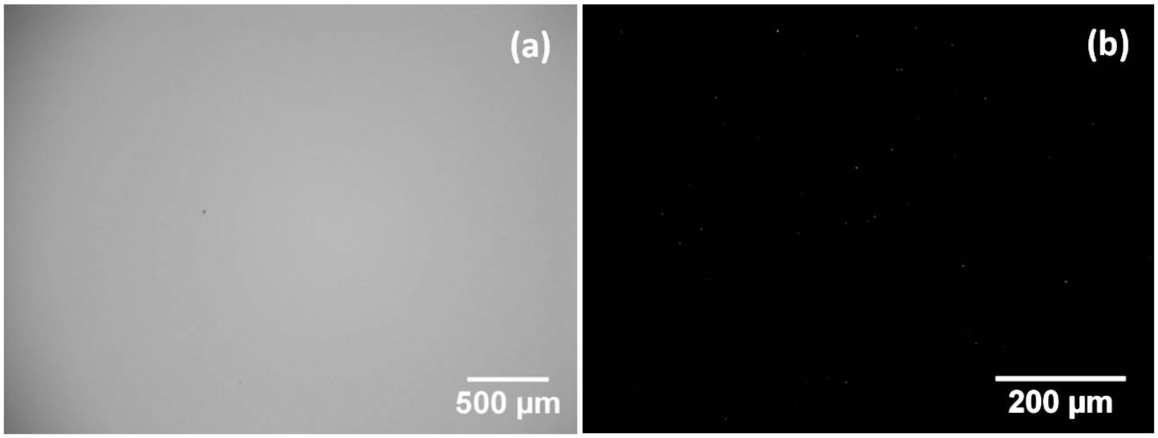

Figure 7.4: Nomarski microscope image of first-iteration MWIR (MCT2-043) HgCdTe nBn sample under (a) 50x (bright field) and (b) 200x (dark field) magnifications.

Surface Morphology Data			
Sample	EPD (cm^{-2})	Defects >2 μm (cm^{-2})	Microdefects <2 μm (cm^{-2})
MCT2-043	3.1×10^4	1.66×10^2	2.6×10^3
MCT2-046	1.9×10^4	8.13×10^2	7.52×10^2
MCT2-086	7.24×10^4	5.06×10^2	3.07×10^3

Table 7.2: Surface morphology data for first-iteration MWIR (MCT2-043) and LWIR (MCT2-046) and second-iteration MWIR (MCT2-086) HgCdTe nBn epitaxial structures.

The nBn samples were examined at 50x and 200x magnifications as shown in Figures 7.4 and 7.5. Surface defects were counted from microscope images taken over various areas of the sample and averaged to determine the overall defect density. The defects were categorized according to size. Micro-defects are defects smaller than 2 μm and are counted from 200x magnification dark field images. Defects larger than 2 μm are called micro-voids and are counted from 50x bright field images. EPD measurements were also performed to examine dislocations in the samples. Typical EPD values for HgCdTe layers grown on CdZnTe fall in the 10^4 cm^{-2} range. The averaged defect densities are summarized in Table 7.2.

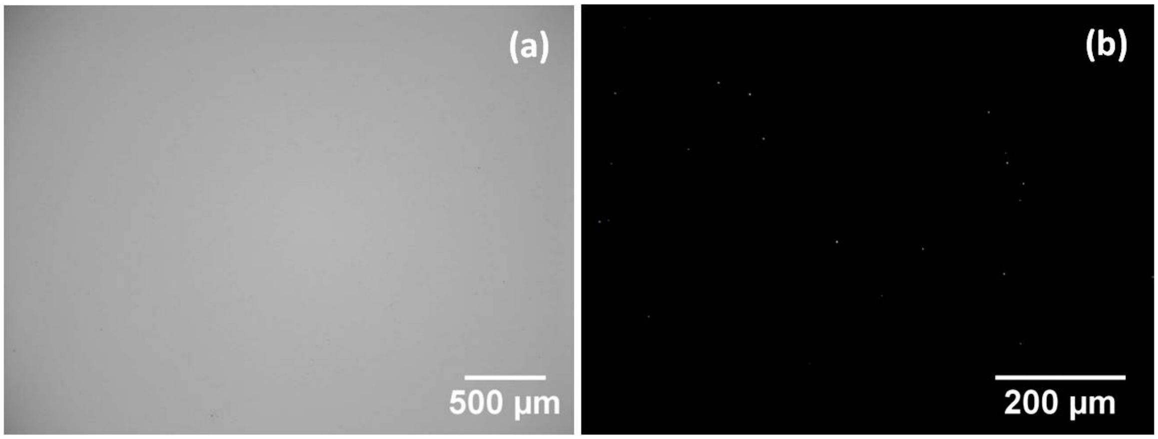

Figure 7.5: Nomarski microscope image of first-iteration LWIR (MCT2-046) HgCdTe nBn sample under (a) 50x (bright field) and (b) 200x (dark field) magnifications.

77 K Hall Measurements (n_{abs})			
Sample	Type	Carrier Concentration (cm^{-3})	Mobility (cm^2/Vs)
MCT2-043	N	7.28×10^{14}	3.04×10^{4}
MCT2-046	N	5.58×10^{14}	8.49×10^{4}
MCT2-086	N	3.33×10^{14}	1.31×10^{4}

Table 7.3: 77 K Hall measurements of first-iteration MWIR (MCT2-043) and LWIR (MCT2-046) and second-iteration MWIR (MCT2-086) HgCdTe nBn absorber layers.

7.3.5 Electrical Properties

Hall measurements were performed on the absorber layer of the nBn layer samples using the standard Van-Der Pauw method. The cap and barrier layers of the nBn samples were removed using a bromine/methanol etch to expose the underlying absorber layer. Measurements of carrier concentrations and electron mobilities taken at 77 K for first-iteration samples are listed in Table 7.3. The nBn absorber layer concentrations are in the mid-10^{14} cm^{-3}.

7.4 Experiment Methodology: Single Element nBn Devices

7.4.1 Device Fabrication

The MWIR and LWIR nBn device structures are loosely based on optimized material and geometric parameters from the simulation study described in the previous chapter [94]. The parameters of the first- and second-iteration nBn layers are listed in Tables 7.4 and 7.5. Prior to processing, the samples were annealed under Hg overpressure at 202°C for 15.5 hours (MCT2-043, MCT2-046) and 203°C for 15 hours (MCT2-086) to eliminate Hg vacancies present after growth. In addition to the *in situ* SE measurements recorded during material growth, SIMS measurements were used to verify the compositional profiles of the nBn structures. The SIMS measurements were outsourced to Evans Analytical Group. The SIMS profiles for similar first-iteration layer structures are shown with slightly modified vacancy anneal conditions in Figure 7.6, and second-iteration layers structures are shown in Figure 7.7. A wide bandgap CdTe/HgCdTe buffer layer is present between the substrate and the absorber. The devices were also grown with a thin CdTe termination layer, later removed during fabrication.

The device fabrication process is shown in Figure 7.8. Plasma etching was used to access the absorber layer just past the barrier, and electrical contacts (100 nm In) to the HgCdTe and pad metals (1st iteration: 20 nm/300 nm Ti/Au, 2nd iteration: 20 nm/400 nm Ti/Au) were fabricated using conventional metallization and lift-off processes. ZnS was deposited by evaporation between the pad metal and HgCdTe for surface passivation and electrical insulation. For practical purposes, the devices were fabricated in planar-mesa and mesa configurations using the same photomask. The configurations are differentiated by the proximity of the mesa delineation features to the electrical contacts as shown in Figure 7.9. Electrical measurements were performed by varying the voltage at the top contact terminal (n_{cap}) relative to the

MWIR (MCT2-043) and LWIR (MCT2-046) nBn Structural Parameters: 1st Iteration			
Layer	$Hg_{1-x}Cd_xTe$	Thickness	In Concentration (N_D)
n_{cap}	x = 0.33 (M)	0.16 μm (M)	7×10^{14} cm^{-3} (M)
	x = 0.31 (L)	1.0 μm (L)	5×10^{15} cm^{-3} (L)
B	x = 0.64 (M)	0.14 μm (M)	2×10^{15} (M)
	x = 0.45 (L)	0.15 μm (L)	7×10^{14} cm^{-3} (L)
n_{abs}	x = 0.30 (M)	2.75 μm (M)	1×10^{14} cm^{-3}
	x = 0.23 (L)	10.0 μm (L)	

Table 7.4: Structural parameters for first-iteration MWIR (MCT2-043) and LWIR (MCT2-046) HgCdTe nBn layers.

MWIR (MCT2-086) nBn Structural Parameters: 2nd Iteration			
Layer	$Hg_{1-x}Cd_xTe$	Thickness	In Concentration (N_D)
n_{cap}	x = 0.4	1.03 μm	5×10^{15} cm^{-3}
B	x = 0.6	0.31 μm	2×10^{13} cm^{-3}
n_{abs}	x = 0.29	5.08 μm	6×10^{13} cm^{-3}

Table 7.5: Structural parameters for second-iteration MWIR (MCT2-086) HgCdTe nBn layers.

absorber terminal (n_{abs}). The dark current-voltage characteristics were measured using a Janis cryostat probe system cooled with LN_2. The devices were packaged and mounted in an LN_2 cooled dewar for all front-side illumination optical measurements.

7.4.2 Device Modeling of MBE Grown nBn Structures

Device simulations incorporating the measured nBn parameters were performed using the physics-based 1-D numerical model described in Chapter III. The calculated energy band diagrams for the first-iteration MWIR nBn layer structure (MCT2-043) along the growth direction are shown in Figure 7.14 under equilibrium and reverse bias conditions. Under low bias conditions near equilibrium, the barrier layer inhibits current flow between the contact and absorber terminals. With increasing reverse bias, the band diagram is inverted to provide a profile that resembles a conventional *p*-*n* heterojunction. In the inverted configuration, the dark current is limited to

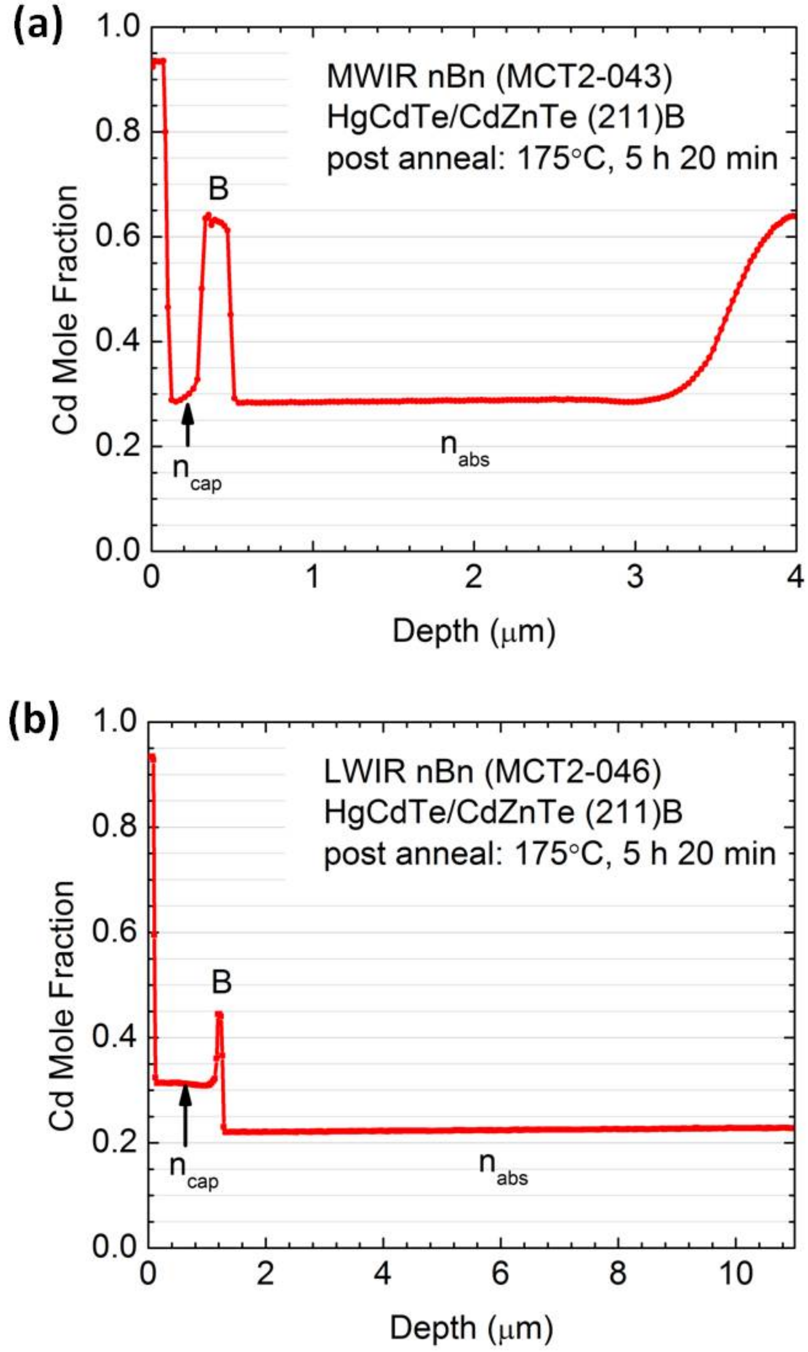

Figure 7.6: SIMS Cd composition profile of first-iteration (a) MWIR (MCT2-043) and (b) LWIR (MCT2-046) HgCdTe nBn layers after a vacancy annihilation anneal at 175°C for 5 h 20 min.

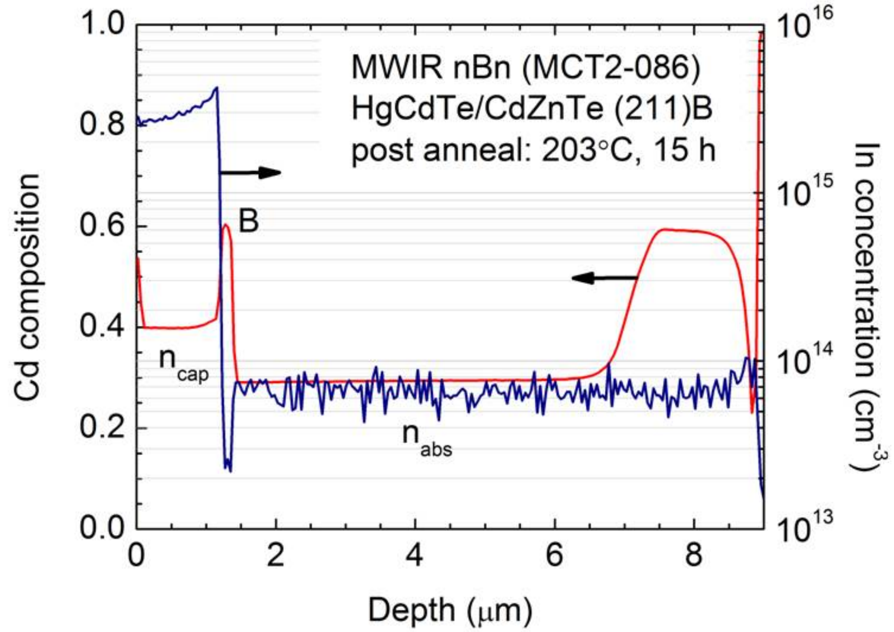

Figure 7.7: SIMS Cd composition and In concentration profiles of second-iteration MWIR (MCT2-086) HgCdTe nBn layers after a vacancy annihilation anneal at 203°C for 15 h.

thermal generation in the absorber layer for the ideal case, while photocurrent may be produced by the collection of photogenerated holes in the absorber. The dark current is expected to saturate under increasing reverse bias (a defining characteristic of the nBn device), barring any contributions from non-ideal effects such as tunneling. It is noted that in the first-iteration MWIR nBn device, the depletion region extends far into the absorber layer as a result of the high doping concentration in the barrier layer. This design is not necessarily ideal, as SRH G-R processes can dominate at lower temperatures, increasing the overall dark current. Figure 7.15 shows the calculated band diagrams based on second-iteration MWIR nBn structural parameters (MCT2-086) along the growth direction.

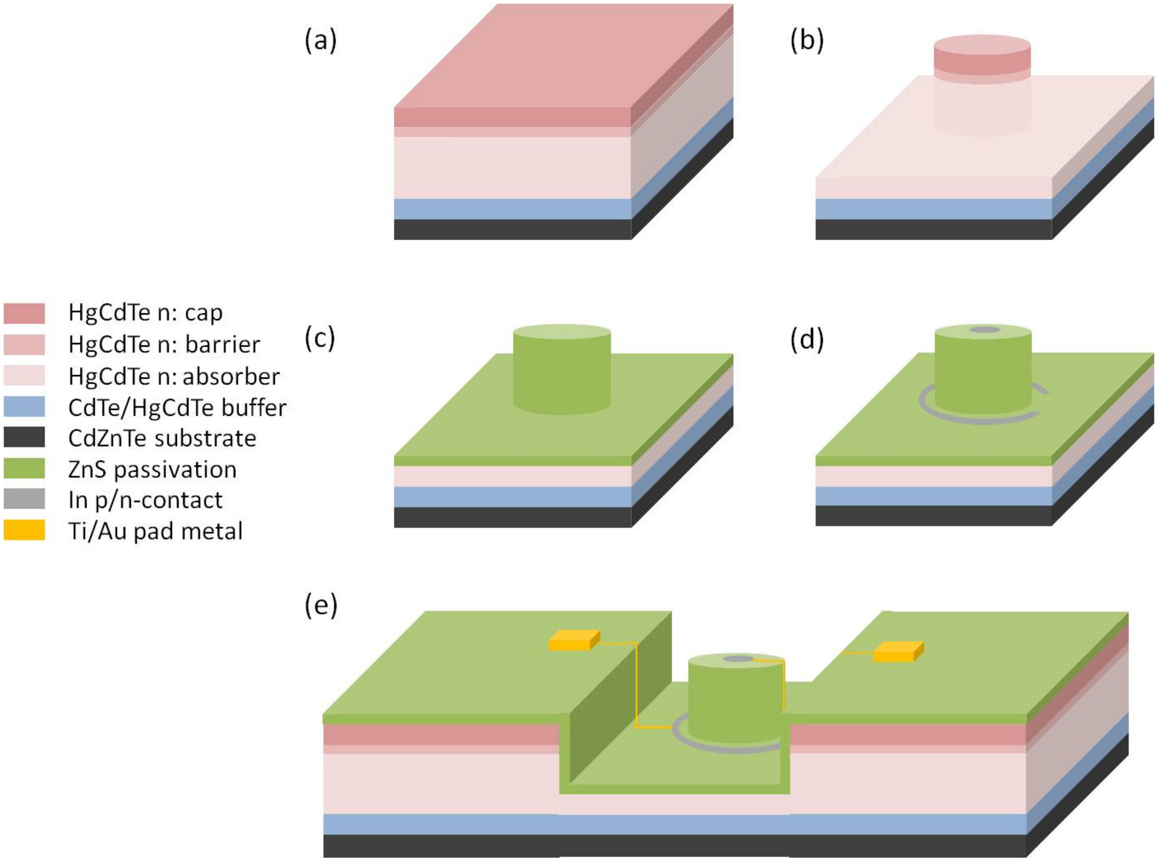

Figure 7.8: Schematic illustration of nBn device fabrication process.

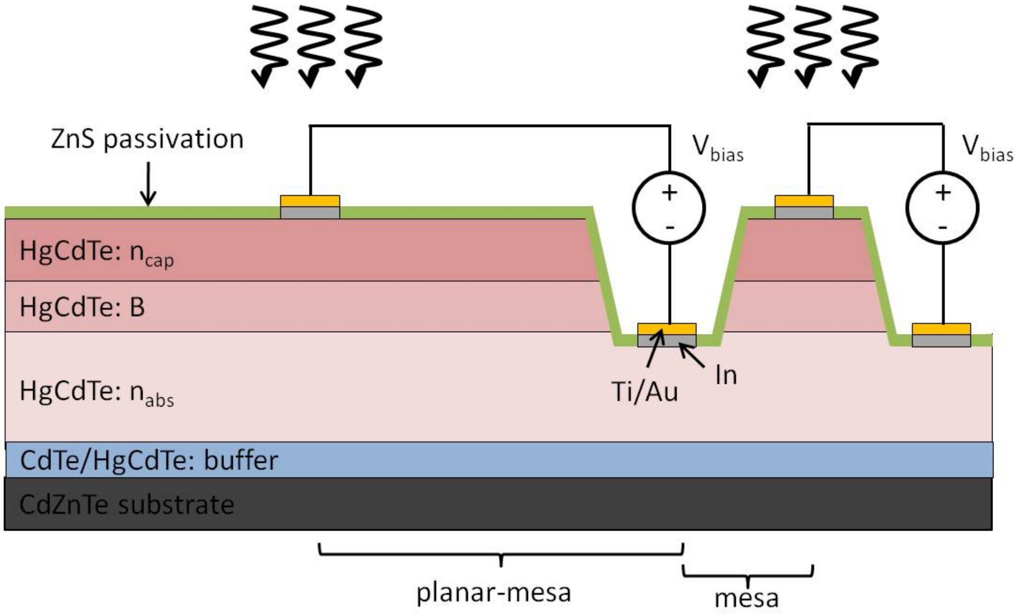

Figure 7.9: Cross-sectional view of planar-mesa and mesa HgCdTe nBn device layer structure and test set-up.

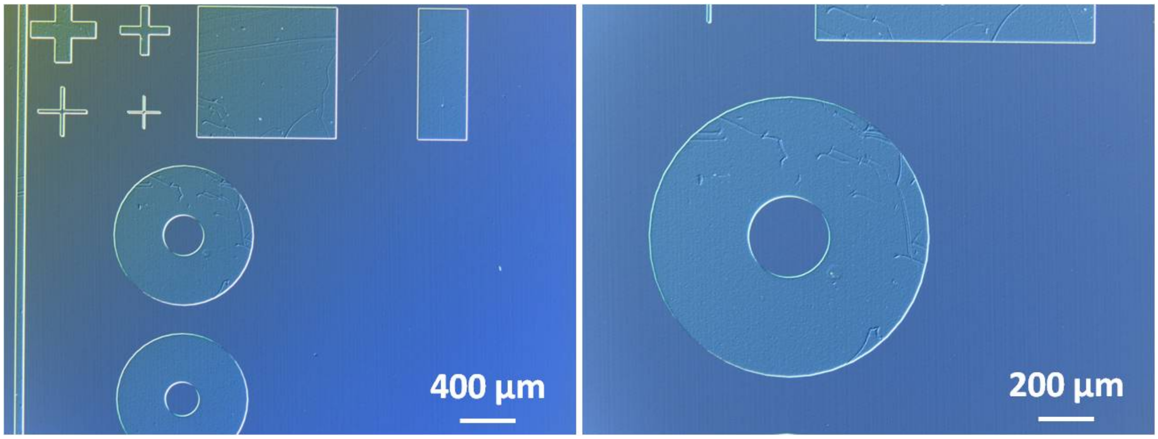

Figure 7.10: First-iteration MWIR (MCT2-043) HgCdTe nBn devices under different magnifications after mesa delineation by plasma etching. Mesa devices etched 0.774 μm from contact to absorber layer.

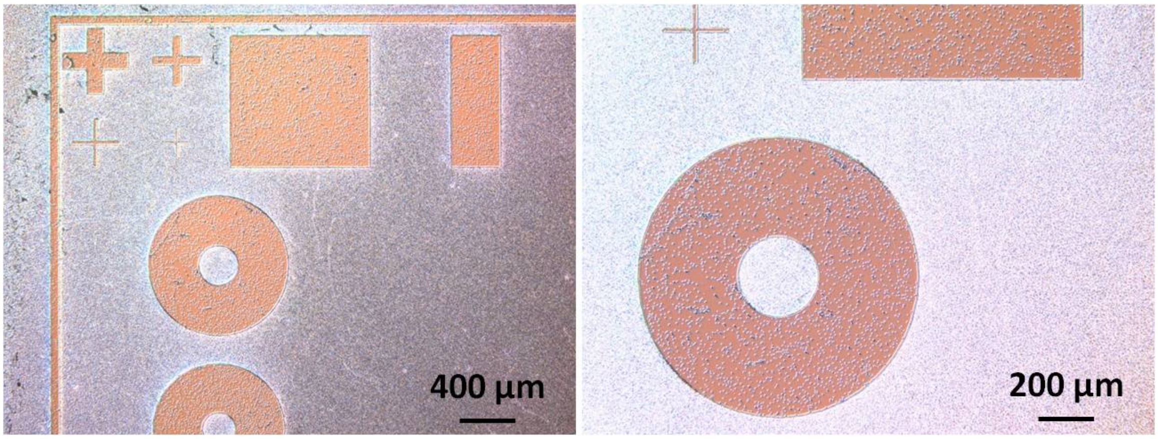

Figure 7.11: First-iteration MWIR (MCT2-043) HgCdTe nBn devices under different magnifications after 400 nm ZnS passivation.

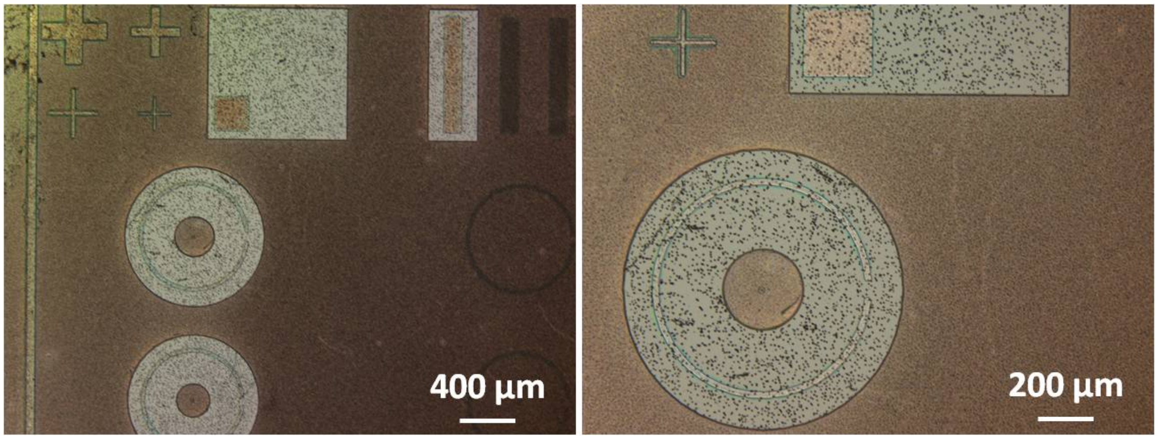

Figure 7.12: First-iteration MWIR (MCT2-043) HgCdTe nBn devices under different magnifications after 100 nm In contact evaporation.

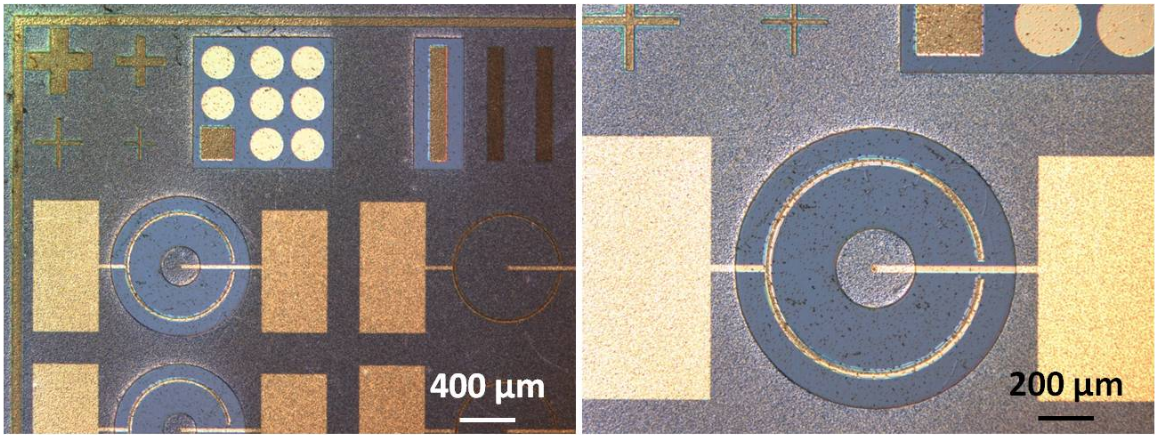

Figure 7.13: First-iteration MWIR (MCT2-043) HgCdTe nBn devices under different magnifications after 20 nm Ti/300 nm Au pad metal deposition.

7.5 Results and Discussion

7.5.1 First-iteration Prototypes

The measured dark I-V characteristics of a first-iteration planar-mesa MWIR nBn device for varying temperatures are shown in Figure 7.16. The unique dark current ‘turn-on’ feature predicted for the nBn device [94] is present in the experimental data at reverse bias values in the range of -0.5 V to -1.0 V. As described in Chapter VI, the ‘turn-on’ bias range indicates the proper bandedge alignment of the contact and absorber regions, enabling the collection of minority carrier holes from the absorber layer. At higher reverse biases, the saturation current slowly increases, eventually resulting in breakdown. The breakdown behavior becomes more apparent at higher operating temperatures where the saturation current is dominated by thermally generated carriers, and the decrease in the barrier layer bandgap reduces the suppression of majority carrier current contributions. The turn-on voltage also appears to shift to higher biases with increasing temperature as the bandedge energies of the material layers change, affecting the bias required to minimize the valence band barrier.

Higher dark current is observed in the first-iteration planar-mesa LWIR device due to increased thermal generation in narrow bandgap materials as shown in Figure

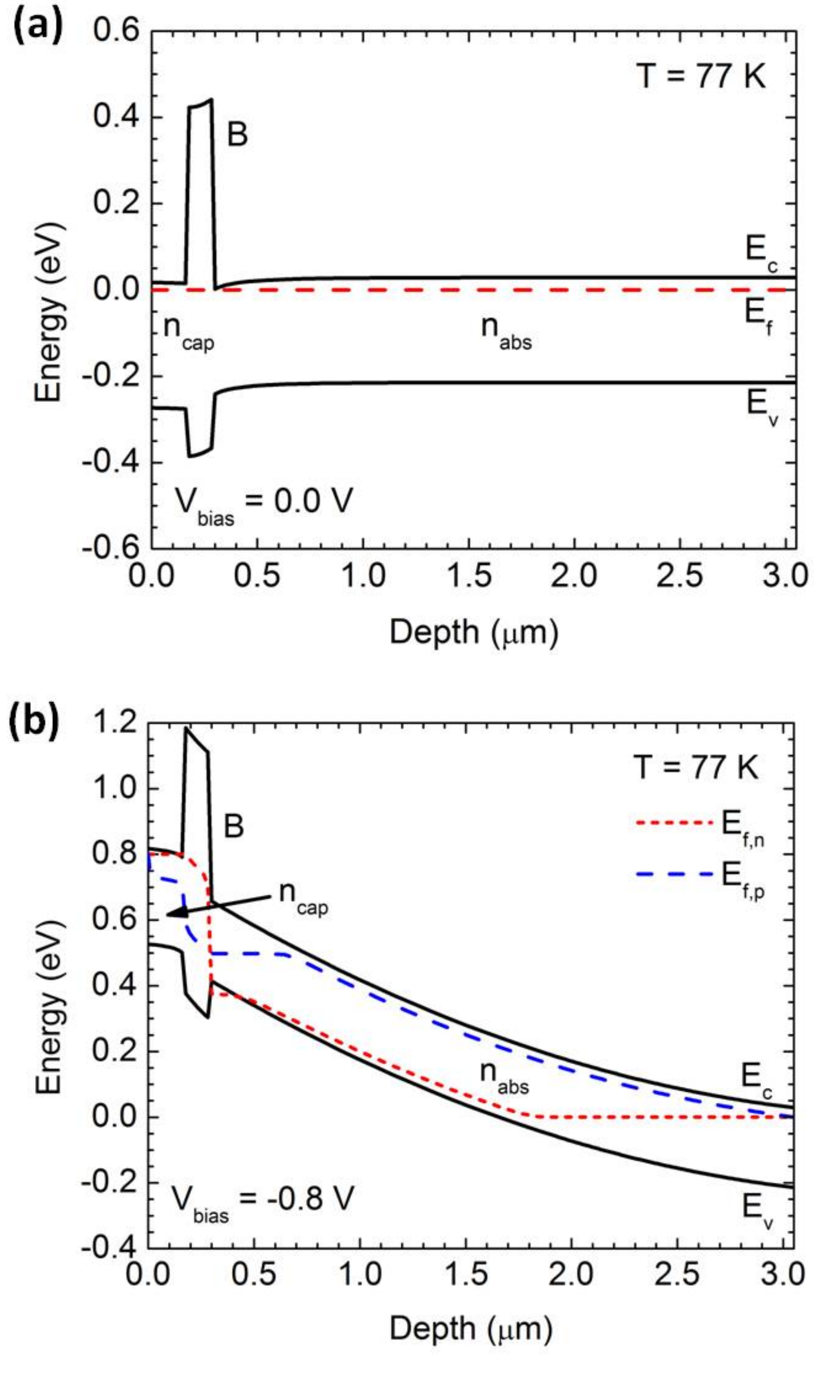

Figure 7.14: Calculated band diagrams based on first-iteration MWIR (MCT2-043) HgCdTe nBn structural parameters (a) at equilibrium and (b) under reverse bias conditions.

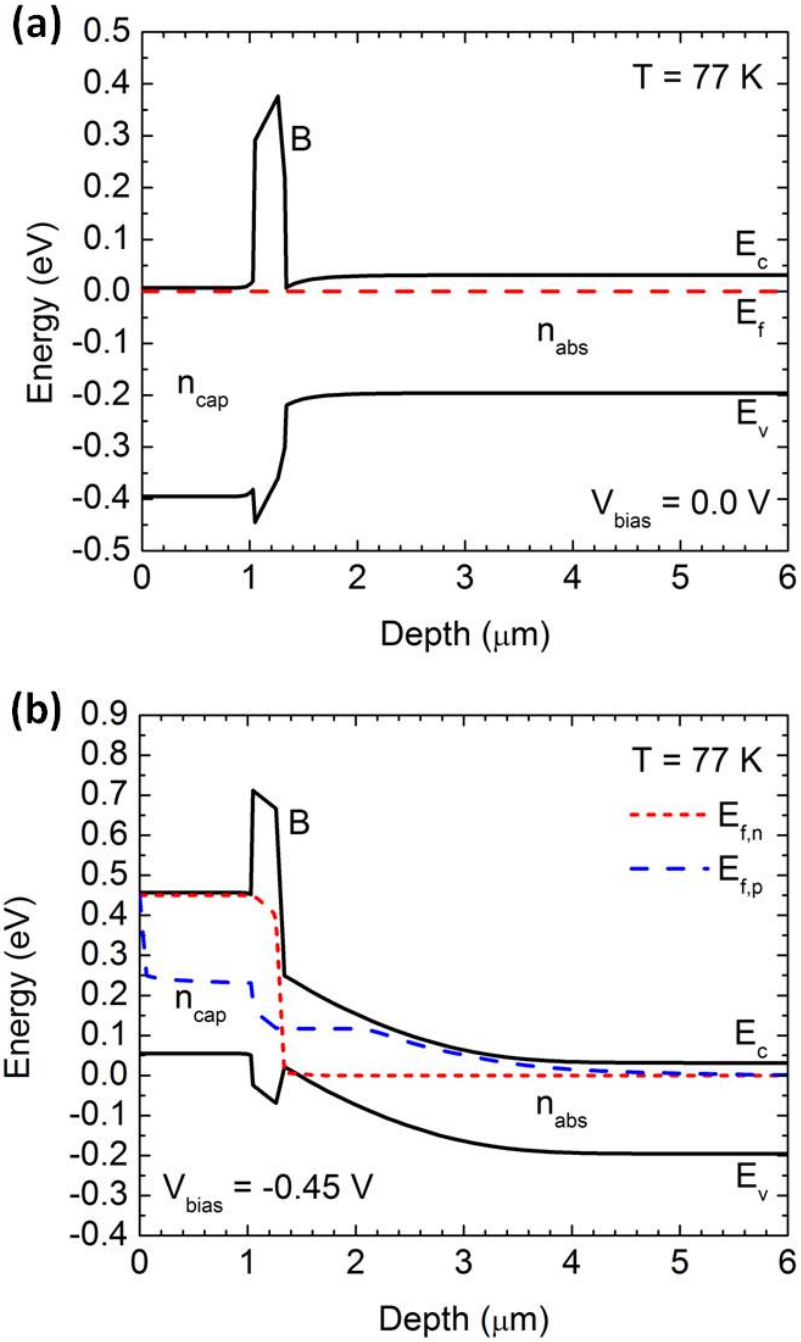

Figure 7.15: Calculated band diagrams based on second-iteration MWIR (MCT2-086) HgCdTe nBn device structural parameters (a) at equilibrium and (b) under reverse bias conditions. Barrier is undoped.

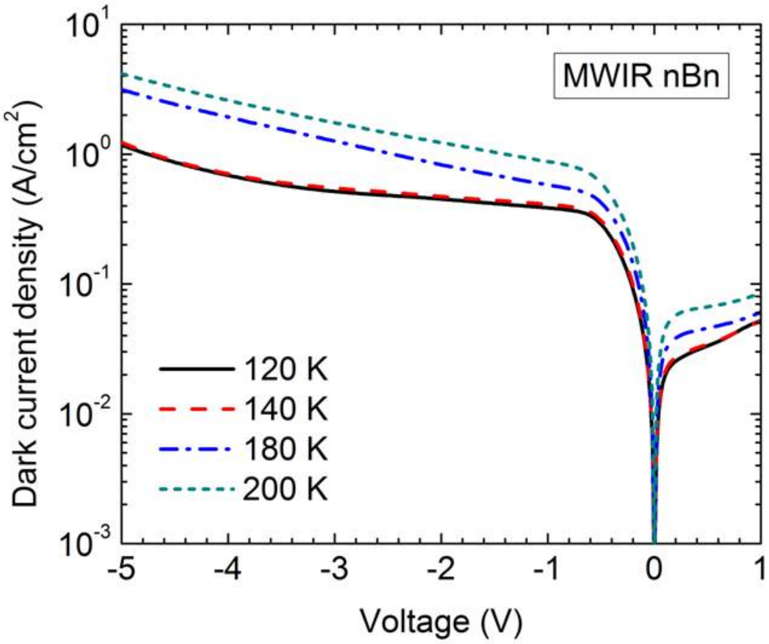

Figure 7.16: Measured current-voltage characteristics of MCT2-043 planar-mesa MWIR HgCdTe nBn device at varying temperatures.

7.20. At 77 K, a higher turn-on voltage range is observed in the MWIR device (-0.5 V to -1 V) compared to the LWIR device (-0.2 V to -0.6 V) due to the difference in the barrier layer band-edge.

The measured and calculated dark current density J_{dark} values at -0.8 V bias for the planar-mesa MWIR nBn device are shown in Figure 7.17 for a range of temperatures. The simulated I-V curve accounts for the layer doping concentrations, compositional profile, device geometry, and assumes an intrinsic trap level with SRH lifetimes of $\tau_{n0} = 10$ μs and $\tau_{p0} = 1$ μs. The -0.8 V reverse bias value was selected to ensure the J_{dark} values correspond to the saturation region. J_{dark} values for temperatures above 180 K correspond to expected trends with the current rising due to increased thermal generation. The saturation dark current density J_{dark} at 180 K at -0.8 V reverse bias is -0.54 A/cm^2, which is comparable to the calculations for a similar structure (-0.31 A/cm^2). Above 180 K, the overall J_{dark} values are dominated by Auger generation. At temperatures above 250 K, the measured J_{dark} is lower than the calculated values. This deviation may be caused by the possible existence of unintentional barriers at the heterojunction interfaces. At 180 K and below, the experimental J_{dark} saturates; this behavior is attributed to some form of perimeter leakage current. Moreover, the J_{dark} for varying planar-mesa device areas exhibits a strong dependence on the perimeter-over-area ratio as shown in the inset of Figure 7.17, suggesting that sidewall perimeter leakage is a limiting mechanism in these devices [95–97].

The contribution of the perimeter leakage current increases with decreasing device size. If the surface leakage current is assumed to be proportional to the diode perimeter P, the total device current I_{diode} (A) can be expressed as [98]

$$\frac{I_{diode}}{A} = J_A + \frac{P}{A} J_P \tag{7.1}$$

where A is the cross-sectional area (cm^2), J_A is the leakage current density proportional to the device area (A/cm^2), and J_P is the perimeter leakage density per unit length (A/cm). From this expression, it follows that the total device current depends linearly on the perimeter-over-area ratio if corner and parasitic components can be neglected. While the J_{dark} values of the planar-mesa device do not strictly exhibit a linear dependence, a distinct proportional increase is nonetheless observed.

For a better understanding of the issue, measured I-V characteristics of several mesa MWIR HgCdTe nBn devices with varying diode diameters shown in Figure 7.18 were also examined. Like the planar-mesa diodes, the J_{dark} of mesa devices exhibit a strong dependence on the perimeter over area ratio as illustrated in Figure 7.18 (inset). The I-V characteristics of the mesa devices reveal an interesting behavior; they are similar to those observed in the planar diode with the exception of a notable inflection at the turn-on voltage in the otherwise monotonically increasing reverse bias current. The turn-on bias range is very similar to the planar-mesa MWIR nBn

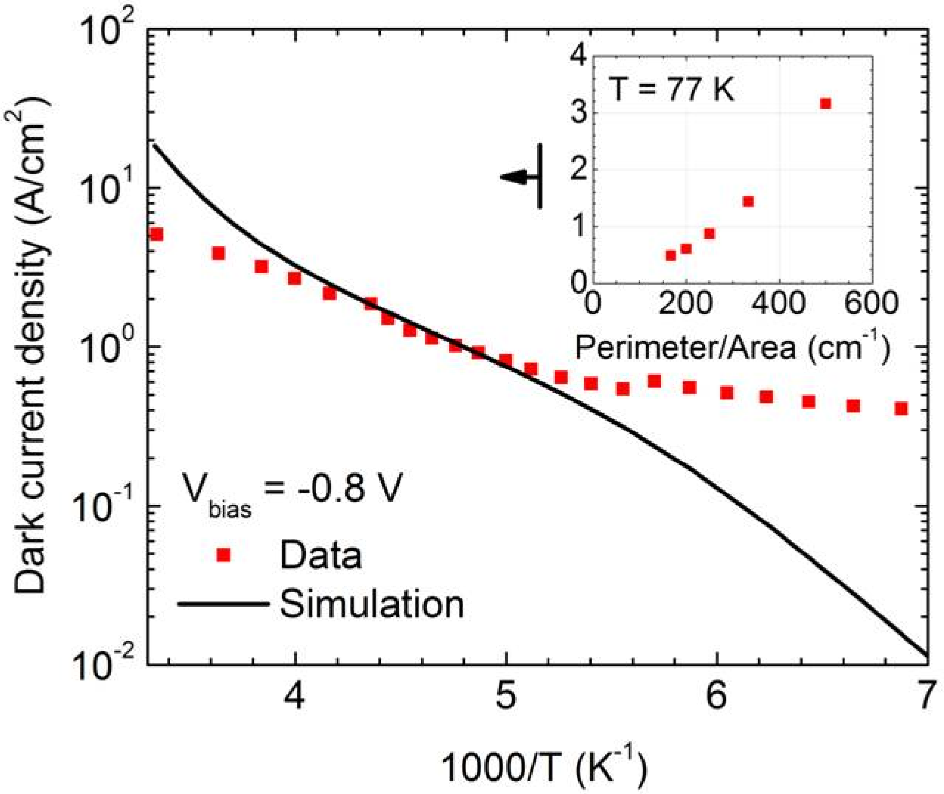

Figure 7.17: Measured and calculated dark current density for MCT2-043 planar-mesa MWIR nBn detector with effective area 4.52×10^{-4} cm^2 biased at -0.8 V for varying temperatures. (Inset) Measured J_{dark} as a function of perimeter-over-area ratio at 77 K for same bias condition.

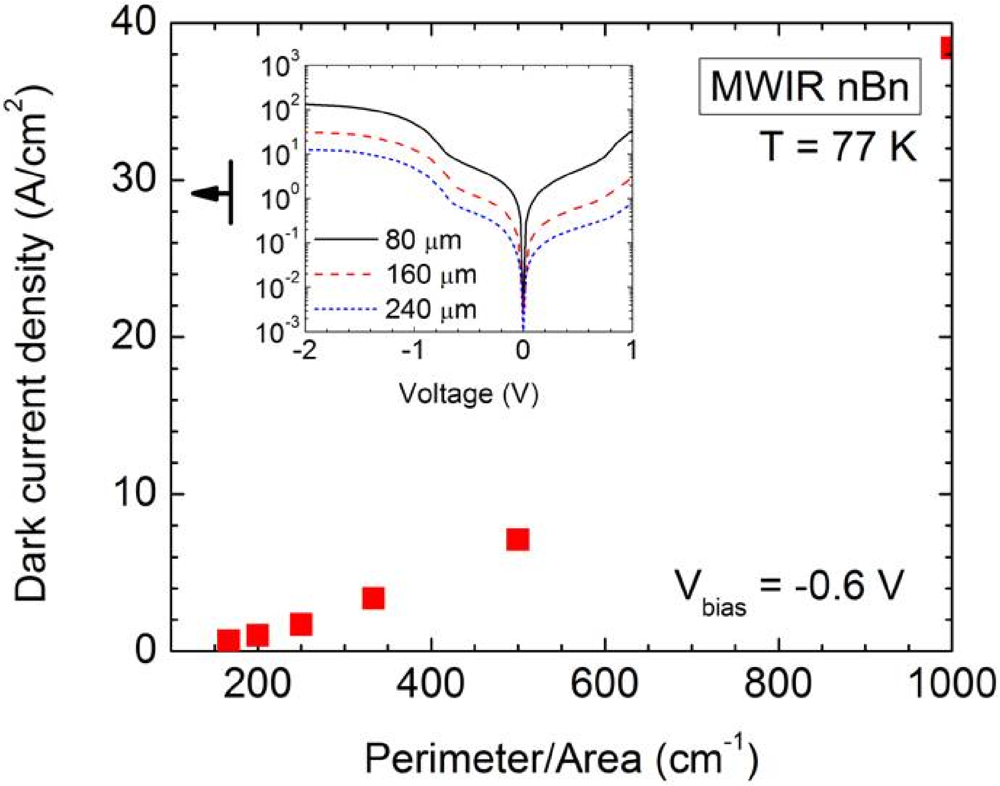

Figure 7.18: Measured MCT2-043 mesa MWIR HgCdTe nBn J_{dark} values under -0.6 V reverse bias as a function of the perimeter over area ratio. (Inset) current-voltage characteristics for devices with varying diameters.

device, and the J_{dark} values of planar-mesa and mesa detectors are roughly comparable between 0 and -0.6 V as observed in Figure 7.19. Just beyond the turn-on voltage, the saturation current density in the mesa device increases abruptly. This change in J_{dark} appears to be bias dependent, suggesting the surface effects are influenced by the barrier layer.

It is possible there are separate perimeter leakage effects dominating the dark current at different bias regions. These mechanisms are 1) band bending at the sidewall due to charge accumulation and 2) carrier generation via sidewall surface states. The use of ZnS passivation typically results in fixed positive charges at the HgCdTe interface [99–101], leading to accumulation at the *n*-type material surface. This effect

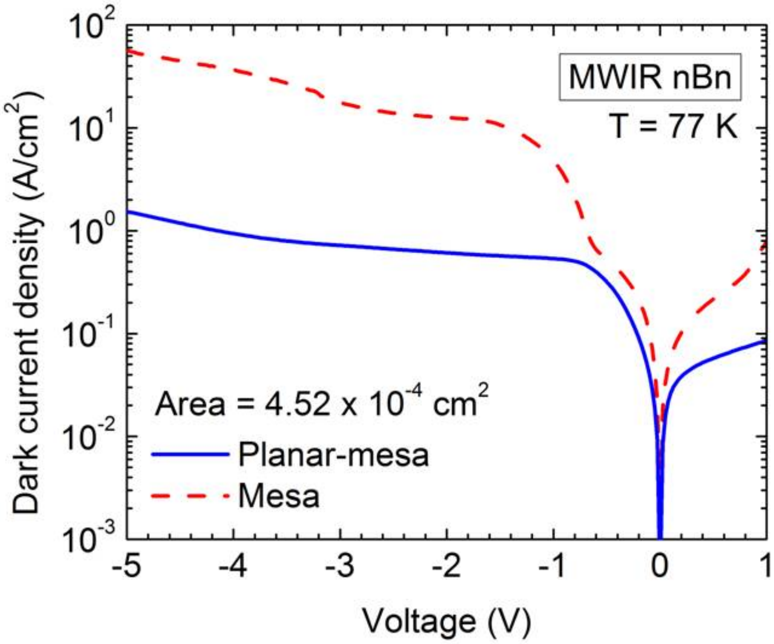

Figure 7.19: Current-voltage characteristics for MCT2-043 planar-mesa and mesa MWIR HgCdTe nBn devices with effective area 4.52×10^{-4} cm^2.

may cause band bending which would reduce ΔE_c along the sidewalls, and provide a conducting path for majority carriers as illustrated in Figure 6.8. Moreover, damage caused by etching into the absorber for contact placement may create trap states near the sidewalls, affecting G-R processes in the narrow bandgap material. Thus, at voltages below the turn-on bias, perimeter leakage due to accumulation-induced band bending (and reduced ΔE_c) may dominate the current behavior. Beyond the turn-on bias where ΔE_v is minimized, minority carriers generated by intermediate states near the surface of the exposed absorber then become the limiting factor. The second mechanism would be most pronounced in the mesa structures where the absorber contact is very close to the cap contact, further facilitating conduction along the device perimeter. The perimeter leakage issue may be addressed by improving sidewall passivation quality and/or minimizing exposure of the absorber layer by reducing the etch depth for contact placement or adopting a backside contact configuration.

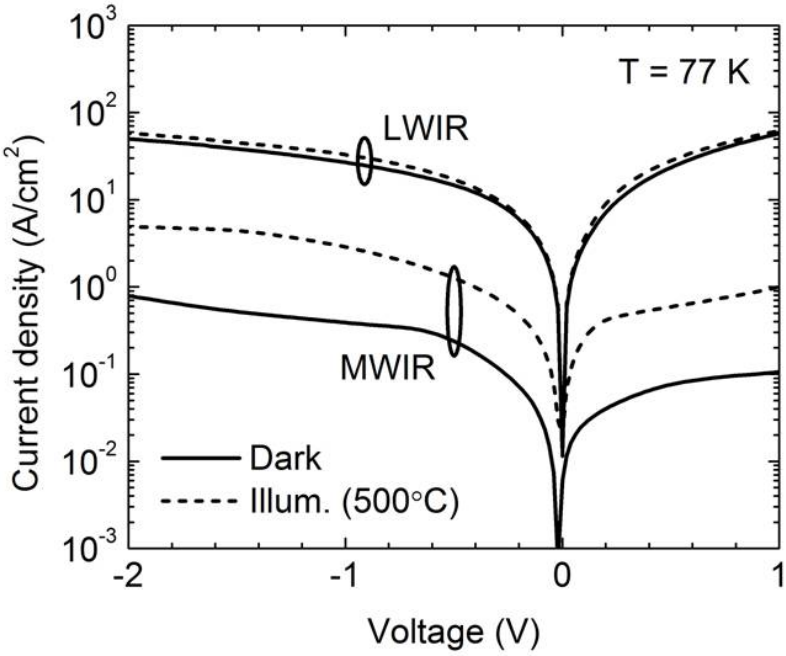

Figure 7.20: Current-voltage characteristics of planar-mesa MWIR (MCT2-043) and LWIR (MCT2-046) HgCdTe nBn devices measured under dark and unfiltered 500°C blackbody illumination conditions.

Under blackbody illumination, the planar-mesa MWIR nBn device exhibits a greater optical response compared to the LWIR device. The I-V characteristics in Figure 7.20 illustrate the photoresponse of both planar-mesa MWIR and LWIR nBn devices under unfiltered 500°C blackbody illumination at 77 K. The results indicate the MWIR device with lower J_{dark} is more sensitive to illumination, exhibiting a larger contrast between light and dark I-V characteristics, while the LWIR nBn dark current is dominated by significantly higher leakage current. It is noted that a slight increase in dark current density is observed in these measurements due to additional leakage currents associated with surface defects incurred during sample packaging. Relative response measurements taken at varying reverse biases for the planar-mesa MWIR nBn device are shown in Figure 7.21. The optical data suggest a bias-dependent photoresponse, as expected from the I-V behavior. Beyond a reverse bias of -0.8 V, the photoresponse saturates, indicating a change in the valence band barrier with increasing bias. The measurements exhibit a consistent cutoff wavelength near 5.7 μm, corresponding to the band-edge of the $Hg_{0.70}Cd_{0.30}Te$ absorber layer. The cut-on behavior near 3.2 μm is attributed to a component of test set-up. Due to the low photoresponse, spectral response measurements were not obtained for the planar-mesa LWIR nBn device. The estimated QE based on measured photocurrent under blackbody illumination relative to the photon flux from the source integrated over the nBn detector spectral response suggests values that would exceed 100%. These estimations indicate carrier collection is not an issue, and the anomalous values are attributed to the lateral collection within the device. Large lateral collection lengths have been similarly reported for nBn devices based on III-V materials [88]. Accurate experimental QE data will require well-passivated mesa delineated devices and is an important consideration for the future development of these devices. A numerical simulation was performed to calculate the internal QE of the MCT2-043 MWIR nBn detector. An internal QE of approximately 66% at a wavelength of 5 μm is predicted

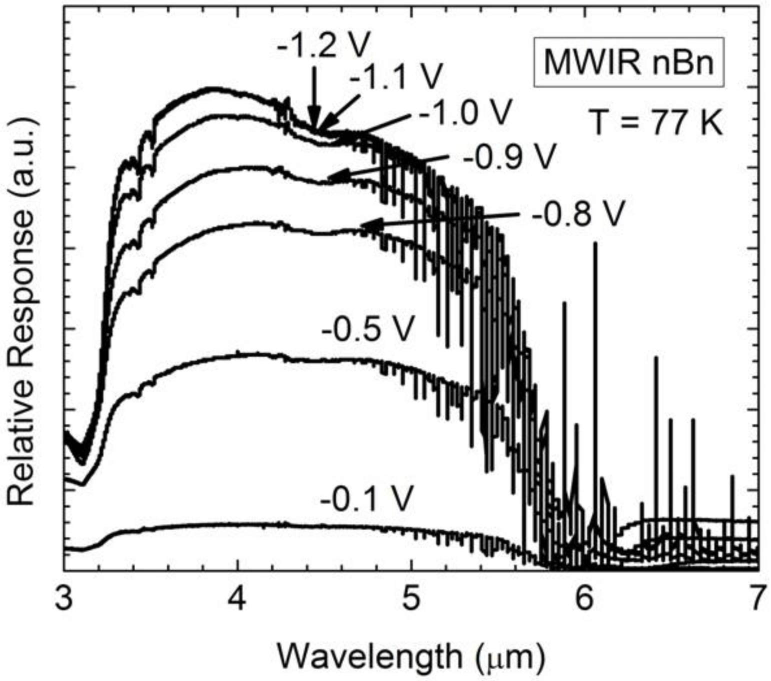

Figure 7.21: Measured spectral response measurements at varying reverse biases for MCT2-043 planar-mesa MWIR HgCdTe nBn device.

at a reverse bias of -0.8 V, verifying efficient collection of photogenerated carriers.

7.5.2 Second-iteration Prototypes

Several modifications were made to the MWIR nBn structure for a second-iteration prototype. Table 7.5 lists the structural parameters of the MBE-grown MWIR HgCdTe nBn device, with the main modifications being the doping concentrations in each layer, namely the undoped barrier layer, the increased barrier thickness, and the increased n_{cap} layer Cd composition. The I-V characteristic of a mesa MWIR nBn device with active area 3.14×10^{-4} cm^2 at 77 K is shown in Figure 7.22a. The dark current turn-on feature is observed in the experimental data at a reverse bias value around -0.2 V. This turn-on voltage is lower than that observed in the first-iteration planar-mesa and mesa MWIR nBn devices at the same temperature and can be attributed to the reduction in ΔE_v. The saturation J_{dark} is stable between -0.2 V and -1.0 V and is the region of interest for device operation. The saturation J_{dark} at 77 K at -0.5 V reverse bias is -3.74×10^{-6} A/cm^2 compared to the calculated value of -8.08×10^{-9}A/cm^2 for a similar structure with an undoped barrier (Figure 7.15). The measured J_{dark} value is about five orders of magnitude lower than values observed in comparable first-iteration planar-mesa (J_{dark}(-0.5 V) = -0.38 A/cm^2) and mesa devices (J_{dark}(-0.5 V) = -0.81 A/cm^2). The 77 K wavelength-dependent relative response measurement shown in Figure 7.22b exhibits a cutoff wavelength of 5.2 μm, consistent with the band-edge of the $Hg_{0.71}Cd_{0.29}Te$ absorber layer. Further optimization of the nBn structural parameters and processing steps in future work are expected to improve the overall J_{dark} and photoresponse of the device.

It is noted that the measured dark current densities of the nBn devices are several orders of magnitude higher than those given by “Rule 07”, a common metric for comparing HgCdTe IR detector dark current [67]. As the inset of Figure 7.17 and Figure 7.18 show, the HgCdTe nBn devices are clearly dominated by perimeter leakage and non-ideal effects rather than intrinsic G-R mechanisms. Further study of devices with improved surface passivation is warranted, and it may also be necessary to identify any issues unique to the nBn structure including mechanisms such as trap assisted tunneling through the barrier layer before accurate comparisons to Rule 07 can be made. These studies are reserved for future work.

7.6 Conclusion

In summary, the concept of the HgCdTe nBn detector was experimentally demonstrated in this study. The results of fabricated single element MWIR and LWIR nBn detectors show electrical and optical characteristics corresponding to the device behavior predicted in Chapter VI. The measured I-V data of the planar-mesa and mesa HgCdTe nBn devices clearly illustrate barrier influenced behavior and follow tem-

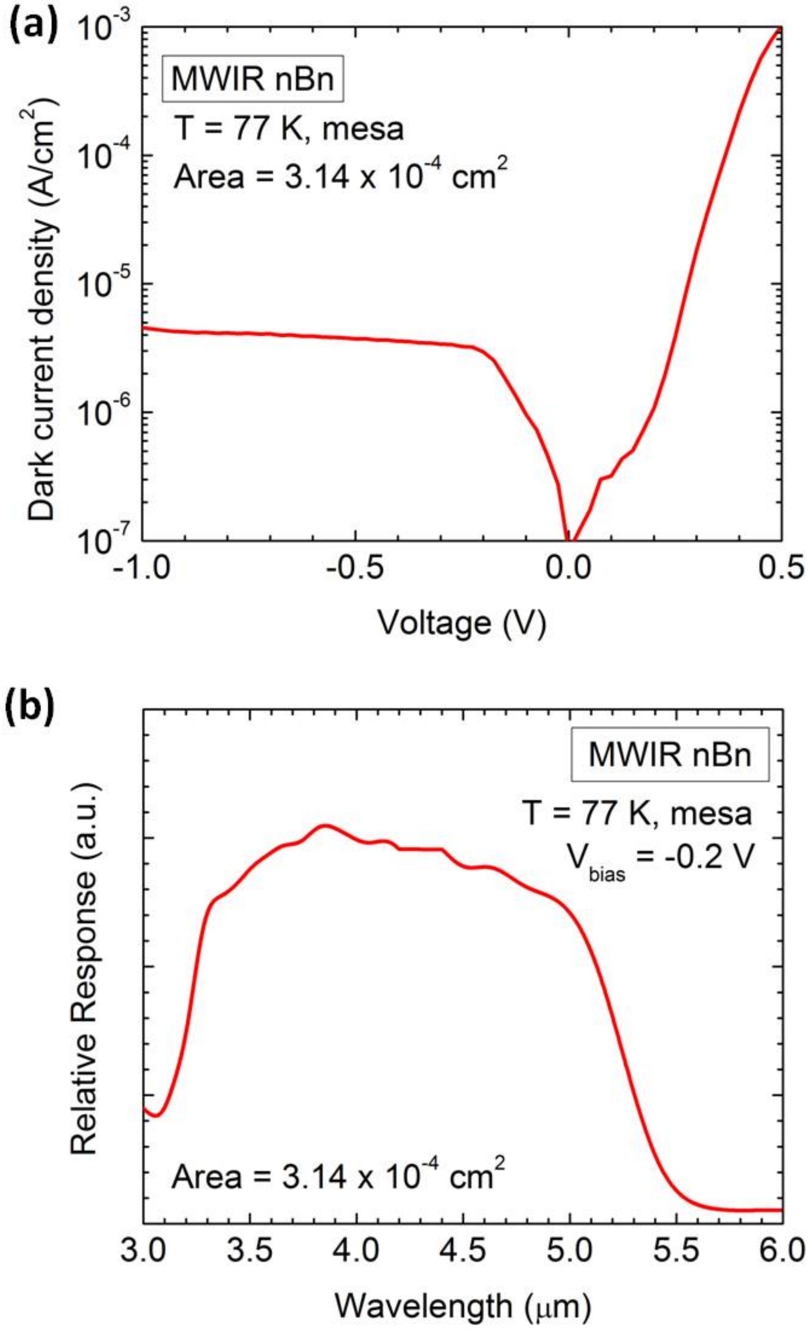

Figure 7.22: Measured (a) dark current density and (b) relative response at 77 K and -0.2 V reverse bias for optimized, second-iteration mesa MWIR (MCT2-086) HgCdTe nBn structure with area $3.14{\times}10^{-4}$ cm^2.

perature dependent trends, while optical measurements of the planar-mesa MWIR HgCdTe nBn device at varying operating biases indicate a bias-dependent spectral response. Furthermore, perimeter leakage current was identified as the limiting mechanism of the device and should be addressed by improving sidewall passivation and/or modifying the device set-up in future work. Finally, strategic adjustments were made to optimize the mesa MWIR HgCdTe nBn device structure, and the modified device showed significant improvement in the J_{dark} values while still exhibiting similar relative response behavior. The HgCdTe nBn device provides a potential alternative to conventional high-performance p-n heterojunction IR detectors, and this preliminary demonstration motivates further investigation of these and related type-I structures for future barrier-integrated IR detector applications.

CHAPTER VIII

Design and Modeling of Auger-Suppressed Unipolar HgCdTe NBνN Detectors

8.1 Background and Motivation

In this chapter, a bandgap engineered hybrid NBνN architecture is proposed for high temperature operation by combining and exploiting the advantages of both HOT (Chapters IV and V) and nBn (Chapters VI and VII) detector structures. The NBνN architecture is expected to achieve lower dark current than conventional *p*-*n* junction photodiodes, nBn, and HOT devices. The simulated performance characteristics of optimized MWIR and LWIR HgCdTe NBνN devices are studied and compared to those of comparable HgCdTe nBn [94] and *p*-*n* junction DLPH detectors [92]. The NBνN architecture is one example of an alternative high performance device design based on the unipolar nBn structure.

8.2 Modeling the HgCdTe NBνN Detector

Numerical simulations were performed using Sentaurus Device to examine the behavior and performance values of the HgCdTe NBνN device. As with previous theoretical studies, the methodology and validation used for the device model follow

MWIR ($\lambda_{co} = 5\mu$m) and LWIR ($\lambda_{co} = 12\mu$m) NBνN Parameters						
Layer	Thickness	Cd composition	Doping	E_{trap}	SRH lifetimes	F_1F_2
Top (N_1^+)	$t_{N_1^+} = 1\ \mu$m	$x_{N_1^+} = x_{abs} + 0.1$	$N_D = 5{\times}10^{15}$ cm^{-3}	$0.25E_g$	$\tau_{n0} = 10\ \mu$s $\tau_{p0} = 1\ \mu$s	0.3
Barrier (B)	$t_B = 50$ nm	$x_B = 0.45$	$N_D = 7{\times}10^{14}$ cm^{-3}			
Absorber (ν)	$t_{abs} = 3\ \mu$m	x_{abs} = varied for λ_c	$N_D = 7{\times}10^{14}$ cm^{-3}			
Bottom(N_2^+)	$t_{N_2^+} = 1\ \mu$m	$x_{N_2^+} = x_{abs} + 0.1$	$N_D = 5{\times}10^{17}$ cm^{-3}			

Table 8.1: MWIR and LWIR HgCdTe NBνN device structural and geometric simulation parameters.

that described in Chapter III. Table 8.1 lists the simulation parameters used for modeling MWIR and LWIR NBνN, nBn, and DLPH structures.

8.2.1 HgCdTe NBνN Device Structure and Operation

The NBνN device comprises four layers including the 1) cap (N_1^+), 2) barrier (B), 3) absorber (ν), and 4) bottom (N_2^+) layers as illustrated in Figure 8.1. Like the nBn detector, the conduction band offset ΔE_c at the N_1^+-B interface prevents the flow of majority carrier (electron) current from the N_1^+ cap region to the absorber. At equilibrium, a large valence band barrier ΔE_v exists at the B-ν interface blocking the flow of the minority carrier (hole) current in the direction of the N_1^+ cap layer. The calculated valence band offset at the B-ν interface in equilibrium ranges between ~15% - 20% depending on the Cd composition and doping concentration of the adjacent layers.

For ideal device operation, the minority carrier holes must be collected at the N_1^+ contact; therefore, a top-negative (reverse) bias is required. Under bias, the energy bands of the NBνN device become inverted, resulting in current flow that is dominated by minority carrier holes. In this mode, the NBνN structure is effectively a minority carrier conduction device. The applied bias aligns the band-edges of the NBνN layers to reduce ΔE_v, allowing for the flow and collection of thermally and optically generated holes from the absorber layer to the N_1^+ cap region. The desired

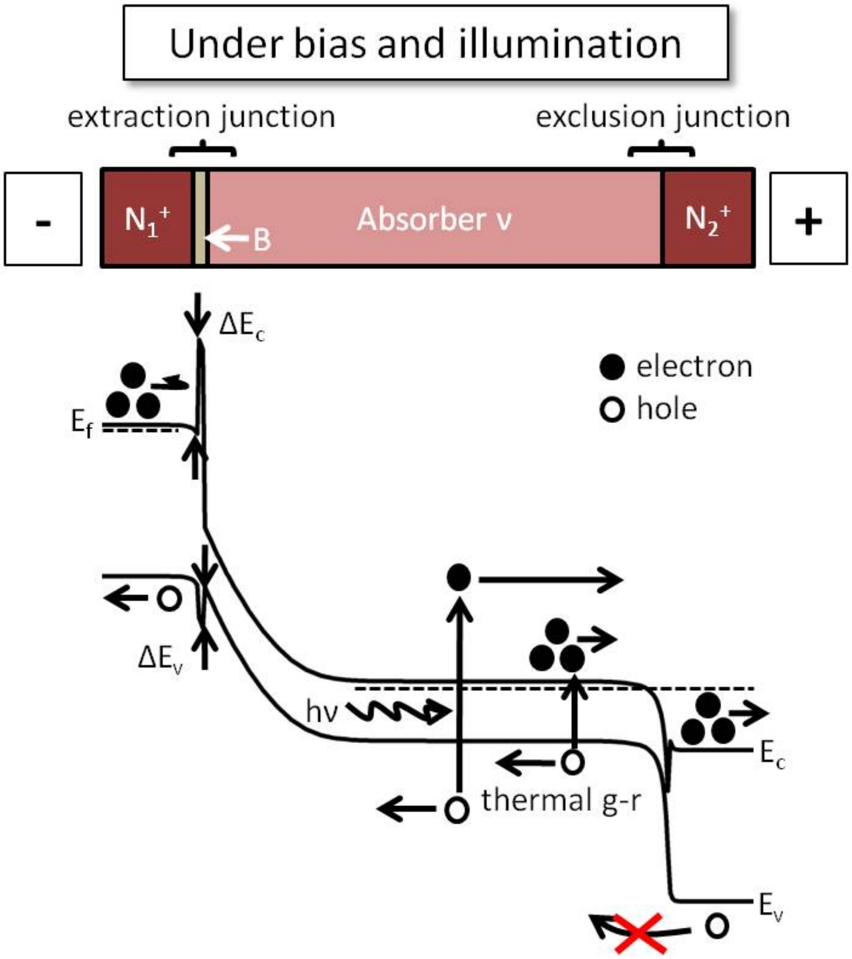

Figure 8.1: Structural layer schematic and energy band diagram of the HgCdTe NBνN photodetector under top-negative (reverse) bias and illumination conditions.

band alignment of the N_1^+, B, and ν layers should somewhat resemble a *p*-*n* diode under reverse bias.

An operating reverse bias value of 450 mV (negative voltage applied to the cap region) was selected for consistency with the nBn optimization simulations [94] and to ensure device operation in the post-'turn-on' threshold region, where the 'turn-on' voltage is defined as the bias at which ΔE_v is minimized. Similar to the nBn detector, biases below 450 mV are generally sufficient for device operation as long as the dark current density is determined to be at or above the turn-on threshold.

SRH generation processes in the depletion region within the lightly doped barrier

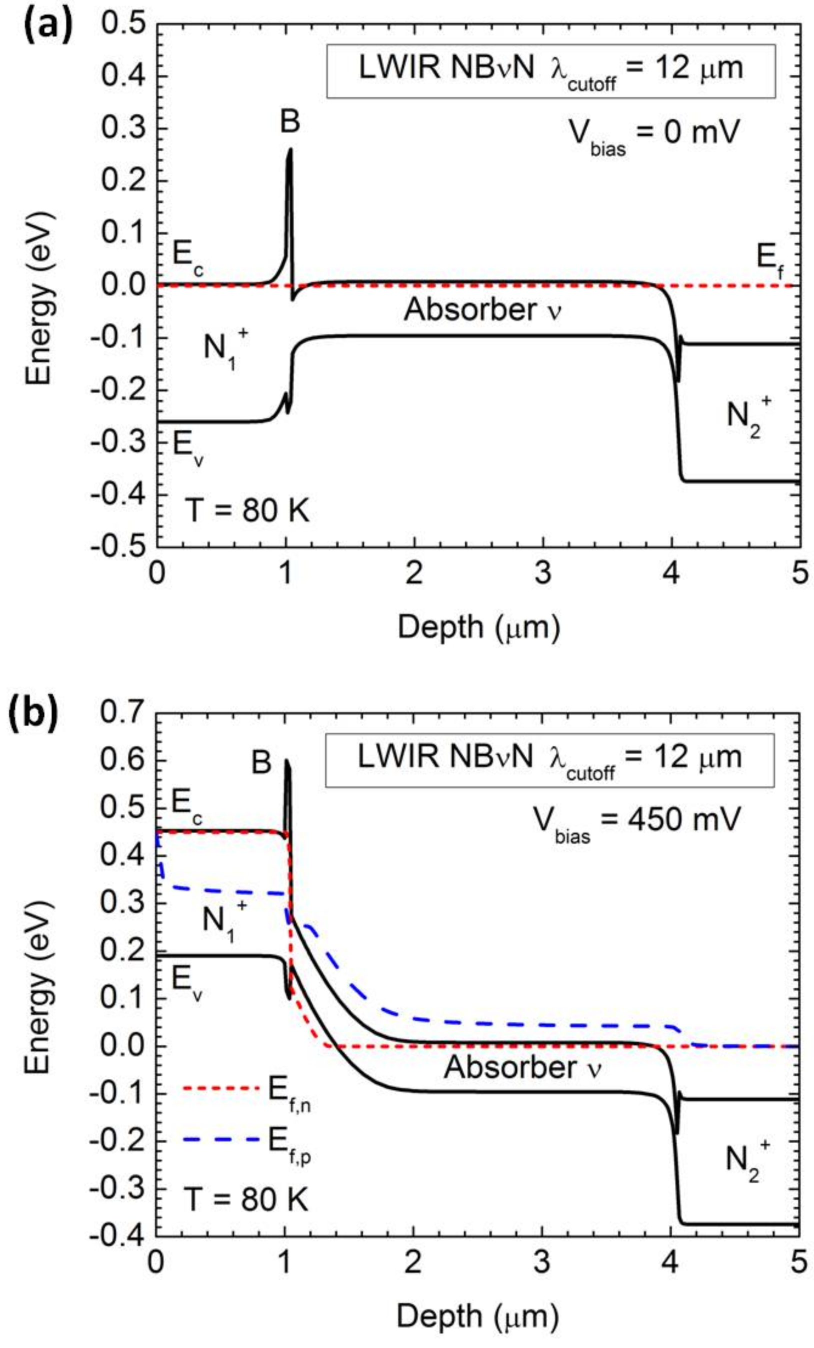

Figure 8.2: Calculated energy band diagrams of the LWIR HgCdTe NBνN photodetector device at (a) equilibrium and (b) under reverse bias without illumination.

layer are suppressed due to the large bandgap energy. It is noted that the low doping concentrations in the barrier and the absorber results in the formation of a bias-induced depletion region extending into the absorber layer as observed in the HgCdTe nBn device [94]. While this design is non-ideal for mitigating SRH processes, carrier generation at low temperatures via activated trap centers appear to be minimal as observed by the low J_{dark} values described later in this chapter.

Like the HOT structure, the NBνN device consists of an extraction and exclusion junction formed at the interface of the N_1^+ cap, barrier, and absorber layers and the interface of the absorber and N_2^+ layers, respectively (Figure 1.17). Under bias, the unipolar extraction junction effectively removes thermally generated minority carriers from the absorber region. With increasing bias, the holes are extracted from the absorber at a rate higher than which they can be replenished by holes in the highly doped N_2^+ region through the exclusion junction. Consequently, the hole concentration in the absorber drops significantly below the thermal equilibrium value. To maintain charge neutrality in the absorber regions, the electron concentration is also reduced below equilibrium, as shown in Figure 8.3. In this way, thermal Auger G-R processes are suppressed by decreasing the overall intrinsic carrier concentration in the active layer. This mechanism is similar to what is observed in the HOT detector.

The structural parameters listed in Table 8.1 for the NBνN device are based on optimized values obtained for the HOT and nBn detectors in Chapters IV and VI. The calculated energy band diagrams of the proposed LWIR HgCdTe NBνN device are illustrated in 8.2.

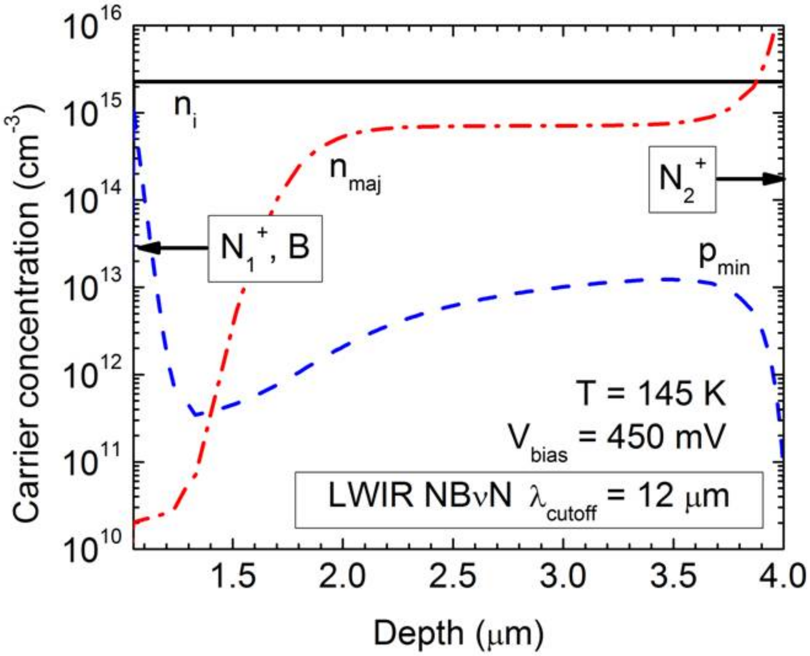

Figure 8.3: Calculated LWIR NBνN carrier concentration profiles.

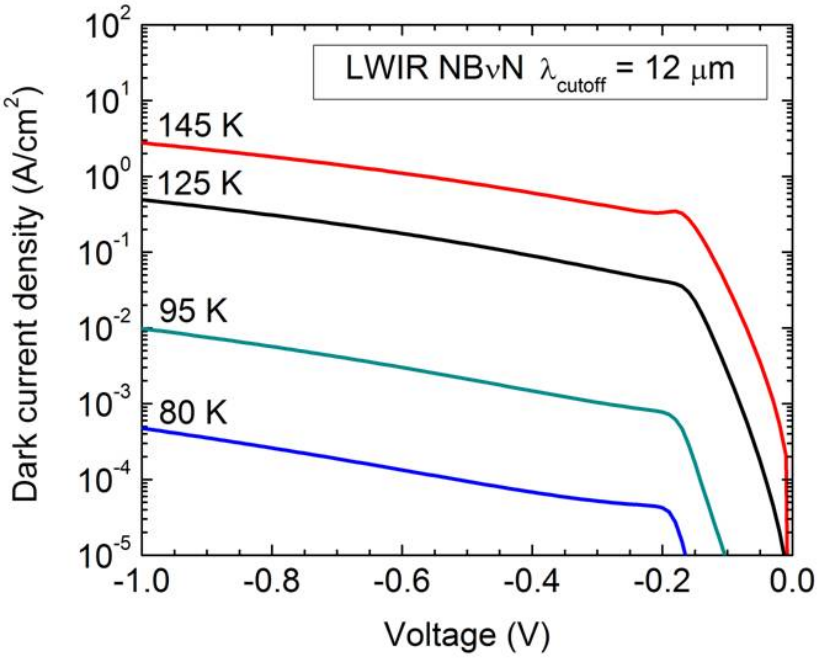

Figure 8.4: Calculated LWIR NBνN current-voltage characteristics at varying temperatures.

8.3 Results and Discussion

8.3.1 J_{dark} Characteristics

Representative I-V characteristics of a LWIR NBνN device are shown in Figure 8.4 for several temperatures ranging from 80 to 145 K. Distinctive current saturation behavior is observed in the I-V curves at all temperatures, and is attributed to the barrier in the valence band at the extraction junction. The turn-on feature is observed as an inflection in the I-V characteristic for biases near 200 mV. This feature indicates the proper alignment of the N_1^+ cap, barrier, and absorber region band-edges, allowing unrestricted flow of hole current arising from the minority carrier generation in the absorber layer. The ideal region of device operation is any reverse bias larger than the turn-on threshold value where the current density is not dominated by significant breakdown effects. A slope is observed in the post-threshold J_{dark} with increasing bias. This behavior is believed to be attributed to the bias-dependent band bending in the lightly-doped absorber region of the NBνN device. At higher temperatures (125 K and 145 K in Figure 8.4), NDR behavior is observed in the LWIR device. The NDR is caused by the Auger suppression mechanism which becomes especially pronounced at high temperatures where Auger generation processes typically increase in the narrow bandgap material of the active layer.

The calculated post-threshold J_{dark} of the MWIR and LWIR NBνN, nBn, and DLPH devices as a function of temperature for specified biases are shown in Figures 8.5. The cutoff wavelengths indicated in the plots were obtained by adjusting the Cd fraction of the absorber in the respective devices for each temperature. The post-threshold J_{dark} is determined as the current density value at a reverse bias of 450 mV for both NBνN and nBn devices, and 300 mV for the DLPH detector. The NBνN device exhibits J_{dark} values between one to two orders of magnitude lower than those observed in the nBn and DLPH devices for temperatures shown in Figures 8.5a

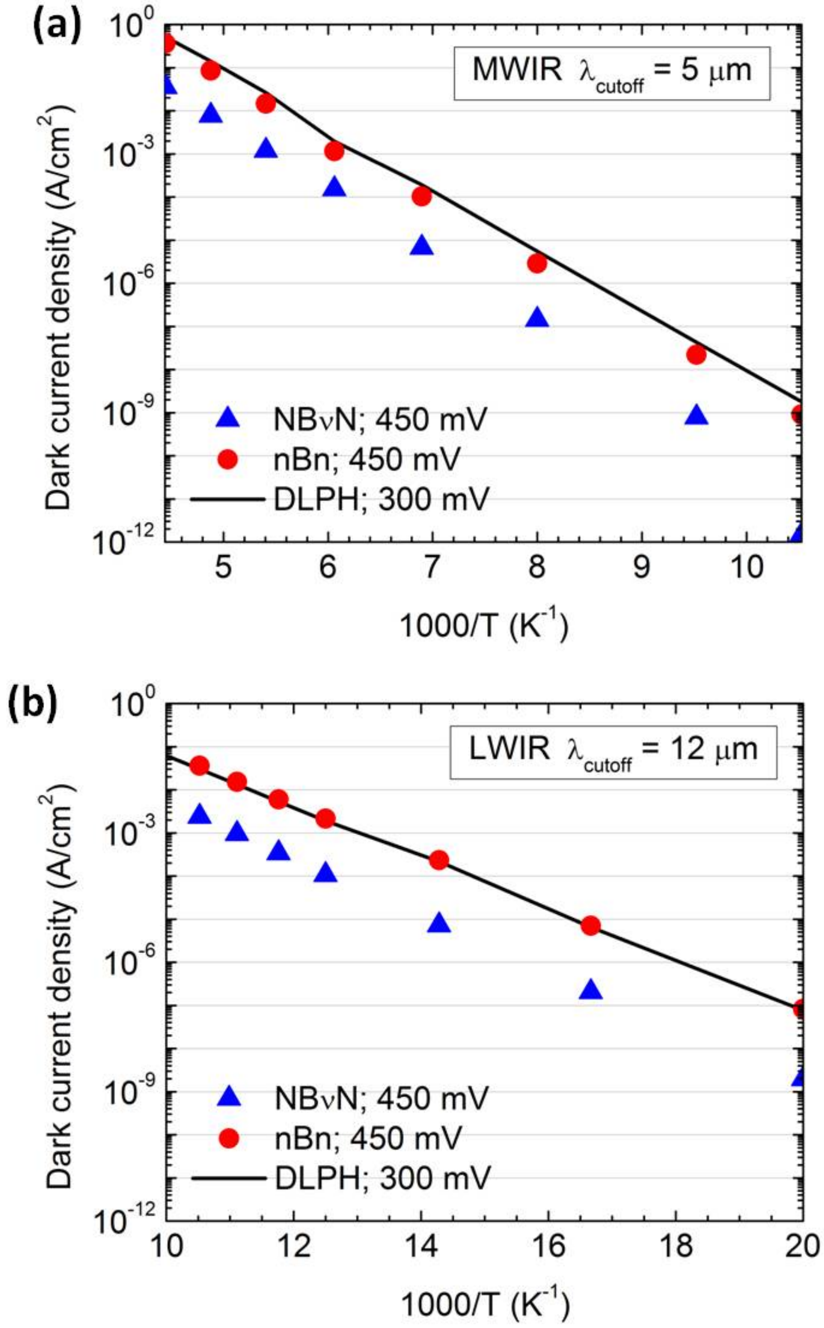

Figure 8.5: Calculated dark current density as a function of temperature for (a) MWIR and (b) LWIR NBνN, nBn, and DLPH photodetectors.

and 8.5b for the MWIR and LWIR spectral regions, respectively. The significant decrease in the NBνN dark current density for both MWIR and LWIR structures is the result of the effective Auger-suppression mechanism. At higher temperatures, the NBνN J_{dark} values begin to converge to the nBn and DLPH values. The decreased dark current density improvement observed in the NBνN device is believed to be due to the large number of majority carriers (electrons) surmounting the conduction band barrier with increasing temperature.

8.3.2 Spectral Response

Figure 8.6 shows representative quantum efficiency and responsivity values for LWIR NBνN, nBn, and DLPH devices at 80 K under 450 mV reverse bias as a function of incident wavelength. All of the devices exhibit QE values in the mid-60% under the given ideal conditions. As one might expect, the NBνN device exhibits a smaller tail due to the reduced absorption caused by the short absorber width (3 μm) compared to those of the nBn and DLPH devices (10 μm). However, the NBνN device exhibits a slightly larger peak responsivity than comparable nBn and DLPH devices, leading to higher peak D^* values.

8.3.3 Peak D^*

Figures 8.7a and 8.7b illustrate higher peak D^* values achieved by the NBνN device for the range of temperatures (MWIR: 95 - 225 K, LWIR: 50 - 95 K) examined. Unrealistic quantum efficiency values greater than 100% were obtained for temperatures above 225 K (MWIR) and 95 K (LWIR). Similar values were observed for the MWIR and LWIR nBn devices. This behavior may be attributed to non-ideal changes in the simulated potential barriers due to photogenerated carriers. D^* values for this range of temperatures were ignored for the time being until experimental data is available to further analyze the validity of this type of behavior. Overall, the

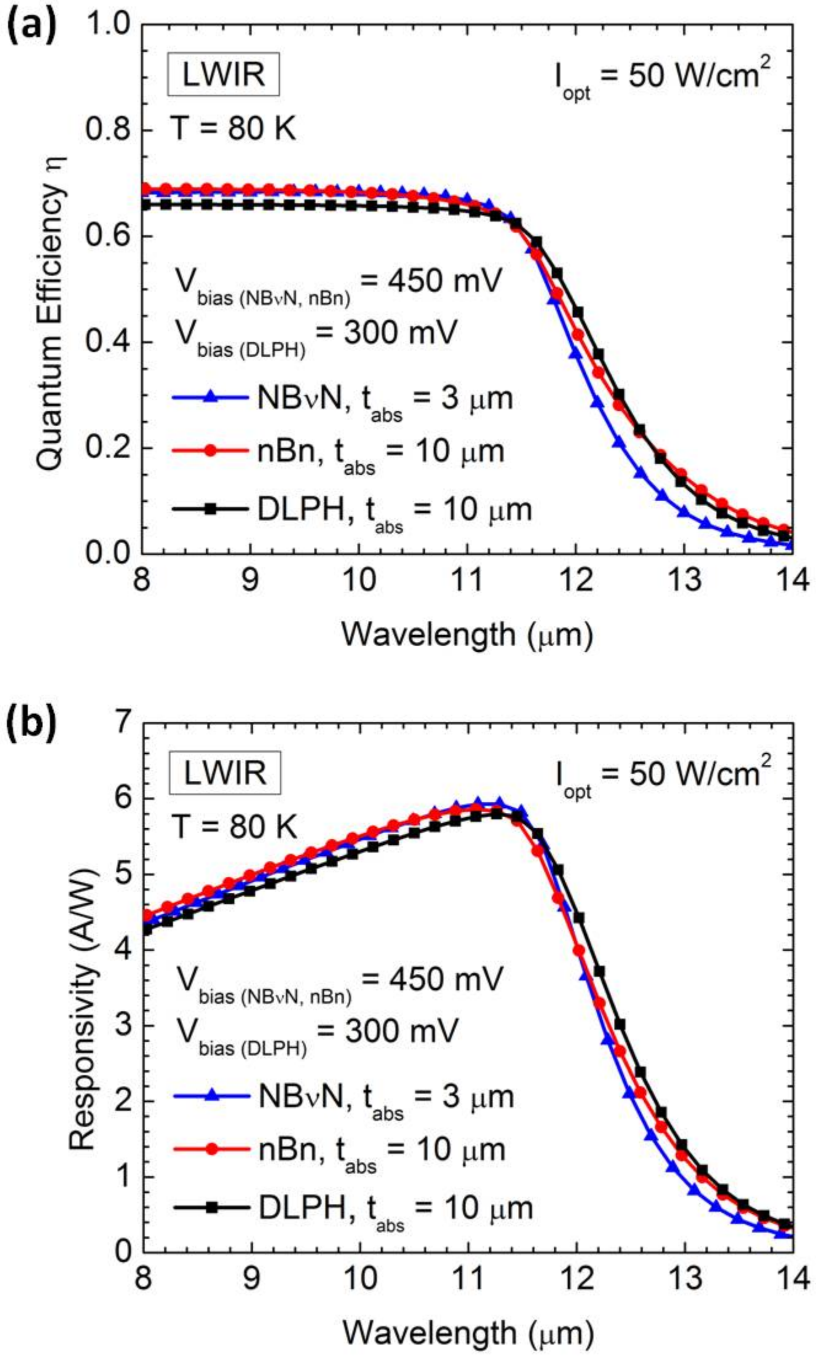

Figure 8.6: Calculated (a) quantum efficiency and (b) responsivity as a function of incident wavelength for LWIR NBνN, nBn, and DLPH photodetectors.

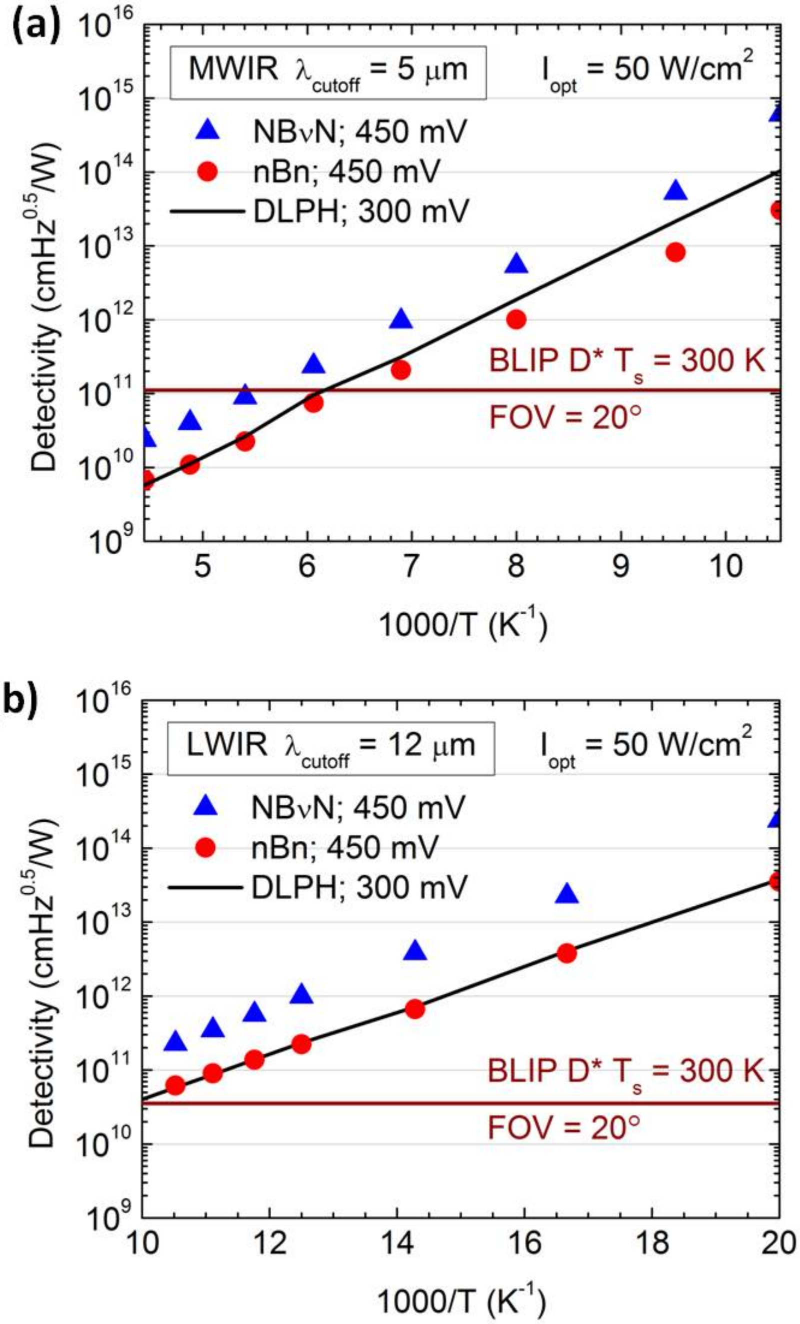

Figure 8.7: Calculated peak detectivity for (a) MWIR and (b) LWIR NBνN, nBn, and DLPH devices at varying temperatures.

suppressed Auger and SRH G-R mechanisms result in high predicted performance values for the NBνN structure.

8.4 Conclusion

This study highlights the potential benefits of the hybrid HgCdTe NBνN structure which combines the distinct advantages of the HOT and nBn designs. Compared to MWIR and LWIR HgCdTe nBn and DLPH devices, the calculated J_{dark} and peak D^* values of the NBνN device are significantly improved due to the effective Auger-suppression mechanism. This preliminary investigation suggests that the proposed unipolar NBνN architecture is a potentially viable solution to achieve reduced cooling requirements for high performance IR detection using a simple design. Experimental implementation in future work is needed to validate the predicted behavior and performance characteristics of the NBνN detector.

CHAPTER IX

Conclusions and Future Work

This collective study examined three bandgap-engineered HgCdTe detector architectures for reduced cooling requirements: 1) the Auger-suppressed non-equilibrium HOT device (Chapters IV and V), 2) the unipolar nBn device (Chapters VI and VII), and 3) the hybrid NBνN device combining the benefits and designs of both HOT and nBn structures (Chapter VIII). As discussed in Chapter I, the performance of state-of-the-art *p*-*n* junction technology is primarily limited by two major issues: intrinsic thermal Auger generation mechanisms and processing challenges around achieving well-controlled, stable *p*-type doping in MBE grown HgCdTe material. The designs proposed in this study aim to address these limitations by using alternative methods to achieve high-performance IR detection that is comparable to or better than HgCdTe *p*-*n* junction photodiodes, with the ultimate goal of integrating the devices for FPA applications. Theoretical and experimental investigations were performed over the course of this work to facilitate a better understanding of the complex relationship between HgCdTe material properties, detector designs, physical mechanisms, and performance characteristics.

The conceptualized architectures were simulated using a discretized numerical device model based on the Synopsys TCAD tool, Sentaurus Device, detailed in Chapter III. The model incorporates HgCdTe material parameters described in Chapter II and self-consistently solves the Poisson equation and electron and hole continuity equations. The device model was validated by comparing calculated results of the DLPH structure to those of previously published experimental data. Numerical simulations based on this model were used to optimize the proposed detector designs by varying structural parameters such as the Cd composition, doping concentration, and layer thickness and analyzing the calculated J_{dark}, D^*, QE, and R values.

Chapter IV examined the predicted performance characteristics of optimized MWIR and LWIR HOT devices compared to conventional DLPH devices. Overall, J_{dark} values of the MWIR and LWIR HOT devices were calculated to be between one and two orders of magnitude lower than those observed in comparable DLPH structures for the same range of operating temperatures. At higher temperatures, the LWIR HOT device exhibited clear NDR behavior in its I-V characteristics due to the bias-dependent Auger-suppression mechanism. Despite having a shorter absorber width, the responsivity of the HOT device was found to be similar to that of the DLPH structure. More notably, the calculated D^* values of both HOT and DLPH devices for varying cutoff wavelengths between 5 μm and 12 μm with a 20° FOV and 300 K background scene temperature showed that the calculated BLIP temperatures of the HOT structure are consistently higher over the range of cutoff wavelengths. This is due to the Auger suppression mechanism reducing the J_{dark} values. A large difference of ΔT_{BLIP} ranging from 43 K - 50 K was achieved over this range of wavelengths, indicating a significant predicted improvement in cooling requirements for the proposed HOT device.

As described in Chapter V, arsenic diffusion for p-type doping was studied in MWIR and LWIR MBE grown HgCdTe HOT devices in conjunction with the theoretical work,. These experiments were motivated by the importance of controlling the doping concentration profile within the absorber region of a $P^+/\pi/N^+$ HOT structure with a preference for a p-type absorber due to the longer Auger 7 minority carrier lifetimes and reduced generation rates. However, achieving controllable *in situ* p-type doping by MBE remains a challenge. To address the issue, a method based on earlier work by Wijewarnasuriya et al. [25] was used, combining shallow As implantation with a deep diffusion anneal to achieve a P^+/π step structure. The experimental data showed that this technique achieved controllable deep diffusion of low As concentration in the absorber layer, resulting in a P^+/π step structure. Data trends show low As concentrations in the absorber were obtained for samples using low Hg partial pressure and long anneal times. Furthermore, this study found that annealing at low $P(Hg)$ increased the effects of deep diffusion more significantly than annealing at high $P(Hg)$ for a longer period. Low As diffusion coefficients were also observed compared to data from past studies where samples were annealed at higher substrate temperatures; the difference in the MWIR and LWIR sample values was attributed to the variation in Hg vacancy concentration associated with HgCdTe alloys with higher Cd fractions. The data obtained in this study are significant in illustrating the effects of annealing conditions on deep diffusion characteristics and provide additional experimental insight on achieving HOT structure via implantation and diffusion techniques.

Another solution to address the *in situ* p-type doping issue was proposed in the theoretical investigation of the type-I, barrier-integrated, unipolar HgCdTe nBn device discussed in Chapter VI. The nBn structure, originally demonstrated in III-V semiconductors, is a promising alternative for replacing or supplementing DLPH technology. By eliminating requirements for p-type material, thus avoiding lower material quality due to implantation-induced defects, and removing high temperature annealing steps, the simplified HgCdTe nBn device offers a significant advantage over conventional p-n junction photodiodes from both practical and performance standpoints. Unlike type-II III-V semiconductors which can be tailored to achieve a near-zero valence band offset at the barrier interface, the type-I nature of HgCdTe results in a non-zero valence band barrier that creates a performance trade-off. Careful optimization of the device layers using modeling shows that the barrier Cd composition is the most critical aspect of the design, affecting both the overall J_{dark} and carrier collection. Unique I-V characteristics were observed corresponding to valence band-edge alignment behavior with J_{dark} 'turn-on' biases depending on the value of the valence band offset. These simulations also showed that the nBn device requires a slight operating bias at or above the turn-on bias threshold. The initial theoretical work suggested that despite certain trade-offs, the HgCdTe nBn device is potentially capable of achieving near equivalent performance to the DLPH device in both MWIR and LWIR spectral ranges. The calculated performance values of the nBn detector exhibited similar responsivity, low J_{dark}, and high D^* values compared to those of the corresponding DLPH device.

The promising results of the theoretical work on the HgCdTe nBn device motivated the experimental investigation detailed in Chapter VII. MBE grown MWIR and LWIR HgCdTe nBn devices were fabricated in planar-mesa and mesa configurations. Temperature-dependent I-V measurements and optical response testing showed bias-dependent characteristics consistent with band-edge alignment behavior predicted theoretically. First-generation nBn devices exhibited I-V characteristics with measured J_{dark} 'turn-on' bias regions of -0.5 to -1.0 V and -0.2 to -0.6 V for MWIR and LWIR devices, respectively. The measured J_{dark} values at low temperatures were considerably higher than those calculated using the device model, but this discrepancy was attributed to perimeter leakage current caused by damage incurred during absorber layer etching and poor surface passivation. MWIR and LWIR planar-mesa devices showed lower J_{dark} values compared to mesa devices, and a clear correlation of J_{dark} to perimeter-over-area ratio was observed in all device sets, confirming sidewall leakage contribution. Structural modifications such as reducing the doping concentration and increasing the thickness of the barrier layer were made to second-iteration nBn structures, and the J_{dark} of a resulting MWIR nBn mesa device was approximately five orders of magnitude lower than that observed in corresponding first-iteration planar-mesa and mesa devices. Relative response measurements for first- and second-iteration MWIR devices exhibited cutoff wavelengths near 5.7 μm and 5.2 μm, respectively. These results comprise the first-reported demonstration and subsequent progress and development of HgCdTe nBn devices.

Chapter VIII proposed a hybrid NBνN device for high temperature operation, which builds on the unipolar device concept. Preliminary modeling showed the NBνN device, combining the structures and performance benefits of the Auger-suppressed HOT and unipolar nBn devices, achieved considerably lower J_{dark} and higher D^* values than those predicted for corresponding DLPH and nBn devices for similar temperatures between 95 - 225 K for the MWIR spectral band and 50 - 95 K for the LWIR spectral band. Moreover, the calculated NBνN device characteristics generally followed those of the nBn and HOT devices, exhibiting J_{dark} 'turn-on' behavior, and NDR attributed to the Auger-suppression mechanism at higher temperatures in the LWIR NBνN device. This final investigation underlines the potential benefits of the hybrid, unipolar NBνN structure. With the realization and further progress of the MBE grown HgCdTe nBn device, a basis component, the development of a functional high performance, high temperature HgCdTe NBνN IR detector is well within reach.

Maturing the concepts of barrier-integrated unipolar devices, however, will require further work on the proposed alternative devices. In the short term, addressing the performance limiting perimeter leakage current in the nBn detector is imperative. This can be done by either improving passivation techniques using CdTe layers instead of ZnS and controlling the etch depth into the absorber for contact placement or modifying the contact configuration to eliminate absorber etching altogether. It may also be beneficial to focus on minimizing the valence band barrier offset ΔE_v through the use of graded Cd composition and doping profiles to mitigate the challenges posed by the type-I nature of HgCdTe. The device model should also be improved to include non-idealities such as non-uniform Cd composition and doping concentration profiles, carrier tunneling through the barrier, top surface and sidewall defects, trap states, and surface charges to provide a better understanding of realistic nBn device behavior. In the long term, the NBνN detector can be fabricated using the improved nBn structure for the extraction junction. Successfully demonstrating the NBνN detector would open doors for pursuing more complex barrier-integrated architectures such as NBνBN or PBνBN configurations for enhanced Auger-suppression and higher temperature operation.

Major research efforts on HgCdTe IR detectors continue to focus on increasing the device operating temperature and format array sizes for high-end FPA applications. While competing technologies based on III-V semiconductors have emerged, HgCdTe continues to remain the front-runner for high performance detector applications. Future detector architectures must address the needs of advancing technology requirements by accommodating and exploiting the unique characteristics of the HgCdTe material. This extended study on alternative HgCdTe detectors for reduced cooling requirements is intended to provide the theoretical basis and experimental prototypes for the HOT, nBn, and NBνN detectors designed for next-generation IR sensing applications.

BIBLIOGRAPHY

BIBLIOGRAPHY

[1] A. Rogalski. *Infrared Detectors.* CRC Press, Boca Raton, FL, second edition edition, 2011.

[2] A. Rogalski, K. Adamiec, and J. Rutkowski. *Narrow-Gap Semiconductor Photodiodes.* SPIE-The International Society for Optical Engineering, Bellingham, WA, 2000.

[3] J. Piotrowski and A. Rogalski. *High Operating Temperature Infrared Photodetectors.* SPIE, Bellingham, WA, 2007.

[4] P.Y. Emelie. *HgCdTe Auger-Suppressed Infrared Detectors Under Non-Equilibrium Operation.* Ph.d. thesis, University of Michigan, 2009.

[5] B.L. Anderson and R.L. Anderson. *Fundamentals of Semiconductor Devices.* McGraw Hill, New York, 1 edition, 2005.

[6] A. Rogalski. HgCdTe infrared detector material: history, status and outlook. *Reports on Progress of Physics*, 68:2267–2336, 2005.

[7] A. Rogalski. Infrared detectors: status and trends. *Progress in Quantum Electronics*, 27(2):59–210, 2003.

[8] G.N. Pultz, P.W. Norton, E.E. Kreuger, and M.B. Reine. Growth and characterization of P-on-n HgCdTe liquid-phase epitaxy heterojunction material for 11-18 μm applications. *J. Vac. Sci. Technol. B*, 9(3):1724–1730, 1991.

[9] P.W. Norton, P. LoVecchio, G.P. Pultz, J. Hughes, T. Robertson, V. Lukach, and K. Wong. Scale-up of LPE processes for flexibility in manufacturing. *Proc. SPIE*, 2228:73–83, 1994.

[10] E.P.G. Smith, R.E. Bornfreund, I. Kasai, L.T. Pham, E.A. Patten, J.M. Peterson, T.J. De Lyon, J.W. Bangs, S.M. Johnson, W.A. Radford, J.A. Roth, B.Z. Nosho, and J.E. Jensen. Status of two-color and large format HgCdTe FPA technology at Raytheon Vision Systems. *Proc. SPIE*, 6127:6121F, 2006.

[11] P. Capper and J. Garland, editors. *Mercury Cadmium Telluride, Growth, Properties and Applications.* Wiley, 2011.

[12] J.M. Arias, J.G. Pasko, M. Zandian, S.H. Shin, G.M. Williams, L.O. Bubulac, R.E. DeWames, and W.E. Tennant. Planar *p*-on-*n* HgCdTe heterostructure photovoltaic detectors. *Appl. Phys. Lett.*, 62(9):976–978, 1993.

[13] J. Bajaj. State-of-the-art HgCdTe infrared devices. *Proc. SPIE*, 3948:42–54, 2000.

[14] S. M. Johnson, T. J. de Lyon, C. A. Cockrum, W. J. Hamilton, T. Tung, F. I Gessweini, B. A. Baumgratz, L. M. Ruzicka, O. K. Wu, and J. A. Roth. Direct growth of CdZnTe/Si substrates for large-area HgCdTe infrared focal plane arrays. *J. Electron. Mater.*, 24(5):467–473, 1995.

[15] P.S. Wijewarnasuriya, M. Zandian, D.D. Edwall, W.V. McLevige, C.A. Chen, J.G. Pasko, G. Hildebrandt, A.C. Chen, J.M. Arias, and A.I. D'Souza et al. MBE P-on-n $Hg_{1-x}Cd_xTe$ heterostructure detectors on silicon substrates. *J. Electron. Mater.*, 27(6):546–549, 1998.

[16] O. Gravrand and Ph. Chorier. Status of very long infrared-wave focal plane array development at DEFIR. *Proc. SPIE*, 7298:729821, 2009.

[17] C.T. Sah, R.N. Noyce, and W. Shockley. Carrier generation and recombination in p-n junction and p-n junction characteristics. *Proc. IRE*, 45:1228–1243, 1957.

[18] S.C. Choo. Carrier generation-recombination in the space charge region of an asymmetrical p-n junction. *Solid-State Electr.*, 11:1069–1077, 1968.

[19] S.M. Sze. *Physics of Semiconductor Devices.* New-York: Wiley, 1981.

[20] M.A. Kinch. Metal-insulator-semiconductor infrared detectors. In R.K. Willardson and A.C. Beer, editors, *Semiconductors and Semimetals*, volume 18, pages 313–378. New York: Academic Press, 1981.

[21] L.O. Bubulac, W.E. Tennant, R.A. Riedel, and T.J. Magee. Behavior of implantation-induced defects in HgCdTe. *J. Vac. Sci. Technol.*, 21(4):251–254, May/June 1982.

[22] H.F. Schaake. Ion implantation damage in $Hg_{0.8}Cd_{0.2}Te$. *J. Vac. Sci. Technol. A.*, 4(4):2174–2176, Jul/Aug 1986.

[23] L.O. Bubulac. Defects, diffusion and activation in ion implanted HgCdTe. *J. Cryst. Growth*, 86(1-4):723–134, 1988.

[24] G.l. Destefanis. Electrical doping of HgCdTe by ion implantation and heat treatment. *J. Cryst. Growth*, 86(1-4):700–722, 1988.

[25] P.S. Wijewarnasuriya, G. Brill, Y. Chen, N.K. Dhar, C.H. Grein, S. Velicu, P.Y. Emelie, H. Jung, S. Sivananthan, A. D'Souza, M.G. Stapelbroek, and J. Reekstin. Pronounced Auger suppression in long wavelength HgCdTe. *Proc. SPIE*, 6542(65420G):1–8, 2007.

[26] A.C. Chen, M. Zandian, D.D. Edwall, R.E. De Wames, P.S. Wijewarnasuriya, J.M. Arias, S. Sivananthan, M. Berding, and A. Sher. Modeling of arsenic activation in HgCdTe. *J. Electron. Mater.*, 27(6):595–599, 1998.

[27] E.C. Piquette, D.D. Edwall, D.L. Lee, and J.M. Arias. Precise arsenic doping of HgCdTe by MBE and effects on compositional interdiffusion. *J. Electron. Mater.*, 35(6):1346–1349, 2006.

[28] M. Zandian, A.C. Chen, D.D. Edwall, J.G. Pasko, and J.M. Arias. p-type arsenic doping of $Hg_{1-x}Cd_xTe$ by molecular beam epitaxy. *Appl. Phys. Lett.*, 71(19):2815–2817, November 1997.

[29] G.K.O. Tsen, R. Sewell, A.J. Atanacio, K.E. Prince, C.A. Musca, J.M. Dell, J. Antoszewski, and L. Faraone. Characterisation of arsenic doped HgCdTe grown by molecular beam epitaxy. In *2006 Conference on Optoelectronic and Microelectronic Materials and Devices*, volume 55, 2006.

[30] T. Ashley and C.T. Elliot. Non-equilibrium devices for infra-red detection. *Electron. Lett.*, 21(2):451–452, May 1985.

[31] S. Maimon and G.W. Wicks. nBn detector, an infrared detector with reduced dark current and higher operating temperature. *Appl. Phys. lett*, 89(151109):1–3, October 2006.

[32] G.R. Savich, J.R. Pedrazzani, S. Maimon, and G.W. Wicks. Use of epitaxial unipolar barriers to block surface leakage currents in photodetectors. *Phys. Status Solidi C*, 7(10):2540–2543, 2010.

[33] J.R. Pedrazzani, S. Maimon, and G.W. Wicks. Use of nBn structures to suppress surface leakage currents in unpassivated InAs infrared photodetectors. *Electronic Letters*, 44(25), December 2008.

[34] P. Norton. HgCdTe infrared detectors. *Opto-electronics Review*, 10(3):159–174, 2002.

[35] G.L. Hansen, J.L. Schmidt, and T.N. Casselman. Energy gap versus alloy composition and temperature in $Hg_{1-x}Cd_xTe$. *J. Appl. Phys.*, 53(10):7099–7101, October 1982.

[36] J. Wenus, J. Rutkowski, and A. Rogalski. Two-dimensional analysis of double-layer heterojunction HgCdTe photodiodes. *IEEE Trans. Electron Devices*, 48(7):1326–1332, 2001.

[37] G.L. Hansen and J.L. Schmit. Calculation of intrinsic carrier concentration in $Hg_{1-x}Cd_xTe$. *J. Appl. Phys.*, 54(4):1639–1640, 1983.

[38] M.H. Weiler. *Semiconductors and Semimetals*, volume 16, chapter Magnetooptical Properties of $Hg_{1-x}Cd_xTe$ Alloys, pages 119–191. Academic Press, New York, 1981.

[39] W. Scott. Electron mobility in $Hg_{1-x}Cd_xTe$. *J. Appl. Phys.*, 43(3):1055–1062, 1972.

[40] J.P. Rosbeck, R.E. Starr, S.L. Price, and K.J. Riley. Background and temperature dependent current-voltage characteristic of $Hg_{1-x}Cd_xTe$ photodiodes. *J. Appl. Phys.*, 53(9):6430–6440, 1982.

[41] P.N.J. Dennis, C.T. Elliot, and C.L. Jones. A method for routine characterization of the hole concentration in p-type cadmium mercury telluride. *Infrared Physics*, 22:167–169, 1982.

[42] W.W. Anderson. Absorption constant of $Pb_{1-x}Sn_xTe$ and $Hg_{1-x}Cd_xTe$ alloys. *Infrared Physics*, 20:363–372, 1980.

[43] R. Beattie and A.M. White. An analytic approximation with a wide range of aplicability for band-to-band radiative transition rates in direct narrow-gap semiconductors. *Semicond. Sci. Tech.*, 12:359–368, 1997.

[44] E. Finkman and S.E. Schacham. The exponential optical absorption band tail of $Hg_{1-x}Cd_xTe$. *J. Appl. Phys.*, 56:2896–2900, 1984.

[45] C.A. Hougen. Model for infrared absorption and transmission of liquid-phase epitaxy HgCdTe. *J. Appl. Phys.*, 66:3763–3766, 1989.

[46] M.W. Scott. Energy gap in $Hg_{1-x}Cd_xTe$ by optical absorption. *J. Appl. Phys.*, 40:4077–4081, 1969.

[47] R. Dornhaus, G. Nimtz, and B. Schlicht. *Narrow-Gap Semiconductors*. Springer Verlag, Germany, 1983.

[48] J.S. Blakemore. *Semiconductor Statistics*. Dover Publications, New York, 1987.

[49] Synopsys, Mountain View, CA. *Sentaurus Device*, 2006.

[50] S.E. Schacham and E. Finkman. Recombination mechanisms in p-type HgCdTe: Freezeout and background flux effects. *J. Appl. Phys.*, 57(6):2001–2009, 1985.

[51] J.S. Blakemore. *Semiconductor Statistics*. Dover Publications, New York, 1962.

[52] T.N. Casselman and P.E. Petersen. A comparison of the dominant Auger transitions in p-type (Hg, Cd)Te. *Solid State Communications*, 33:615–619, 1980.

[53] T.N. Casselman. Calculation of the Auger lifetime in p-type $Hg_{1-x}Cd_xTe$. *J. Appl. Phys.*, 52:848–854, 1981.

[54] M.A. Kinch, F. Aqariden, D. Chandra, P.-K Liao, H.F. Schaake, and H.D. Shih. Minority carrier lifetime in p-HgCdTe. *J. Electron. Mater.*, 34:880–884, 2005.

[55] E. Bellotti and D. D'Orsogna. Numerical analysis of HgCdTe simultaneous two-color photovoltaic infrared detectors. *IEEE J. Quantum Electron.*, 42(4):418–426, April 2006.

[56] R. Zucca, D.D. Edwall, J.S. Chen, S.L. Johnston, and C.R. Younger. Minority carrier lifetimes of metalorganic chemical vapor deposition long-wavelength infrared HgCdTe on GaAs. *J. Vac. Sci. Technol. B*, 9(3):1823–1828, 1991.

[57] M.A. Kinch, M.J. Brau, and A. Simmons. Recombination mechanisms in 8-14 μ HgCdTe. *J. Appl. Phys.*, 44(4):1649–1663, 1973.

[58] H. R. Vydyanath. Mechanisms of incorporation of donor and acceptor dopants in (Hg, Cd)Te alloys. *J. Vac. Sci. Technol. B*, 9(3):1716–1723, 1991.

[59] P.S. Wijewarnasuriya, F. Aqariden, C.H. Grein, J.P. Faurie, and S. Sivananthan. p-Type doping with arsenic in (211)B HgCdTe grown by MBE. *J. Cryst. Growth*, 175(1):647–652, 1997.

[60] P.S. Wijewarnasuriya and S. Sivananthan. Arsenic incorporation in HgCdTe grown by molecular beam epitaxy. *Appl. Phys. Lett.*, 72(14):1694–1696, 1998.

[61] F. Aqariden, P.S. Wijewarnasuriya, and S. Sivananthan. Arsenic incorporation in HgCdTe grown by molecular beam epitaxy. *J. Vac. Sci. Technol. B*, 16(3):1309–1311, 1998.

[62] H.F. Schaake, M.A. Kinch, D. Chandra, F. Aqariden, P.K. Liao, D. F. Weirauch, C.F. Wan, R.E. Scritchfield, W.W. Sullivan, J.T. Teherani, and H.D. Shih. High-operating-temperature MWIR detector diodes. *J. Electron. Mater.*, 37(9):1401–1405, September 2008.

[63] T.J. De Lyon, J.E. Jensen, I. Kasai, G.M. Venzor, K. Kosai, J.B. De Bruin, and W.L. Ahlgren. Molecular-beam epitaxial growth and high-temperature performance of HgCdTe midwave infrared detectors. *J. Electron. Mater.*, 31(3):220–226, March 2002.

[64] G.M. Williams and R.E. De Wames. Numerical simulation of HgCdTe detector characteristics. *J. Electron. Mater.*, 24(9):1239–1248, September 1995.

[65] A.I. D'Souza, J. Bajaj, R.E. De Wames, D.D. Edwall, P.S. Wijewarnasuriya, and N. Nayar. MWIR DLPH HgCdTe photodiode performance dependence on substrate material. *J. Electron. Mater.*, 27(6):727–732, June 1998.

[66] P.Y. Emelie, J.D. Phillips, S. Velicu, and P.S. Wijewarnasuriya. Parameter extraction of HgCdTe infrared photodiodes exhibiting Auger suppression. *J. Phys. D Appl. Phys.*, 42(234003):1–8, December 2009.

[67] W.E. Tennant, D. Lee, M. Zandian, E. Piquette, , and M. Carmody. MBE HgCdTe technology: A very general solution to IR detection, described by "Rule 07", a very convenient heuristic. *J. Electron. Mater.*, 37(9):1406–1410, September 2008.

[68] P.Y. Emelie, J.D. Phillips, S. Velicu, and C.H. Grein. Modeling and design consideration of HgCdTe infrared photodiodes under nonequilibrium operation. *J. Electron. Mater.*, 36(8):846–851, August 2007.

[69] J. Piotrowski, A. Jozwikowska, K. Jozwikowski, , and R. Ciupa. Numerical analysis of longwavelength extracted photodiodes. *Infrared Physics*, 34(6):565–572, December 1993.

[70] George M. Williams. HgCdTe detector modeling program.

[71] A.B. Chen, Y.-M. Lai-Hsu, S. Krishnamurthy, M.A. Berding, and A. Sher. Band structures of HgCdTe and HgZnTe alloys and superlattices. *Semicond. Sci. Tech.*, 5(3S):S100–S102, March 1990.

[72] M.A. Berding, A. Sher, M. van Schilfgaarde, A.C. Chen, and J. Arias. Modeling of arsenic activation in HgCdTe. *J. Electron. Mater.*, 27(6):605–609, 1998.

[73] D. Ambrose and C.H.S. Sprake. The vapour pressure of mercury. *J. Chem. Thermodynamics*, 4(4):603–620, July 1972.

[74] G.R. Nash, J.F.W. Schiz, C.D. Marsh, P. Ashburn, and G.R. Booker. Activation energy for fluorine transport in amorphous silicon. *Appl. Phys. Lett.*, 75(32):3671, 1999.

[75] D. Shaw. The diffusion of arsenic in $Hg_{0.8}Cd_{0.2}Te$. *Semicond. Sci. Tech.*, 9:1729–1732, 1994.

[76] L.O. Bubulac, D.D. Edwall, S.J.C. Irvine, E.R. Gertner, and S.H. Shin. P-type doping of double layer mercury cadmium telluride for junction formation. *J. Electron. Mater.*, 24(5):617–624, 1995.

[77] L.O. Bubulac, S.J.C. Irvine, E.R. Gertner, J. Bajaj, W.P. Lin, and R. Zucca. As diffusion in $Hg_{1-x}cd_xte$ for junction formation. *Semicond. Sci. Technol.*, 8:S270–S275, 1993.

[78] S.H. Shin, J.M. Arias, M. Zandian, J.G. Pasko, L.O. Bubulac, and R.E. De Wames. Enhanced arsenic diffusion and activation in HgCdTe. *J. Electron. Mater.*, 24(5):609–615, 1995.

[79] D. Chandra, M.W. Goodwin, M.C. Chen, and L.K. Magel. Variation of arsenic diffusion coefficients in HgCdTe alloys with temperature and Hg pressure: Tuning of p on n double layer heterojunction diode properties. *J. Electron. Mater.*, 24(5):599–608, 1995.

[80] D. Shaw. Diffusion in mercury cadmium telluride-an update. *J. Electron. Mater.*, 24(5):587–598, 1995.

[81] J.M. Arias, J.G. Pasko, M. Zandian, S.H. Shin, G.M. Williams, L.O. Bubulac, R.E. De Wames, and W.E. Tennant. MBE HgCdTe heterostructure p-on-n planar infrared photodiodes. *J. Electron. Mater.*, 22(8):1049, 1993.

[82] D. Chandra, D.F. Weirauch, H.F. Schaake, M.A. Kinch, F. Aqariden, C.F. Wan, and H.D. Shih. Growth of very low arsenic-doped HgCdTe. *J. Electron. Mater.*, 34(6):963–967, 2005.

[83] S. Holander-Gleixner, H.G. Robinson, and C.R. Helms. Simulation of HgTe/CdTe interdiffusion using fundamental point defect mechanisms. *J. Electron. Mater.*, 27(6):672, 1998.

[84] G. Bishop, E. Plis, J.B. Rodriguez, Y.D. Sharma, H.S. Kim, L.R. Dawson, and S. Krishna. nBn detectors based on InAs/GaSb type-II strain layer superlattice. *J. Vac. Sci. Technol. B*, 26(3):1145–1148, May/June 2008.

[85] J.B. Rodriguez, E. Plis, G. Bishop, Y.D. Sharma, H. Kim, L.R. Dawson, and S. Krishna. nBn structure based on InAs/GaSb type-II strained layer superlattices. *Appl. Phys. lett*, 91(043514):1–2, July 2007.

[86] H.S. Kim, E. Plis, J.B. Rodriguez, G.D. Bishop, Y.D. Sharma, L.R. Dawson, s. Krishna, J. Bundas, R. Cook, D. Burrows, R. Dennis, K. Patnaude, A. Reisinger, and M. Sundaram. Mid-IR focal plane array based on type-II InAs/GaSb strain layer superlattice detector with nBn design. *Appl. Phys. Lett.*, 92(18):183502, 2008.

[87] E. Plis, S. Myers, A. Khoshakhlagh, H. S. Kim, Y. Sharma, N. Gautam, R.. Dawson, and S. Krishna. InAs/GaSb strained layer superlattice detectors with nBn design. *Infrared Phys. Technol.*, 52(6):335–339, 2009.

[88] E. Plis, S. Myers, M.N. Kutty, J. Mailfert, and E.P. Smith. Lateral diffusion of minority carriers in InAsSb-based nBn detectors. *Appl. Phys. Lett.*, 97(123503):1–3, 2010.

[89] Y. Sharabani, Y. Paltiel, A. Sher, A. Raizman, and A. Zussman. InAsSb/GaSb heterostructure based mid-wavelength-infrared detector for high temperature operation. *Appl. Phys. Lett.*, 90:232106, 2007.

[90] P. Klipstein. "XBn" barrier photodetectors for high sensitivity and high operating temperature infrared sensors. *Proc. SPIE*, 6940:69402U, 2008.

[91] A.M. White. Infra red detectors, 1987.

[92] A.M. Itsuno, J.D. Phillips, and S. Velicu. Predicted performance improvement of Auger suppressed HgCdTe photodiodes and p-n heterojunction detectors. *IEEE Trans. Electron Devices*, 58(2):501–507, December 2011.

[93] S. Velicu, C.H. Grein, and S. Sivananthan. Nonequilibrium photodetectors with single carrier species barriers, 2008.

[94] A.M. Itsuno, J.D. Phillips, and S. Velicu. Design and modeling of HgCdTe nBn detectors. *J. Electron. Mater.*, 40(8):1624–1629, 2011.

[95] V. Gopal. A general relation between zero-bias resistance-area product and perimeter-to-area ratio of the diodes in variable-area diode test structures. *Semicond. Sci. Technol.*, 11:1070–1076, 1996.

[96] M.H. Weiler and G.J. Tarnowski. Characterization of HgCdTe P-on-n heterojunction photodiodes and their defects using variable area structures. *J. Electron. Mater.*, 26:635–642, 1997.

[97] J. Antoszewski, C.A. Musca, J.M. Dell, and L. Faraone. Small two-dimensional arrays of mid-wavelength infrared HgCdTe diodes fabricated by reactive ion etching -induced p-to-n -type conversion. *J. Electron. Mater.*, 32:627–632, 2003.

[98] M. Henini and M. Razeghi, editors. *Handbook of infrared detection technologies.* Elsevier Advanced Technology: UK, 2002.

[99] R. Singh, A.K. Gupta, and K.C. Chabra. Surface passivation of mercury-cadmium-telluride infrared detectors. *Defence Sci. J.*, 41(3):205–239, 1991.

[100] Y.-H. Kim, S.-H. Bae, H.C. Lee, and C.K. Kim. Surface leakage current analysis of ion implanted ZnS-passivated n-on-p HgCdTe diodes in weak inversion. *J. Electron. Mater.*, 29(6):832–836, 2000.

[101] Y.-C. Jung, S.-J. Yoon, S.-H. Suh, and J.-S. Kim. The effect of ammonium sulfide treatment on interfacial properties in ZnS/HgCdTe heterostructure. *J. Electroceram.*, 17(2):1041–1045, 2006.